UNIVERSITY OF CALIFORNIA
RIVERSIDE

MoS_2 Heterostructures Based Biosensors

A Dissertation submitted in partial satisfaction
of the requirements for the degree of

Doctor of Philosophy

in

Chemical and Environmental Engineering

by

Ying Chen

March 2024

Dissertation Committee:
Dr. Ashok Mulchandani, Chairperson
Dr. Ruoxue Yan
Dr. Jianlin Liu

The Dissertation of Ying Chen is approved:

_____

_____

_____

Committee Chairperson

University of California, Riverside

ACKNOWLEDGEMENTS

I would like to express my profound gratitude to my advisor, Prof. Ashok Mulchandani, for his guidance and support throughout this whole PhD journey. I'm very proud of being a member of Prof. Mulchandani's group. His exceptional scientific fervor and knowledge positioned him as an exemplary research advisor, and his compassionate and supportive mentorship is held in high regard. He has been instrumental in helping me navigate challenging periods, offering unwavering understanding and support to both me and my family. Graduate studies come with their own set of trials, yet under his mentorship, I have felt more empowered and encouraged.

I am sincerely thankful for the guidance and support from my defense committee members, Prof. Ruoxue Yan and Prof. Jianlin Liu; and in the Preliminary Exam, Prof. Younjin Min and Prof. Yun Shen. I would like also to thank my former and current lab mates: Yu Shen, Mohammed Sedki Abuelhassan, Guo Zhao, Xingyu Chen, Touhid Bin Anwar, Gaurav Ahuja, and Samriddha Dutta. My appreciation also goes to my mentored intern student, Nataly Vicente, who excelled during her time working with me. Special thanks to my former colleague, Tung Pham, for his contributions that have significantly aided me in reaching my goals. I am lucky to have you as my senior. My close friends, Xinyao Zheng and Yue Xing, deserve a special

mention for the joy and camaraderie during our workout sessions and learning together. Finally, a thank you to all my classmates, friends, teachers, and relatives who have cared for, supported, and assisted me.

Lastly, but certainly not least, I must thank my husband, who has been by my side through thick and thin, providing constant encouragement and support. To my parents, whose love, endless support, and reliance have been my bedrock. To my son, whose companionship has brought immense joy and enriched my life experiences.

ABSTRACT OF THE DISSERTATION

MoS_2 Heterostructures Based Biosensors

by

Ying Chen

Doctor of Philosophy, Graduate Program in Chemical and Environmental Engineering
University of California, Riverside, March 2024
Professor Ashok Mulchandani, Chairperson

Two-dimensional (2D) nanomaterials have significantly advanced biosensor technology. Their unique properties enable highly sensitive and specific biomolecule detection, streamlining diagnostics and environmental monitoring with their rapid and efficient capabilities. In this research, we conducted a comprehensive investigation into the development and optimization of flexible optoelectronic biosensors using 2D molybdenum disulfide (MoS_2) for the rapid selective detection of biomolecules. Through a series of experimental studies, we explored innovative strategies that leverage the unique photoresponse characteristics of MoS_2 and the electrical conductivity of graphene to enhance biosensor performance. In the first part of our

study, we introduced a MoS_2-based optoelectronic biosensor that demonstrates significantly improved sensitivity and selectivity under photonic excitation. Following this, we extend this approach by integrating MoS_2 with graphene electrodes to address conductivity limitations, resulting in a hybrid optoelectronic biosensor with superior sensitivity. Our research further advanced by examining vertical heterostructures of MoS_2 and graphene, presenting two configurations that optimize biomolecule sensing capabilities. Our findings reveal that biofunctionalized MoS_2 platforms and MoS_2 and graphene heterostructures Field-Effect Transistors (FETs) achieve high sensitivity and specificity, significantly advancing biosensor technology. These innovations offer fresh perspectives and methods to boost biosensor performance, paving the way for health and environmental breakthroughs.

CONTENTS

LIST OF FIGURES

Chapter 1

Introduction: MoS_2 - A Valuable Component for Constructing Biosensors

1.1 Introduction

Two-dimensional (2D) layered van der Waals (VDW) nanomaterials, such as graphene and transition metal dichalcogenides (TMDs), are at the forefront of advancements in chemical and biological sensing, attributed to their exceptional optical, electronic, and catalytic characteristics. Among these, MoS_2-based nanomaterials have emerged as particularly compelling due to their distinctive electronic, optical properties, and vast surface modification potential, making them ideal for nanoelectronics and optoelectronics applications. Their remarkable electrochemical and optical attributes have positioned MoS_2 nanomaterials as innovative platforms for biosensing, capable of detecting a wide array of analytes.

MoS_2 stands out within the TMD family for its unique properties, especially its direct bandgap in monolayer formations, offering promising avenues for semiconductors, photodetectors, and biosensors. Its ability to exhibit a direct bandgap in monolayer form makes it a promising candidate for various applications, including semiconductors, photodetectors, and biosensors. MoS_2's mechanical flexibility and high surface area also offer advantages in flexible electronics and optoelectronics devices and show great potential in the field of biosensing.

1.2 MoS_2 optical and electric properties

MoS_2, as one of the most popular members of the TMDCs family, features a graphite-like hexagonal structure with S-Mo-S layers bound by VDW forces. Its semiconducting behavior transitions from a 1.8 eV direct bandgap in monolayers to a 1.2 eV indirect bandgap in bulk, highlighting its adaptability in electronic and optoelectronic fields. Monolayer and few-layer MoS_2 stand out for their exceptional mobility and high I_{on}/I_{off} ratio, with negligible standby power loss, positioning it as a prime candidate for future electronics, optoelectronics, and energy storage innovations.

The electrical properties of MoS_2, particularly in atomically thin layers, have been a focal point for research in applications like field-effect transistors (FETs) and light-harvesting devices due to their outstanding electronic properties. Both bulk, few-layer, and monolayer MoS_2 FETs, have been explored, revealing significant insights into charge transport characteristics. Charge carrier transport in 2D MoS_2 is notably influenced by carrier density or Fermi energy, impacting the material's resistivity and transition between insulating and conducting states. It is easily exfoliated by ion diffusion or external mechanical forces to get a single layer or few layers. Also, chemical vapor deposition methods have been utilized for the synthesis of high-quality 2D MoS_2 nanosheets. These preparation methods significantly influence the physical properties and application potential of MoS_2. Figure 1.1 shows the reported mobility values for

MoS_2 devices across various studies, categorizing the data based on factors like synthesis method, thickness, measurement temperature, and other testing parameters. The carrier mobility values for monolayer MoS_2, as depicted in Figure 1.1a, span a broad range, covering three orders of magnitude from 1 to 1000 cm^2/Vs. Additionally, the electron mobility in monolayer MoS_2 varies widely, with temperature and layer number significantly affecting it, indicating the material's potential for diverse electronic applications. Figure 1.1b illustrates a trend where the room temperature mobility of the material is enhanced with an increase in the number of layers. This variation points to the delicate dependence of MoS_2 device performance on material quality, fabrication techniques, and device design.

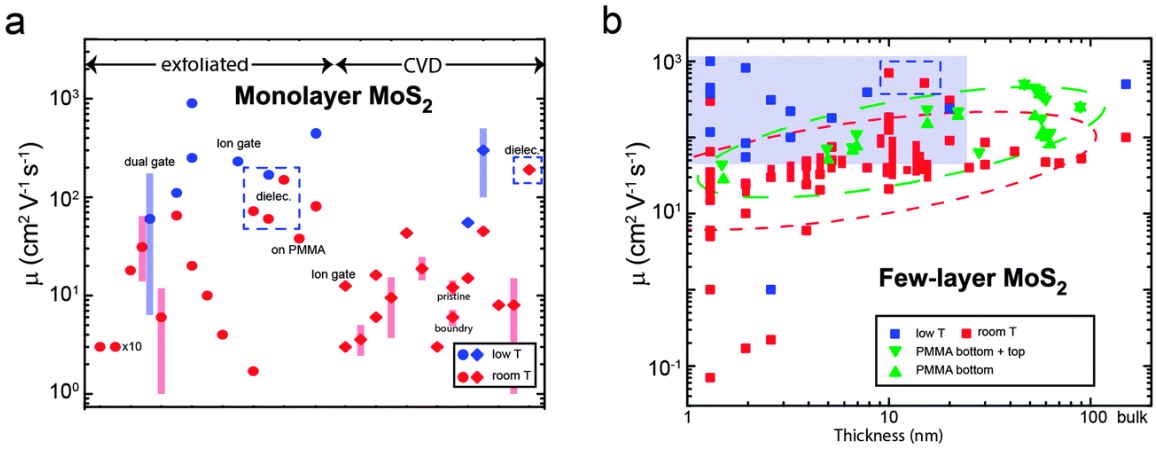

Figure 1.1. Carrier mobilities reported for (a) monolayer and (b) few-layer MoS_2. The values are obtained from the review by Schmidt et al.1 Reproduced with permission from ref. 1, Copyright 2015, The Royal Society of Chemistry.

The optical properties of MoS_2, ranging from ultraviolet-visible spectroscopy (UV-vis) and photoluminescence (PL) to Raman spectroscopy, have been thoroughly studied to comprehend its electronic structure and interaction mechanisms.[2,3] These techniques provide comprehensive insights into MoS_2's electronic structure, bandgap, and vibrational modes, making them essential for understanding its optical behavior and suitability for various applications in electronics and photonics. Raman spectroscopy plays a pivotal role in characterizing the optical properties of MoS_2 by enabling the precise identification of its vibrational modes. This technique is crucial for distinguishing between single, few-layer, and bulk MoS_2 structures, providing insights into their electronic and structural dynamics. Through Raman analysis, researchers can observe shifts in vibrational frequencies that correlate with changes in material thickness, revealing significant information about the material's lattice structure and electron-phonon interactions (Figure 1.2a and 1.2b). Meanwhile, AFM offers precise thickness measurements of MoS_2 layers (Figure 1.2c), crucial for correlating physical dimensions with optical and electronic properties. Studies have shown that MoS_2's optical behavior, including excitonic transitions and layer-dependent photoluminescence, offers insights into its potential for applications in electronics, photonics, and biosensing. Figure 1.2d displays the PL spectra for single-layered (1L), double-layered (2L), and triple-layered (3L) MoS_2, revealing two prominent peaks Peak

A (1.85 eV) and Peak B (2.05 eV). These peaks correspond to direct bandgap transitions, with the energy difference between two peaks reflecting the valence band splitting caused by strong spin-orbit interactions. The observation of weaker Peak I, which signify indirect bandgap transitions in the PL spectra of 2L and 3L MoS_2, contrasts with their absence in 1L MoS_2. This distinction highlights an indirect bandgap is transited to a direct bandgap energy structure when a thickness of 2L reduced to 1L. This characteristic change underscores the utility of PL spectroscopy in elucidating the electronic structure of MoS_2, demonstrating how PL can be a powerful tool for distinguishing between direct and indirect bandgap transitions, bandgap energy, and the layer thickness on MoS_2 properties. Together, these techniques offer a comprehensive toolset for exploring the nuanced interactions within MoS_2 structures, significantly advancing our understanding of the versatile material in nanotechnology and optoelectronics applications.

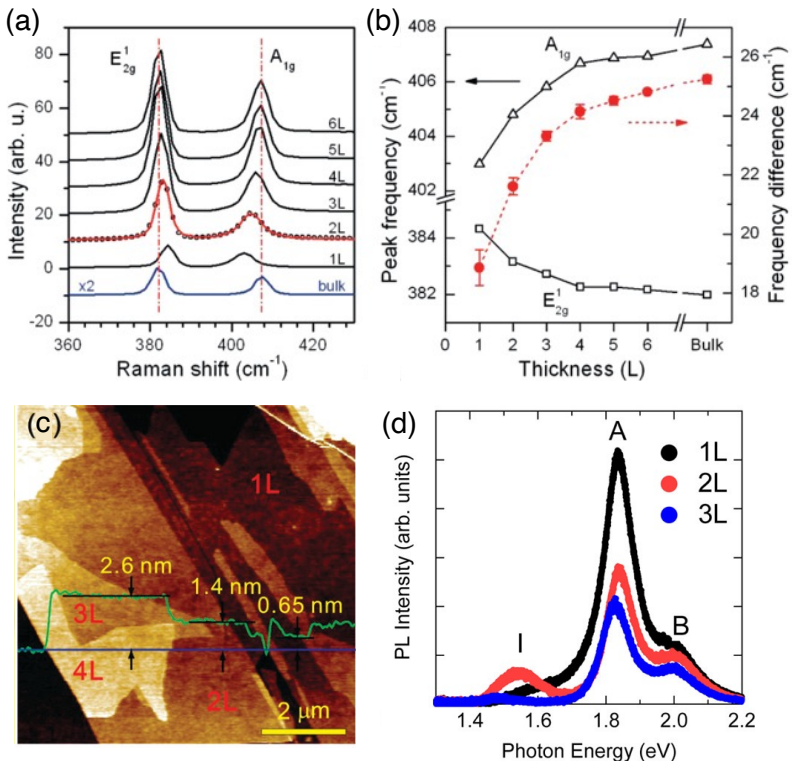

Figure 1.2. (a) Raman spectra of thin (nL) and bulk MoS_2 films. (b) Frequencies of MoS_2 Raman modes (left vertical axis) and their difference (right vertical axis) as a function of layer thickness. (c) AFM height image with thickness measurements. (a)-(c) Reproduced with permission from ref. 2, Copyright 2010, American Chemical Society. (d) PL spectra of MoS_2 films. (d) Reproduced with permission from ref. 4, Copyright 2013, American Chemical Society.

1.3 MoS_2 FET biosensing application

2D MoS_2 has captured significant interest for its potential to transform biosensing technologies, thanks to its superior electrical and optical attributes. MoS_2's incorporation into FET biosensors marks a crucial breakthrough, enhancing the sensitivity and specificity for biomolecule detection. Biosensor devices designed for real-time and onsite detection have become a focal point of research. The rapid

advancement in biosensing technologies has catalyzed a transformative shift towards early disease diagnostics and environmental monitoring, accommodating a wide array of biofunctionalization strategies. MoS_2 FET-based biosensor strategies target molecules ranging from disease-related proteins and DNA to environmental contaminants like Bisphenol A, ensuring versatility and broad applicability in detection capabilities. Herein, we summarize recent progress in MoS_2 FET biosensors, focusing on their biofunctionalization methods, application across diverse detection targets, and real-sample testing platforms.

To precisely detect specific biomolecules using 2D-FET platforms, it is necessary to modify the semiconductor channel with molecules that can recognize the target biomolecules.[5,6] This process involves using physical and chemical methods that are compatible with the device's architecture to attach recognition molecules (such as antibodies, enzymes, or nucleic acids) that have a specific affinity for the biomolecule of interest.[7] These biorecognition elements exploit the specificity of biological interactions, including enzyme-substrate reactions and nucleic acid hybridization, to achieve targeted and highly specific biomolecule detection on the FET biosensor platform. In 2D MoS_2-based FET biosensors, surface charge or mass modifications directly impact the electric field or surface potential, hence, the resistive channel area and transconductance vary.[8,9] The biofunctionalization of MoS_2 surfaces is pivotal for

enhancing a biosensor's sensitivity and selectivity. Non-chemical adsorption for receptor binding stands out as the simplest yet effective method. Lee et al. showcased this through MoS_2 FET biosensors detecting prostate-specific antigen (PSA) in a label-free platform without requiring chemically treated gate dielectrics.[10] They utilized the MoS_2 surface's hydrophobicity to facilitate strong protein-surface adsorption. Anti-PSA antibodies were physisorbed non-specifically on the sensing area, followed by the selective binding of PSA antigens. The research by another group led by Lee et al. underscored a direct and effective biosensing strategy via the interaction between the MoS_2 channel and the analyte.[11] Their study on biofunctionalization showed that the nucleobases of probe DNA molecules could bind with MoS_2's surface via van der Waals forces. Notably, the study achieved a limit of detection (LOD) for 10 fM and with a detection range of 10^{-14} M to 10^{-8} M, demonstrating the method's high sensitivity and broad applicability in biosensing.

Techniques like APTES-glutaraldehyde coupling for biomolecule attachment have been crucial. Combining high-k metal oxide dielectric gate insulators with MoS_2 FET biosensors has shown remarkable effectiveness for enhancing device stability and sensitivity. This setup benefited from the properties of these materials, as Park et al. had shown with a MoS_2 FET biosensor that enables reliable and quantitative detection of biomarkers in nonaqueous environments.[12] This was achieved by preventing

nonspecific binding, ensuring uniform chemisorption of biomolecules on the MoS_2 surface. Wang et al. coated their device with a 7–8 nm layer of hafnium oxide (HfO_2), and subsequently treated it with APTES and glutaraldehyde for biofunctionalization.[13] This method facilitated the label-free platform for real-time PSA detection.

The detection of specific proteins such as PSA, human immunoglobulin G (IgG), and severe acute respiratory syndrome coronavirus 2 (SARS-CoV-2) antibody using MoS_2 FET biosensors signifies a leap towards pinpointing disease markers with unprecedented precision. Research has showed the capability of MoS_2 FETs to identify these proteins sensitively and selectively, underscoring their potential in cancer diagnostics and viral infection assessments at an early stage. Song et al. reported an ultrasensitive FET biosensor utilizing vertically aligned MoS_2 nanolayers (VAMNs) grown via chemical vapor deposition.[14] these VAMNs provided abundant, dense surface-active sites for molecule biofunctionalization, which was supported by detailed XPS evidence. The design integrated thiol-based linkers for biofunctionalization, enabling PSA detection within a 10-10^7 fg/mL range and attaining a low LOD of 800 fg/mL, significantly outperforming traditional methods and commercial ELISA kits. This structure facilitated rapid, sensitive PSA detection in human serum, showing promise for early-stage prostate tumors disease diagnosis. Moreover, the rapid sulfurization process used for VAMNs growth facilitated simple patterning of FET

channels, making it compatible with microfabrication processes and enabling wafer-scale fabrication. The study by Ji et al. investigated multi-layer MoS_2-FET biosensors for detecting various proteins, including IgG, β-actin, and PSA, focusing on the sensing mechanism and the key factors influencing responses.[15] The researchers modeled the MoS_2-FET response to IgG, showing consistency with experimental data. They explored how channel dimensions and dielectric materials, especially those with lower dielectric constants, affected biosensing performance due to their impact on gate capacitance. The study also investigated how the acidity and alkalinity of proteins affect sensor performance, where β-actin and PSA exhibited opposite acidity compared to IgG as representative examples, revealing that induced doping and gating effects played significant roles. This comprehensive analysis provided valuable insights for designing MoS_2-FET biosensors, demonstrating the importance of device dimensions, dielectric properties, and the acid-base properties of proteins.

The specificity of DNA detection holds profound implications for genetic diagnostics and personalized medicine. MoS_2 FET biosensors, through the strategic functionalization with probe DNAs, have been shown to specifically capture target DNA sequences, offering a pathway to rapid and precise genetic analysis. Liu et al. utilized CVD-grown monolayer MoS_2 films to craft an ultrasensitive FET biosensor aimed at noninvasive prenatal testing for detecting trisomy 21 (Down Syndrome)

through DNA screening. The biosensor, enhanced with gold nanoparticles and tailored probe DNAs, achieved a detection range from 100 aM to 1 fM, with a LOD under 100 aM and high specificity, meeting the criteria for screening Down Syndrome-related DNA fragments (chromosome 21 or 13). Their research underscored MoS_2-FET biosensors' capability in identifying chromosomal abnormalities from pregnant women's peripheral blood, highlighting a promising route for early disease diagnosis characterized by high sensitivity and affordability.

The application of MoS_2 FET biosensors has extended to detect small molecules, demonstrating the versatility and sensitivity of these devices in environmental monitoring contexts. Hossain et al. developed a microfluidic MoS_2 FET biosensor to detect Bisphenol A (BPA), a small molecule harmful to health and the environment.[16] By utilizing gold nanoparticles functionalized with DNA aptamers, the research unveiled a novel sensing mechanism where BPA's electro-oxidation generates phenoxy radicals, reacting with nucleophiles, and leading to the detachment of DNA from the MoS_2 surface, causing a detectable current change. By achieving a detection range from 1 pg/mL to 100 ng/mL and a LOD as 1 pg/mL, the device demonstrated rapid response and high specificity, marking a significant advancement in MoS_2-based biosensors for detecting low-concentration harmful substances in environmental and healthcare settings.

The ultimate test of a biosensor's efficacy lies in its performance with real samples. MoS_2 FET biosensors have successfully detected disease markers in diluted serum samples and environmental contaminants in water samples, highlighting their practical applicability and robustness. Chen et al. introduced a MoS_2 FET biosensor designed for utraselective antibiotic sensing, targeting kanamycin (KAN) via a complementary strand DNA-assisted aptamer.[17] The study concluded that the sensing mechanism involves the release of charge from the probe, effectively overcoming the Debye screening limitation and enhancing selectivity. Furthermore, it discussed interaction kinetics to elucidate the sensing principle. Demonstrating a low detection limit (0.66 nM to 1.06 nM) and high selectivity, the sensor was applied in real-water monitoring, where various antibiotics coexist, showcasing its potential for sensing in real-time applications. This approach significantly improved selectivity and reliability, while minimizing variations between devices. The sensor's application extended to detecting water samples from tap and lake water, achieving high recoveries in recovery tests. Wei et al. showcased the sensitive and quantitative detection of SARS-CoV-2 antibodies using a MoS_2-FET biosensor functionalized with the spike protein receptor binding domain.[18] Employing an on-chip calibration method, this approach enabled reliable quantification of antibody levels in vaccinated serum samples and significantly contributed to clinical diagnostics for COVID-19.

Exploiting the dual electrical and optical features of 2D MoS_2 FETs for biosensing significantly improves detection accuracy and versatility. This approach, as illustrated by De-Eknamkul et al., involves the creation of a dual-mode optoelectronic MoS_2 biosensor.[19] They developed a dual-mode optoelectronic MoS_2 biosensor capable of generating concurrent electrical and optical signals from biomolecular interactions. The study outlined the innovative design of a biosensor that effectively combined a MoS_2-based FET with a photonic crystal slab to enable dual functionality as both a FET and an optical modulator. The assembly incorporated a CVD MoS_2-based FET suspended over a silicon nitride (SiN) membrane, complemented by alumina (Al_2O_3) and indium tin oxide layers (ITO) as the optically transparent dielectric and back gate electrode for enhanced optical and electronic properties, as shown in Figure 1.3a and 1.3b. Integrating a meticulously patterned photonic crystal supports nanophotonic operation, allowing light transmission. By leveraging MoS_2's interaction with photonic nanostructures, this setup facilitates a multimodal sensor capable of detailed biomolecular analysis through electrical and optical signals. Directly immobilizing μ-opioid receptor illustrates the sensor's efficiency in detecting synthetic opioid peptides. Both the electronic and optical sensing modes showed consistent trends (Figure1.3c to 1.3f), with detection limits falling below 1 nM. These results indicate a high level of

sensitivity and a broad operational scope for the biosensor, showcasing its capability to detect minute concentrations of biomolecules effectively.

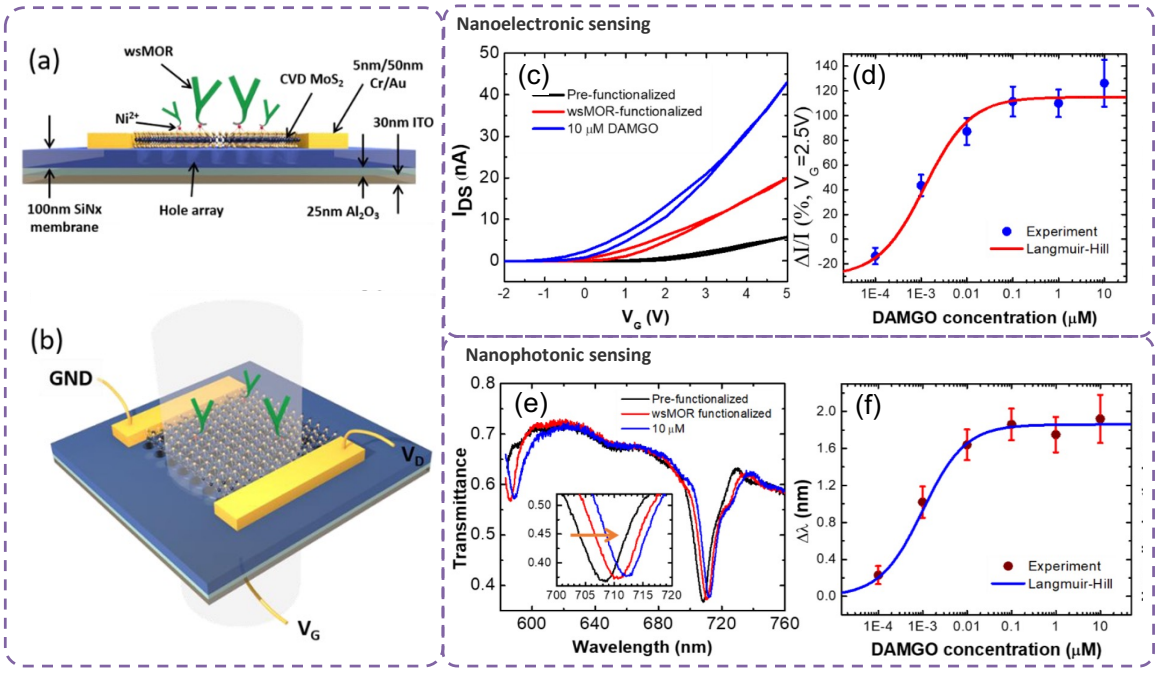

Figure 1.3. (a) Device structure and (b) Sensing scheme of the dual-mode sensor. Nanoelectronic sensing. (c) I_{DS}–V_G characteristics of the biosensor during biofunctionalization process. (d) Electronic response reported as percentage change in I_{DS} with respect to the I_{DS} of biofunctionalized device. Nanophotonic sensing. (e) Transmission spectra of the biosensor during biofunctionalization process. (f) Optical response reported as resonance wavelength shift with respect to the resonance peak position of biofunctionalized device. Reproduced with permission from ref. 19, Copyright © IOP Publishing Ltd.

1.4 MoS_2-Based 2D Heterostructures

2D materials and their heterostructures are gaining attention as promising alternatives due to their diverse bandgaps, absence of dangling bonds, exceptional mobility at atomic layer thicknesses, high optical absorption coupled with transparency, and suitability for flexible and stretchable electronics and

optoelectronics.[20] This system enables the integration of different materials with varied electronic, optical, and mechanical properties, creating engineered materials with customized properties for advanced electronics, optoelectronics, and biosensing applications.[21–23] Within the nanotechnology and materials science fields, MoS_2 is a critical element for boosting heterostructure performance and functionality. Characterized by its atomic-layer thickness, MoS_2 offers unique electrical, optical, and mechanical advantages when integrated into heterostructures with other 2D materials. This integration creates a sensitive platform for improved sensing performance and enhances the overall functionality of the heterostructures.

Xu et al. demonstrated an enhancement in photocurrent and introduced gate-tunable heterostructures for phototransistors.[24] They constructed a 2D atomic thin phototransistor based on a MoS_2 and graphene hybrid device. The device demonstrated a notably higher photoresponse compared to phototransistors based solely on graphene or MoS_2. The robust and specific light absorption within the MoS_2 layer led to the generation of electric charges, which were then transferred to the graphene layers through an inherent electric field. Within the graphene layers, these charges circulated multiple times, facilitated by the high carrier mobility characteristic of graphene. The integration of MoS_2 films with graphene in heterostructures significantly enhanced photocurrent generation, underscoring the crucial role of MoS_2. By adjusting the

thickness of MoS_2, precise spectral sensitivity tuning was achieved, leading to a substantial increase in device responsivity (up to ~10,000 mA/W under specific conditions). The sensitivity tuning marked a considerable advancement over traditional MoS_2 or graphene phototransistors. Moreover, the MoS_2-graphene combination facilitated rapid photo-switching, with swift photocurrent saturation and reduction times, emphasizing the structure's efficiency and potential to significantly improve the performance of phototransistor devices. Vera-Hidalgo and colleagues developed a technique for covalently grafting MoS_2 flakes onto graphene monolayers in FETs.[25] This innovative approach provided an alternative to traditional van der Waals force-based assembly, enabling precise control over the interface's interlayer spacing and chemical characteristics. By functionalizing MoS_2 with maleimide moieties and anchoring them onto graphene through diazonium groups, they introduced a molecular interface that enhanced device performance beyond the inherent attributes of the constituent materials. This example underscores the capability of MoS_2 to facilitate improved interactions between 2D materials, offering a sophisticated method for enhancing device functionality through chemical customization.

Utilizing the heterostructure can also enhance the carrier mobility of MoS_2 to achieve high performance. Kim et al. proposed a junction FET architecture with MoS_2 as channel and graphene-MoS_2 heterointerface for optimal contact material.[26] The

heterointerface's performance, characterized by its high carrier mobility (up to 100 cm^2/Vs) and on/off current ratio (up to 10^8 at room temperature), contrasted with the standard mobility (~10 cm^2/Vs) observed in pure MoS_2 devices. This performance was supported by graphene's additional conduction pathway and ability to adjust the Fermi level, offering precise control over the device's conduction properties. This dual conduction mechanism underscores the graphene-MoS_2 heterojunction's potential as a high-performance electronic device platform. The FETs fabricated by Han et al. using MoS_2/graphene heterostructures have shown a significant improvement in electron transmission performance compared to devices made solely from MoS_2.[27] The MoS_2/graphene FETs demonstrate marked improvements: on-state current boosts from 3.7×10^{-8} A to 6.2×10^{-7} A, switching ratios increase from 10^4 to 10^5, and maximum drain currents jump from 2.4×10^{-7} A to 4.3×10^{-6} A, showcasing an order of magnitude enhancement over MoS_2-only FETs. These heterostructure FETs exhibit improved mobility and more effective control over the gate electric field. Another notable advancement is the ability to better regulate the interlayer impedance in MoS_2/graphene FETs by manipulating gate and drain voltages. Those studies underscore the potential of 2D heterostructures and novel device architectures in advancing electron transmission capabilities, thereby broadening the horizons for research into electric and optoelectronic devices leveraging van der Waals forces.

Pham et al.'s research illustrated the n-doping effect of MoS_2 in MoS_2/graphene heterostructures and the significant potential for enhancing electronic devices sensing performance.[28] The paper elucidated the advantageous n-doping effect of integrating MoS_2 with graphene, illustrated through a band-alignment diagram. Here, inherently n-type CVD-processed MoS_2 was stacked with strongly p-doped CVD-graphene to create a heterojunction. This combination, driven by the variance in work functions, prompted electron migration from MoS_2 to graphene, neutralizing the excess of holes in graphene and causing an upward shift in its Fermi level. Such a shift, indicative of reduced p-doping, led to a decreased work function in the graphene component of the heterostructure compared to its single-layer counterpart. This mechanism likely contributed to the diminished PL intensity observed in the MoS_2/graphene heterostructure by reducing electron-hole recombination during PL excitation. Expanding on this foundation, the team evaluated the sensing capabilities of the devices by subjecting them to various gaseous analytes. Devices based on graphene alone exhibited minimal response to toluene. In contrast, although MoS_2-based devices demonstrated a higher affinity for toluene, their performance was limited by high contact resistance and reduced electrical mobility. Remarkably, the devices incorporating the MoS_2/graphene heterostructure as the sensing channel showed a significant response, registering a 12.5% change in current in the presence of toluene

concentrations at 10% saturation. This finding emphasized the MoS_2/graphene heterostructure's superior performance over that of the individual components, achieving enhanced stability, sensitivity, and signal-to-noise ratio in sensing applications. Cho et al. reported on flexible chemoresistive gas sensing devices based on MoS_2/graphene heterostructures designed for detecting NO_2 and NH_3.[29] They observed that the junction between graphene and MoS_2 film typically results in a lower barrier height, leading to less modulation upon gas adsorption compared to a metal-MoS_2 junction. This characteristic is advantageous for gas sensing performance, as it enhances the device's sensitivity to NO_2 and NH_3 by leveraging the unique properties of the MoS_2/graphene interface. Ignatova et al. explored the potential of MoS_2-graphene heterostructures for label-free biosensing, targeting a widely used cancer medication.[30] Their comprehensive study revealed that lattice mismatches and variations in work function at the nanoscale significantly boost biosensor efficiency through three distinct optical detection methods. The research highlighted the pivotal role of these heterostructures in enhancing sensitivity and specificity for biomolecule detection, signifying a major leap in biosensing technology.

Moudgil et al. developed an n-type MoS_2/TiO_2 hybrid nanostructure-based FET platform, functionalized with vancomycin, to capture and selectively detect Gram-positive bacteria.[31] The device demonstrated the capability for real-time monitoring,

detecting target concentrations as low as 50 cfu/mL with notable sensor stability. The biosensor accurately identified *S. aureus* when tested under physiological conditions, in complex matrices akin to human serum. In a comparative analysis of the sensitivity of MoS_2/TiO_2, MoS_2, and TiO_2 FET biosensors towards Gram-positive and Gram-negative bacteria, the MoS_2/TiO_2 FET exhibited the highest sensitivity for *S. aureus* detection. The performance of the biosensor was distinguished by its high sensitivity (49.47 ± 1.7%) towards *S. aureus*, demonstrating a low detection limit of 50 cfu/mL and a swift response time of 22.19 seconds. These features underscore its promising utility in clinical settings.

The benefits of MoS_2 in heterostructures extend to improved photoresponse, enhanced sensitivity in sensors, and the development of next-generation electronics with lower power consumption and higher performance thresholds. Specifically, MoS_2's ability to form covalent and van der Waals bonds with other materials allows for the engineering of heterostructures with optimized charge carrier mobility, tunable band alignments, and controlled interlayer interactions. Such versatility in design and functionality underscores the significance of MoS_2 in advancing the frontier of heterostructure-based devices and beyond.

1.5 Challenges and Future Directions

MoS_2 biosensors are at the forefront of ultra-sensitive and selective detection technologies, showing immense promise for various applications from biomolecular to environmental sensing. They stand to transform diagnostic and monitoring practices, providing precise and point-of-care tools that enhance accessibility and ease of use. While the advancements in MoS_2 biosensors are promising, challenges such as reproducibility, long-term stability, and the broadening of detectable targets remain. As summarized by Samy et al., the literature reports several challenges MoS_2 materials face, particularly in structural properties, biocompatibility, and its application in electronics and optoelectronics.[32] One of the current technical challenges is the production of high-quality, homogeneous 2D MoS_2 layers.[8] The uniformity of these layers is essential for the performance of biosensors, as variability can lead to discrepancies in sensor readings. Integration of materials and advanced sensors into portable devices will require innovative approaches, such as developing new methods for transferring MoS_2 layers without inducing strain or unintentional doping, which can alter the sensor's properties.[33] *In situ* fabrication of heterostructure materials in synthetic facilities presents an alternative that may address several of these challenges.[34] By synthesizing these materials in a controlled environment, researchers can maintain the integrity of the layered structures and minimize contamination,

leading to sensors with superior performance. Reproducibility and long-term stability are also significant hurdle, which involves ensuring that these biosensors maintain their sensitivity and selectivity over time, even under varying environmental conditions. MoS_2 biosensors will be crucial tools in health and environmental applications.

1.6 Objectives and organization of this work

This research aimed to comprehensively investigate the capabilities of MoS_2 and its combinations with graphene for biosensor applications. The primary objectives of this work are to:

- Develop flexible optoelectronic biosensors based on MoS_2 for sensitive and selective biomolecule detection.
- Develop flexible optoelectronic biosensors based on 2D MoS_2 and graphene for the sensitive and selective detection of biomolecules.
- Investigate the enhancement of biosensor efficacy through the innovative integration of MoS_2 with graphene and the exploration of their unique vertical MoS_2-graphene heterostructures in biosensing, aiming to optimize sensitivity, specificity, and stability.
- Demonstrate the potential of these biosensors for practical applications, including early-stage disease diagnostics, through real-time monitoring and testing in complex matrices.

The thesis is organized into three main chapters, each focusing on a specific aspect of MoS_2-based biosensors development: Chapter 2 introduces the foundation of

utilizing MoS_2 in biosensors, showcasing the initial design, fabrication, and testing for HIgG detection. Chapter 3 expands on Chapter 2 by integrating MoS_2 with graphene to enhance biosensor performance, addressing conductivity issues, and demonstrating improved detection limits. Chapter 4 innovates with vertical heterostructures of MoS_2 and graphene, exploring different configurations and their impact on biosensing, ultimately achieving higher sensitivity and specificity.

1.7 References

(1) Schmidt, H.; Giustiniano, F.; Eda, G. Electronic Transport Properties of Transition Metal Dichalcogenide Field-Effect Devices: Surface and Interface Effects. Chem. Soc. Rev. 2015, 44 (21), 7715–7736. https://doi.org/10.1039/C5CS00275C.

(2) Lee, C.; Yan, H.; Brus, L. E.; Heinz, T. F.; Hone, J.; Ryu, S. Anomalous Lattice Vibrations of Single- and Few-Layer MoS 2. ACS Nano 2010, 4 (5), 2695–2700. https://doi.org/10.1021/nn1003937.

(3) Wang, K.; Wang, J.; Fan, J.; Lotya, M.; O'Neill, A.; Fox, D.; Feng, Y.; Zhang, X.; Jiang, B.; Zhao, Q.; Zhang, H.; Coleman, J. N.; Zhang, L.; Blau, W. J. Ultrafast Saturable Absorption of Two-Dimensional MoS 2 Nanosheets. ACS Nano 2013, 7 (10), 9260–9267. https://doi.org/10.1021/nn403886t.

(4) Mouri, S.; Miyauchi, Y.; Matsuda, K. Tunable Photoluminescence of Monolayer MoS 2 via Chemical Doping. Nano Lett. 2013, 13 (12), 5944–5948. https://doi.org/10.1021/nl403036h.

(5) Zheng, C.; Huang, L.; Zhang, H.; Sun, Z.; Zhang, Z.; Zhang, G. J. Fabrication of Ultrasensitive Field-Effect Transistor DNA Biosensors by a Directional Transfer Technique Based on CVD-Grown Graphene. ACS Applied Materials and Interfaces 2015, 7 (31), 16953–16959. https://doi.org/10.1021/acsami.5b03941.

(6) Cheng, S.; Hideshima, S.; Kuroiwa, S.; Nakanishi, T.; Osaka, T. Label-Free Detection of Tumor Markers Using Field Effect Transistor (FET)-Based Biosensors for Lung Cancer Diagnosis. Sensors and Actuators, B: Chemical 2015, 212, 329–334. https://doi.org/10.1016/j.snb.2015.02.038.

(7) Syu, Y.-C.; Hsu, W.-E.; Lin, C.-T. Review—Field-Effect Transistor Biosensing: Devices and Clinical Applications. ECS Journal of Solid State Science and Technology 2018, 7 (7), Q3196–Q3207. https://doi.org/10.1149/2.0291807jss.

(8) Kalantar-zadeh, K.; Ou, J. Z. Biosensors Based on Two-Dimensional MoS 2. ACS Sens. 2016, 1 (1), 5–16. https://doi.org/10.1021/acssensors.5b00142.

(9) Matsumoto, A.; Miyahara, Y. Current and Emerging Challenges of Field Effect Transistor Based Bio-Sensing. Nanoscale 2013, 5 (22), 10702. https://doi.org/10.1039/c3nr02703a.

(10) Lee, J.; Dak, P.; Lee, Y.; Park, H.; Choi, W.; Alam, M. A.; Kim, S. Two-Dimensional Layered MoS2 Biosensors Enable Highly Sensitive Detection of Biomolecules. Sci Rep 2014, 4 (1), 7352. https://doi.org/10.1038/srep07352.

(11) Lee, D.-W.; Lee, J.; Sohn, I. Y.; Kim, B.-Y.; Son, Y. M.; Bark, H.; Jung, J.; Choi, M.; Kim, T. H.; Lee, C.; Lee, N.-E. Field-Effect Transistor with a Chemically Synthesized MoS2 Sensing Channel for Label-Free and Highly Sensitive Electrical Detection of DNA Hybridization. Nano Res. 2015, 8 (7), 2340–2350. https://doi.org/10.1007/s12274-015-0744-8.

(12) Park, H.; Han, G.; Lee, S. W.; Lee, H.; Jeong, S. H.; Naqi, M.; AlMutairi, A.; Kim, Y. J.; Lee, J.; Kim, W.; Kim, S.; Yoon, Y.; Yoo, G. Label-Free and Recalibrated Multilayer MoS 2 Biosensor for Point-of-Care Diagnostics. ACS Appl. Mater. Interfaces 2017, 9 (50), 43490–43497. https://doi.org/10.1021/acsami.7b14479.

(13) Wang, L.; Wang, Y.; Wong, J. I.; Palacios, T.; Kong, J.; Yang, H. Y. Functionalized MoS 2 Nanosheet-Based Field-Effect Biosensor for Label-Free Sensitive Detection of Cancer Marker Proteins in Solution. Small 2014, 10 (6), 1101–1105. https://doi.org/10.1002/smll.201302081.

(14) Song, P.; Ou, P.; Wang, Y.; Yuan, H.; Duan, S.; Chen, L.; Fu, H.; Song, J.; Liu, X. An Ultrasensitive FET Biosensor Based on Vertically Aligned MoS2 Nanolayers with Abundant Surface Active Sites. Analytica Chimica Acta 2023, 1252, 341036. https://doi.org/10.1016/j.aca.2023.341036.

(15) Ji, Z.; Wei, J.; Luo, F.; Liu, Z.; Lu, H.; Chen, R.; Wang, Y.; Qin, G. Investigating on Sensing Mechanism of MoS 2 -FET Biosensors in Response to Proteins. Nanotechnology 2023, 34 (43), 435503. https://doi.org/10.1088/1361-6528/aceb6a.

(16) Hossain, M. M.; Shabbir, B.; Liu, J.; Wan, Z.; Walia, S.; Bao, Q.; Alan, T.; Mokkapati, S. Bisphenol A Detection Using Molybdenum Disulfide (MoS 2) Field-Effect Transistor Functionalized with DNA Aptamers. Adv Materials Technologies 2023, 8 (11), 2201793. https://doi.org/10.1002/admt.202201793.

(17) Chen, X.; Hao, S.; Zong, B.; Liu, C.; Mao, S. Ultraselective Antibiotic Sensing with Complementary Strand DNA Assisted Aptamer/MoS2 Field-Effect Transistors. Biosensors and Bioelectronics 2019, 145, 111711. https://doi.org/10.1016/j.bios.2019.111711.

(18) Wei, J.; Zhao, Z.; Luo, F.; Lan, K.; Chen, R.; Qin, G. Sensitive and Quantitative Detection of SARS-CoV-2 Antibodies from Vaccinated Serum by MoS 2 -Field Effect Transistor. 2D Mater. 2022, 9 (1), 015030. https://doi.org/10.1088/2053-1583/ac40c4.

(19) De-Eknamkul, C.; Zhang, X.; Zhao, M.-Q.; Huang, W.; Liu, R.; Johnson, A. T. C.; Cubukcu, E. MoS 2 -Enabled Dual-Mode Optoelectronic Biosensor Using a Water Soluble Variant of μ-Opioid Receptor for Opioid Peptide Detection. 2D Mater. 2019, 7 (1), 014004. https://doi.org/10.1088/2053-1583/ab5ae2.

(20) Pham, P. V.; Bodepudi, S. C.; Shehzad, K.; Liu, Y.; Xu, Y.; Yu, B.; Duan, X. 2D Heterostructures for Ubiquitous Electronics and Optoelectronics: Principles, Opportunities, and Challenges. Chem. Rev. 2022, 122 (6), 6514–6613. https://doi.org/10.1021/acs.chemrev.1c00735.

(21) Yoon, J.; Lim, J.; Shin, M.; Lee, S.-N.; Choi, J.-W. Graphene/MoS2 Nanohybrid for Biosensors. Materials 2021, 14 (3), 518. https://doi.org/10.3390/ma14030518.

(22) Pham, P. V.; Bodepudi, S. C.; Shehzad, K.; Liu, Y.; Xu, Y.; Yu, B.; Duan, X. 2D Heterostructures for Ubiquitous Electronics and Optoelectronics: Principles, Opportunities, and Challenges. Chem. Rev. 2022, 122 (6), 6514–6613. https://doi.org/10.1021/acs.chemrev.1c00735.

(23) Azadmanjiri, J.; Srivastava, V. K.; Kumar, P.; Sofer, Z.; Min, J.; Gong, J. Graphene-Supported 2D Transition Metal Dichalcogenide van Der Waals Heterostructures. Applied Materials Today 2020, 19, 100600. https://doi.org/10.1016/j.apmt.2020.100600.

(24) Xu, H.; Wu, J.; Feng, Q.; Mao, N.; Wang, C.; Zhang, J. High Responsivity and Gate Tunable Graphene-MoS 2 Hybrid Phototransistor. Small 2014, 10 (11), 2300–2306. https://doi.org/10.1002/smll.201303670.

(25) Vázquez Sulleiro, M.; Develioglu, A.; Quirós-Ovies, R.; Martín-Pérez, L.; Martín Sabanés, N.; Gonzalez-Juarez, M. L.; Gómez, I. J.; Vera-Hidalgo, M.; Sebastián, V.; Santamaría, J.; Burzurí, E.; Pérez, E. M. Fabrication of Devices Featuring Covalently Linked MoS2–Graphene Heterostructures. Nat. Chem. 2022, 14 (6), 695–700. https://doi.org/10.1038/s41557-022-00924-1.

(26) Kim, T.; Fan, S.; Lee, S.; Joo, M.-K.; Lee, Y. H. High-Mobility Junction Field-Effect Transistor via Graphene/MoS2 Heterointerface. Sci Rep 2020, 10 (1), 13101. https://doi.org/10.1038/s41598-020-70038-6.

(27) Han, T.; Liu, H.; Chen, S.; Wang, S.; Yang, K. Construction and Electrical Performance Improvement of MoS 2 FET with Graphene/Metal Contact. Opt. Mater. Express 2021, 11 (9), 3099. https://doi.org/10.1364/OME.431806.

(28) Pham, T.; Ramnani, P.; Villarreal, C. C.; Lopez, J.; Das, P.; Lee, I.; Neupane, M. R.; Rheem, Y.; Mulchandani, A. MoS2-Graphene Heterostructures as Efficient Organic Compounds Sensing 2D Materials. Carbon 2019, 142, 504–512. https://doi.org/10.1016/j.carbon.2018.10.079.

(29) Cho, B.; Yoon, J.; Lim, S. K.; Kim, A. R.; Kim, D.-H.; Park, S.-G.; Kwon, J.-D.; Lee, Y.-J.; Lee, K.-H.; Lee, B. H.; Ko, H. C.; Hahm, M. G. Chemical Sensing of 2D Graphene/MoS 2 Heterostructure Device. ACS Appl. Mater. Interfaces 2015, 7 (30), 16775–16780. https://doi.org/10.1021/acsami.5b04541.

(30) Ignatova, T.; Pourianejad, S.; Li, X.; Schmidt, K.; Aryeetey, F.; Aravamudhan, S.; Rotkin, S. V. Multidimensional Imaging Reveals Mechanisms Controlling Multimodal Label-Free Biosensing in Vertical 2DM-Heterostructures. ACS Nano 2022, 16 (2), 2598–2607. https://doi.org/10.1021/acsnano.1c09335.

(31) Moudgil, A.; Singh, S.; Mishra, N.; Mishra, P.; Das, S. MoS 2 /TiO 2 Hybrid Nanostructure-Based Field-Effect Transistor for Highly Sensitive, Selective, and Rapid Detection of Gram-Positive Bacteria. Adv Materials Technologies 2020, 5 (1), 1900615. https://doi.org/10.1002/admt.201900615.

(32) Samy, O.; Zeng, S.; Birowosuto, M. D.; El Moutaouakil, A. A Review on MoS2 Properties, Synthesis, Sensing Applications and Challenges. Crystals 2021, 11 (4), 355. https://doi.org/10.3390/cryst11040355.

(33) Chrimes, A. F.; Khoshmanesh, K.; Stoddart, P. R.; Mitchell, A.; Kalantar-zadeh, K. Microfluidics and Raman Microscopy: Current Applications and Future Challenges. Chem. Soc. Rev. 2013, 42 (13), 5880. https://doi.org/10.1039/c3cs35515b.

(34) Huo, N.; Konstantatos, G. Recent Progress and Future Prospects of 2D-Based Photodetectors. Advanced Materials 2018, 30 (51), 1801164. https://doi.org/10.1002/adma.201801164.

Chapter 2

Two-Dimensional Molybdenum Disulfide-Based Flexible Optoelectronic Biosensors for Fast and Selective Detection of Human Immunoglobulin G

2.1 Introduction

Sensitive, specific, and rapid identification of biological molecules is critical to the biosensor's development. Nanoscience and nanotechnology provide an essential optional platform to develop rapid responsiveness, higher sensitivity and selectivity, and lower limit of detection for biosensors. Extensive efforts have been put into the development of nanomaterials based biosensors.[1–3] Field-Effect Transistors (FETs) are sensitive to the local surface charge by density changes inside of the semiconductors. Therefore, they could be used to monitor dynamic binding of target processes and further application of diagnosis for point-of-care testing. Biosensors that combines bio-receptors with ion-sensitive FETs are one of the most fundamental and widely researched types within the diverse array of biosensing technologies.[4–6]

Two-dimensional (2D) thin-film materials are crucial to the advancement of FET-based biosensor technology.[7,8] Molybdenum disulfide (MoS_2) is the highest profile 2D semiconducting material among atomically thin layered transition metal dichalcogenides family.[9,10] Layered MoS_2 thin films show excellent electrical and optical properties and have found vast application in the field of, catalysis, energy, optoelectronics, electronics, and biomedical areas in the past few years.[11]

The MoS_2-based FETs, combined the 2D nanomaterials and nanotechnology, has captured researchers' attention due to their appealing features, including the ability for label-free rapid electrical detection capabilities, minimal power usage, compact design, and the potential for seamless on-chip integration with measurement systems.[11] Recent advancements feature MoS_2-based gas sensors capable of detecting NH_3, NO, NO_2, and a range of volatile organic compounds. [12–14] Additionally, MoS_2-based FETs were also designed as biosensors for the identification of DNA and proteins, targeting biomarkers associated with bladder cancer, such as nuclear matrix protein 22 and cytokeratin 8, and markers for prostate cancer, including the prostate-specific antigen.[15–18] These reports show good sensitivity and limit of detection, however, these MoS_2-based FET sensors experienced a very low current output (in low picoampere) due to a high device resistance because of high MoS_2 resistivity and a large contact resistance.[19] Therefore, MoS_2-based FET biosensors very often need high bias to guarantee that the transistor remains active throughout the biosensing procedure.[20,21] One concern for those applications is that these MoS_2-based FET sensors all needed a high top or back gate voltage applied across the sensor terminals with a solid gate or a suspended gate. This fabrication of gate processes increases the consumption of energy, but also needs a complicated microfabrication process for the gating terminals in a clean room to not cause an extra waste of time and material.

A promising improvement strategy involves harnessing the photoresponse characteristics of MoS_2 to enhance the efficacy of MoS_2-based FET sensors.[22] When MoS_2 is illuminated with light whose energy equals or exceeds this band gap, it generates a substantial number of photocarriers.[22,23] It is reported that photoresponse in MoS_2-based devices arises due to the change in the conductivity after illumination.[24] Tung et al. utilize red LED Illumination to induce a photocurrent, and the generated photocurrent is then utilized for NO_2 gas sensing. By this way, MoS_2 channel resistance experienced a thousandfold decrease.[25] Peng and colleagues developed a flexible sensor by integrating a monolayer MoS_2 channel onto a Kapton substrate, creating flexible MoS_2/Kapton heterointerfaces for relative humidity detection.[26] When using 325 nm UV photoexcitation, the MoS_2/Kapton sensor exhibited a significant increase in photocurrent, achieving a photocurrent to dark current ratio of 3.87×10^5. This achievement underscores the effectiveness of optimizing photocurrent charge transfer between 2D materials and photoabsorbing substrates as a strategy for enhancing the performance of sensing applications.

In this paper, we report a sensitive MoS_2 FET optoelectronics biosensor for real-time protein detection in liquid-phase. We deposited a layer of Al_2O_3 by using ALD method to encapsulate MoS_2 with the help of a durable protective passivation layer and provide a coating layer for biofunctionalization. (3-aminopropyl) Triethoxysilane

(APTES) and glutaraldehyde are utilized to immobilize antibody on the Al_2O_3 encapsulated MoS_2-based platform. Within this study, the sensing of HIgG antigen as target with HIgG antibody as receptor will be used as a model system. A LED emitting visible red light (λ = 650 nm), which matches the band gap of single-layer MoS_2, is utilized as the source of light irradiation in the system. Transparent and flexible Kapton was used as a substitute for silicon wafers as substrate which is not only helpful for the application of the light source in the microfluidics system, but also a cost-saving material compared with Si/SiO_2 wafer. The output current change in the MoS_2 transistor is due to the specific binding of HIgG proteins to the immobilized antibodies on the device surface. Furthermore, exciting the MoS_2 channel of an FET by a low energy red LED during the sensing process will increase the current output and thereby improve the sensing response. Our experimental findings underscore the remarkable sensitivity and rapid detection capabilities of MoS_2-based optoelectronic biosensors for HIgG. Additionally, the biosensor exhibits excellent specificity with negligible signals in response to non-target proteins in both simple and complex matrices. This study highlights the potential of biofunctionalized MoS_2-based flexible optoelectronics for identifying different biomolecules and biomarkers in advancing the early disease diagnostics.

2.2 Experimental section

2.2.1 Chemicals and instruments

1 MIL 25 μm Kapton film was purchased from Cole-Parmer. The thermally grown 300 nm thick SiO_2 silicon wafers were purchased from Ultrasil LLC. All reagents were purchased from Fisher Scientific unless noted otherwise. Sulfur, molybdenum trioxide (MoO_3), APTES, and glutaraldehyde were obtained from Sigma-Aldrich. All antibodies and antigens, including anti-HIgG antibody, HIgG protein, bovine serum albumin (BSA), and human serum albumin (HSA), were acquired from Sigma-Aldrich.

Electrical measurements were performed via a Keithley source meter (Model 2636). Raman and Photoluminescence (PL) spectra were collected on Horiba LabRam system using a green laser with wavelength of 532 nm. The surface morphology was performed by a Aist-NT Atomic Force Microscopy (AFM) system. Surface roughness was measured within 3 μm × 3 μm image using tapping mode. Root-mean-square (RMS) roughness is calculated by the Aist-NT software considers both microscopic peaks and valleys in the surface topography. Optical microscope (OM) image was obtained by Hirox KH-7700 digital microscope.

2.2.2 Material and device fabrication

MoS_2 synthesis. MoS_2 was synthesized with sulfur and MoO_3 powders as precursors in a tube furnace system). The MoS_2 synthesis using a chemical vapor deposition (CVD) method involved a two-zone tube furnace system (Lindberg/Blue,

Mini-Mite, Thermo Scientific) with temperatures setting at 170°C for sulfur and 725°C for MoO_3 to grow 20 min. Argon was applied as carrier gas. After unloading the sample from the tube furnace, as-fabricated MoS_2 on Si/SiO_2 substrate was coated with polystyrene (PS) and the film was delaminated by 1 M potassium hydroxide solution followed with thorough washing with deionized water to remove residues.

Device fabrication. The standard photolithographic patterning process was performed using a Karl Suss MicroTech mask aligner (Model MA6, SÜSS MicroTec SE). Following this step, Cr/Au (5/50 nm) metal contact pads were deposited using an e-beam evaporator (Temescal BJD-1800) on the Kapton substrate. The MoS_2/PS film was transferred ontop, serving as the semiconductor within a channel measuring 10 μm by 10 μm. Following the removal of PS in toluene, a 30 nm Al_2O_3 layer was deposited in an ALD system (Cambridge Nanotech Savannah 100, Veeco). The deposition of the Al_2O_3 layer involved subjecting the substrate to a temperature of 250°C for 300 cycles, employing trimethylaluminum and water as the precursor materials.

2.2.3 Functionalization

The Al_2O_3 passivated MoS_2-based device was treated with ammonium hydroxide (NH_4OH) for 30 min. Subsequently, the device was soaked in 1 mL of APTES for 60 min and then extensively cleansed with ethanol. Following this, the amine functional groups on APTES underwent a reaction with a solution of 4 mL of 25% glutaraldehyde

for two hours. The device was incubated overnight at 4 °C with 20 µL of 50 µg/mL anti-HIgG in 10 mM in phosphate buffer (PB) to immobilize the antibody on the surface. It was followed by quenching with 20 µL of 10% ethanolamine. All the above steps were done at room temperature except the anti-HIgG immobilization step. A schematic diagram of biofunctionalization and detection of biomolecules on Kapton substrate is shown in Figure 2.1a. These functionalization steps were evaluated through current-voltage (I-V) curves without gate voltage application.

2.2.4 Biosensing of HIgG

The detection of HIgG served as a model for evaluating the biosensing capabilities of MoS_2 optoelectronic biosensors. These experiments were conducted in a microfluidic system (Figure 2.1b) with a 30 µL customized PMMA cell. The dynamic electrical resistance change was continuously monitored while various analytes were injected into the sensor. This monitoring occurred at a fixed source-drain voltage (V_D = 1 V), without applying any gate voltage, allowing for the evaluation of the biosensor's response to the analytes in real-time. A red LED light, with a central wavelength of 650 nm and output power of 5 mW (UMLIFE US), was incorporated at the bottom of the cell within the biosensing microfluidics system. This setup aimed to enhance the detection capabilities of the system by providing optimal illumination conditions for the biosensing process. The performance of the biosensing system was also evaluated

by comparing detections under conditions with and without illumination. Various concentrations of HIgG (from 10 ng/mL to 10^6 ng/mL in PB solution) were tested to determine analytical figures of merits of dynamic range, sensitivity, and limit of LOD.

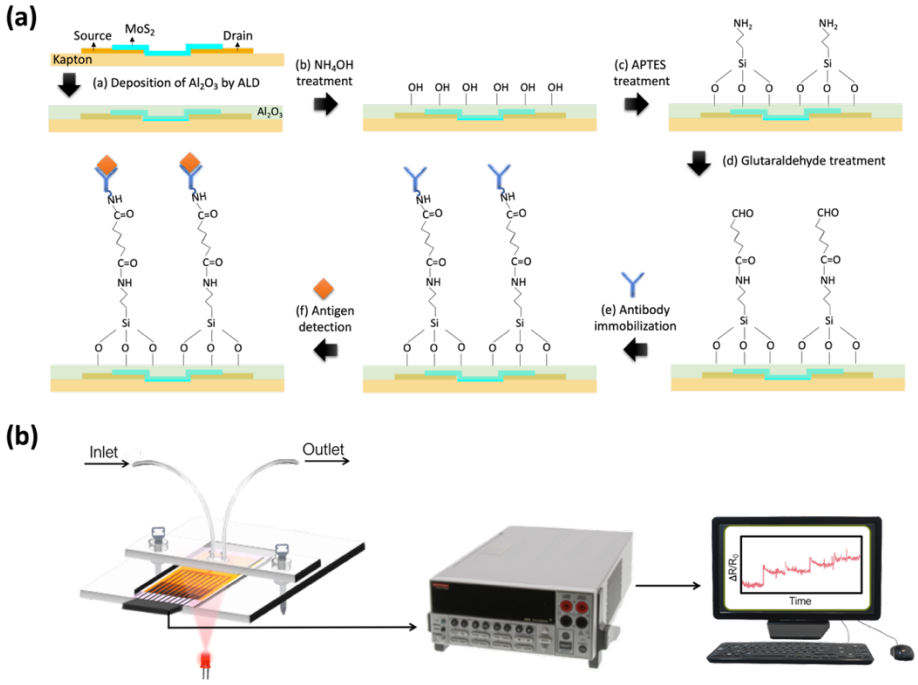

Figure 2.1. (a) Schematic representation of detection of biomolecules on Kapton substrate based optoelectronic biosensors. The processes involve: a. deposition of Al_2O_3 by ALD; b. ammonium hydroxide treatment; c. generation of silane layer with APTES solution; d. reaction with glutaraldehyde solution; e. antibody immobilization; f. detection of antigen. (b) Schematic of microfluidic biosensing system.

To test the suitability of the MoS_2 flexible optoelectronic biosensor for detection of HIgG in a real environment, the biosensor was employed for detecting HIgG within an artificial urine (AU) matrix with a pH of 7.4.[27] Following each detection of HIgG analytes, the MoS_2-based biosensor underwent a washing process using a PB solution.

This step was essential to recover the biosensor's responsiveness after exposure to environments with high ionic strength, ensuring accurate subsequent measurements.

The BSA and HSA proteins were chosen as the control group to assess the specificity of the fabricated sensing platform for detecting HIgG. Each protein was individually introduced into the detection system following the same detection process.

2.3 Results and discussion

2.3.1 MoS_2 characterizations

A large-area and continuous MoS_2 film can be achieved (Figure 2.2a) by the CVD method. Within the continuous film's perimeter, isolated triangular MoS_2 with dozens of micrometer lateral sizes was visible via OM image. Some boundaries were formed because of the triangular MoS_2's convergence. The size of these triangular grains ranged from 7 to 90 μm and a thin film with lateral size more than 500 μm was observed as well. The thickness of this MoS_2 was further measured using AFM. As shown in Figure 2.2b, the step size between the surface of the triangle and SiO_2 substrate is about 0.9 nm, which agrees to 1–2 layers of MoS_2.[28] As shown in Figure 2.2c, Raman spectra of MoS_2 indicates clearly the E_{2g} (399 cm^{-1}) and A_{1g} (419 cm^{-1}) peaks corresponding to the in-plane and out-of-plane vibration modes, respectively. The CVD grown MoS_2 exhibits an intense photoluminescence at around 1.84 eV as shown in Figure 2.2d, which is consistent with the literature reports.[29]

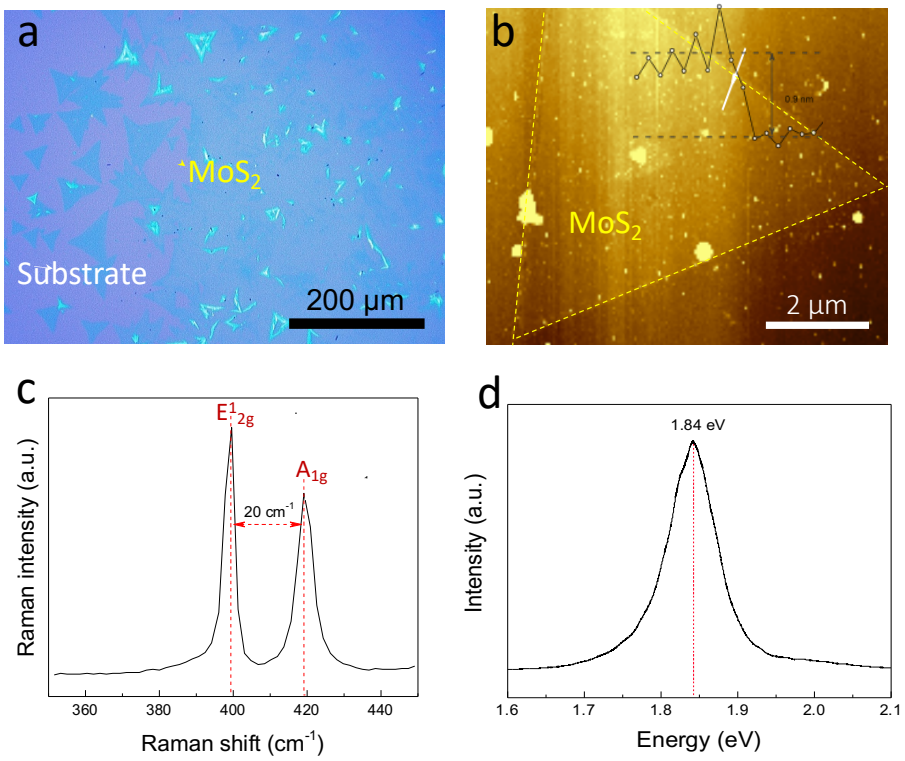

Figure 2.2. (a) OM image and (b) AFM image of the transferred MoS_2 on the Si/SiO_2 substrate. The inset plot in (b) is the corresponding height profile of the transferred MoS_2 on the Si/SiO_2 substrate. (c) Raman spectra and (d) PL spectrum of MoS_2 samples. The excitation wavelength is 532 nm.

2.3.2 Device characterization

Figure 2.3a shows I-V curves of the as-grown CVD MoS_2 and Al_2O_3 passivated device. The bare MoS_2 exhibits low charge mobility and the high contact resistance at MoS_2/gold interface. The bare MoS_2 showed numerous sulfur vacancies, especially at boundaries and edges, leading to trapped electrons and reduced electron mobility due to its semiconducting natural properties and large work function. To address this, our prior work demonstrated an effective approach through the physical passivation of

MoS_2 by applying an ALD-grown Al_2O_3 layer, which mitigates the adverse effects of these vacancies.[30] The introduction of an Al_2O_3 film passivation layer markedly improved performance, amplifying a minimal current of 16 nA at V_D = 1 V to an impressive 600 nA, which is a 37-fold increase in magnitude. This enhancement illustrates the impact of surface passivation on improving electrical conductivity and interface efficiency in semiconducting devices. This physical passivation layer of Al_2O_3 not only minimizes the intercalation of water molecules through MoS_2 grain boundaries leading to delamination of MoS_2 in aqueous solutions, but also passivates sulfur vacancy defects with a strong n-doping effect. This strategy significantly improves the device's electrical performance through heightened charge mobility and current flow, leading to more efficient electrical testing that requires lower power. By eliminating the need of a gate and reducing the source-drain voltage, the method simplifies device fabrication and operation, leading to devices that are not only more energy-efficient but also easier to produce and use.

To explore the response of the device and study photo responsive behavior, a red LED was incorporated into the setup as the illumination source. When MoS_2 was illuminated with a red light, many photocarriers were generated and showed photoresponse behavior in the MoS_2 FET platform. The terms "light" and "dark" states were used to describe conditions with and without light exposure. Figure 2.3b showed

the photocurrent response/output of the optoelectronic transduction device in air when the light was introduced from the bottom. There was a quick initial surge in current, achieving approximately a 75% increase in photocurrent within a few seconds upon the light turning on. This was followed by a more gradual rise that persisted for several hundred seconds, indicated a two-phase response to light exposure with both rapid and slow components in the current's behavior. MoS_2, as a conducting channel, showed a typical n-type behavior. Under illumination, the photogenerated electron-hole pairs were separated. The charge separation results in an increase of electron concentration in the conduction band. As a result, the magnitude of current in such a device was directly proportional to the concentration of electrons in MoS_2, which in turn increased the current in the device. When the LED was switched off, the current exhibited a slow decay pattern, initially dropping quickly to below 75% of its peak level within a few seconds and was then followed by a prolonged, gradual decline.

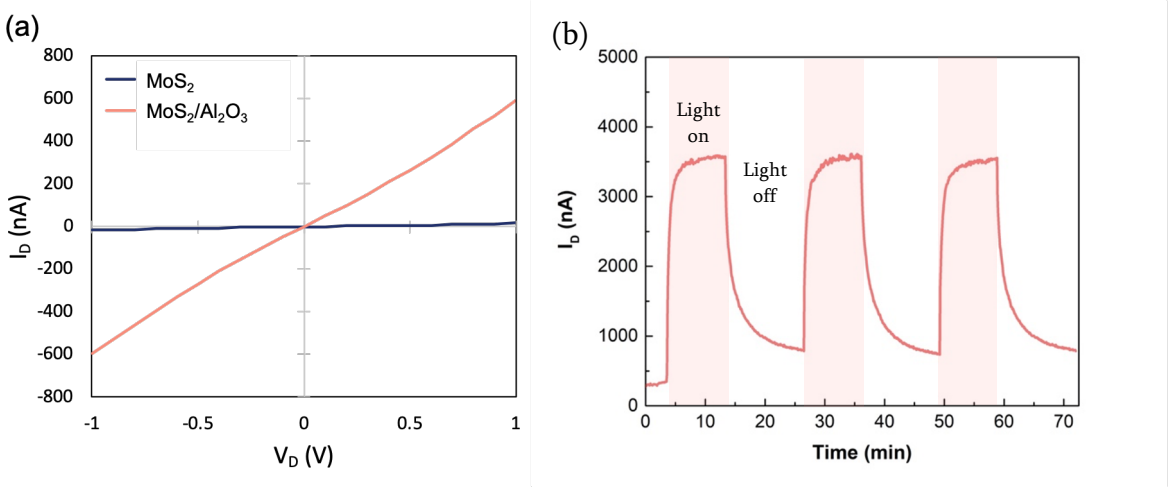

Figure 2.3. (a) I-V curves of as-grown CVD MoS_2 and Al_2O_3 passivated devices. (b) Photocurrent pulses as a response to red LED for Al_2O_3 passivated device. It was measured at V_D = 1V.

2.3.3 Develop optoelectronic MoS_2 biosensors on flexible substrate

The as-fabricated devices were further functionalized to develop biosensors for liquid-phase applications. Each of these functionalization steps were evaluated through I-V curves as shown by characteristics of a representative device in Figure 2.4. I-V curves were linear in V_D range of -1 to 1 V, which suggested that the electrode-channel contact to be ohmic. As -OH groups were sufficiently activated on the surface, they behaved like a negative surface gate on the device, which resulted in a decrease in current after ammonium hydroxide treatment. After antibody conjugation to the device surface via linkers, a significant reduction was observed in the slope of the I-V curve compared with the Al_2O_3 passivated device. The conjugation of biomolecules to

linkers on the device resulted in pronounced changes in the slopes of I-V curves, indicating a significant increase in device resistance. The observed change in electrical resistance due to biomolecule conjugation was linked to the larger size of protein molecules compared to the linkers. After subsequent quenching and blocking steps, there was a slight increase in the slope of the I-V curve, indicating enhanced conductance in the FET channel. This change was attributed to the blocking of the antibody's active end, which altered the local environment at the FET surface. Consequently, this modification affected the carrier density, leading to a reduction in resistance.[31]

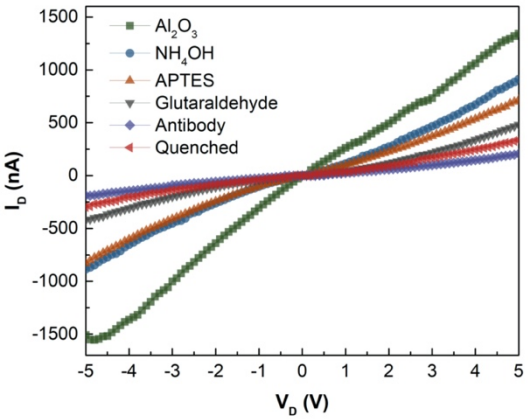

Figure 2.4. I-V curves of a representative Al_2O_3 passivated MoS_2-based device at different functionalization steps. Measurements were from -5 V to +5 V with step size of 0.1 V with red light illumination from bottom.

We analyzed the surface using AFM to investigate the surface morphology and roughness changes upon different functionalization steps. Figure 2.5 presented AFM

images capturing the surface morphology at various stages of the biofunctionalization process: Al_2O_3 passivated surface, Al_2O_3 passivated surface with APTES silanization, surface reacted with glutaraldehyde, and the immobilization of anti-HIgG antibody. Continuous and flat Al_2O_3 films were deposited on MoS_2 with extracted RMS values of 1.72 nm, as shown in Figure 2.5a. After the silanization process with APTES, an increase of roughness to 2.43 nm was noted in surface, indicating changes in the substrate's physical texture due to the treatment (Figure 2.5b). We observed that a compact and highly dense layer on the Al_2O_3 passivated surface in Figure 2.5c, which indicated the surface's textural alteration due to the glutaraldehyde. This indicated that glutaraldehyde not only reacts with the amine groups but also aids in reducing surface roughness by leveling out the clefts.[32] Subsequent to the immobilization of antibodies, there was an increase in surface roughness to 2.89 nm which is attributed to the size and distribution of the antibodies creating a more complex surface topography (Figure 2.5d).

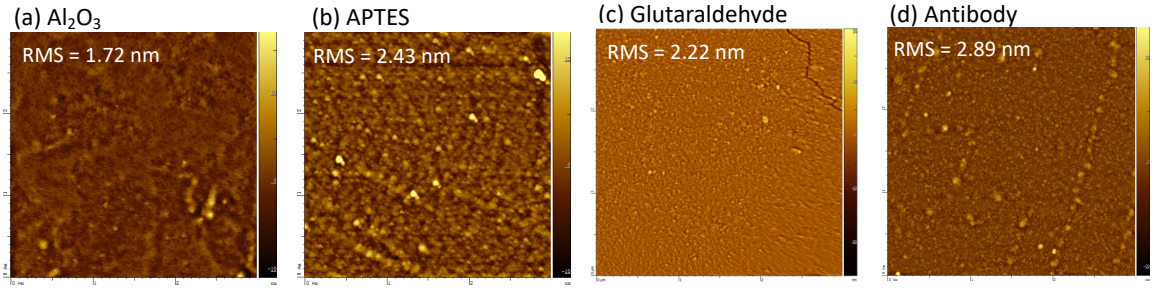

Figure 2.5. AFM and roughness parameters of the device at different biofunctionalization steps. The size of the scanning area is 3 μm × 3 μm.

2.3.4 Response of the biosensors in simple matrix

The biofunctionalized devices were utilized in a microfluidic setup (as depicted in Figure 2.1b) to detect varying concentrations of HIgG antigen in PB solution. In Figure 2.6a, the observed resistance fluctuations were due to the physical action of injecting solutions, but the post-stabilization increases in resistance values were attributed to the HIgG antigens binding to the receptors on the surface. Noticeably compared without illumination, the response to HIgG analyte solution under illumination was enhanced dramatically for each concentration. Figure 2.6b's calibration curves demonstrated that the resistance change directly correlates with HIgG concentration, showing a consistent linear response across a wide range of concentrations from 10 ng/mL to 10^6 ng/mL. Additionally, the curves illustrated the variation of the relative response $\Delta R/R_0$ in both with and without illumination conditions as a function of the HIgG concentration (Log[ng/mL]) on a logarithmic scale. The device's sensitivity is determined by the slope of this variation. Under red light illumination, the high sensitivity of 0.115 per Log[ng/mL] was observed, which was as 2.4 times as high of sensitivity without illumination of S = 0.047 per Log[ng/mL]. The calculation of theoretical LOD based on a response three times higher than the noise level and followed the same method described in our previous work.[30] Root-mean-square value of sensing process with and without illumination were 0.0337 and 0.0303

as shown in Figure 2.6b (inset). Therefore, the LODs were estimated to be 7.57 ng/mL and 85.9 ng/mL for sensing processes with and without illumination, respectively. The narrow error margins indicated high reproducibility, confirming the biosensor's consistent and reliable capability in HIgG detection.

Control experiments were conducted with nonspecific antigens to confirm the specificity of the interaction, demonstrating that the detected changes are a direct consequence of the specific antibody adhering to the antigen on the surface. First, a non-antibody immobilization MoS_2-based device did not show changes in conductance upon the addition of various concentrations of HIgG solutions. (Figure 2.6c). Second, even after additions of high concentrations (10^2-10^6ng/mL) of BSA and HSA, which were not specific for anti-HIgG, the conductance of the biofunctionalized sensor did not show any response, whereas subsequent addition of HIgG solutions produce a conductance drop, as observed in Figure 2.6d. Third, the addition of PB solutions did not result in change in conductance for the biofunctionalized MoS_2-based device (Figure 2.6d). All above results were indicative of the specificity of our biosensors for HIgG biomarkers.

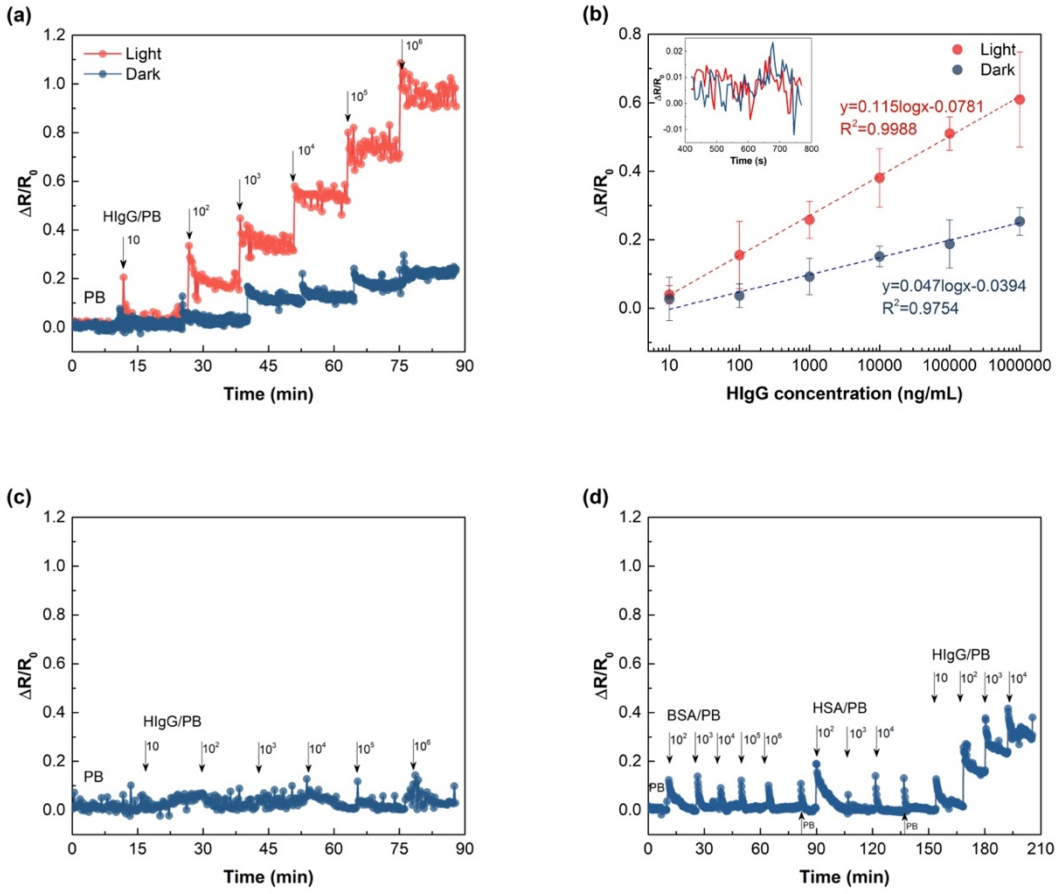

Figure 2.6. (a) Real-time monitoring of the changes in resistance for HIgG sensing and the priming process with 10 mM PB (V_D = 1 V) with and without illumination. (b) Calibration curve of Al_2O_3 passivated MoS_2-based sensor with and without illumination. Data points are an average of 3 measurements and error bars represent ±1 SD. Inset shows a temporal trace of experimentally recorded noise of $\Delta R/R_0$ with (red line) and without (blue line) illumination. (c) Real-time monitoring of the changes in resistance for control experiments with red light illumination from bottom, showed a negative control sensing process not functionalized with anti-HIgG but quenched with ethanolamine. (d) Real-time monitoring of the changes in resistance with different biomolecules solutions additions, which are measured with red light illumination from bottom. R_0 is defined as the resistance of the device after priming with PB and ΔR is a resistance change caused by affinity binding of HIgG antigen-antibody interaction.

2.3.5 Response of the biosensors in artificial urine matrix

There is a high demand of a biosensor that can be used directly with physiological samples. To demonstrate the biosensor's practical application in biomedical diagnostics, the MoS_2-based flexible optoelectronic biosensor was further used to detect the HIgG in real-life human body fluids environment with red light illumination from bottom. To mimic real-world conditions, an AU medium with a pH of 7.4 was utilized. Upon injecting the AU into the system, Figure 2.7a showed a significant reduction in resistance. This decrease was attributed to the high salt content in the AU medium, which increased the solution's electrical conductivity. In high salt solutions, ions accumulated at the interface and a high capacitance of electrical double layer region formed at the solid-liquid interface.[33] It led to higher density of the negative ions accumulated on the passivated surface, which caused a higher density of positive ions accumulated on the surface of the active channel and a larger increase in the electron concentration.[34] This resulted in detections responses that were not readable. Consequently, to mitigate this high ionic environment and restore the MoS_2-based biosensor's sensitivity to antigen-antibody interactions, a washing step using PB solution was demanded. This procedure was critical for ensuring the biosensor's functionality by reducing the ionic strength and enhancing the detection of specific binding events. The recovered responses showed excellent agreement with the

responses in PB as shown in Figure 2.6a. The calibration curves were shown in Figure 2.7b, which gave linear regression between concentration and the resistance change. The measurement also demonstrated a high sensitivity level of 0.141 per Log[ng/mL] after PB washing with recovered signal. Further, control experiments were conducted to confirm the observed results were due to specific antibody binding to the surface antigen. The non-antiHIgG modified MoS_2-based device did not show changes in conductance following the addition different concentrations of HIgG in AU solutions (Figure 2.7c). Also, addition of blank AU solution (Figure 2.7d) and non-target BSA analyte in AU solutions (Figure 2.7e) did not result in conductance change after PB washing.

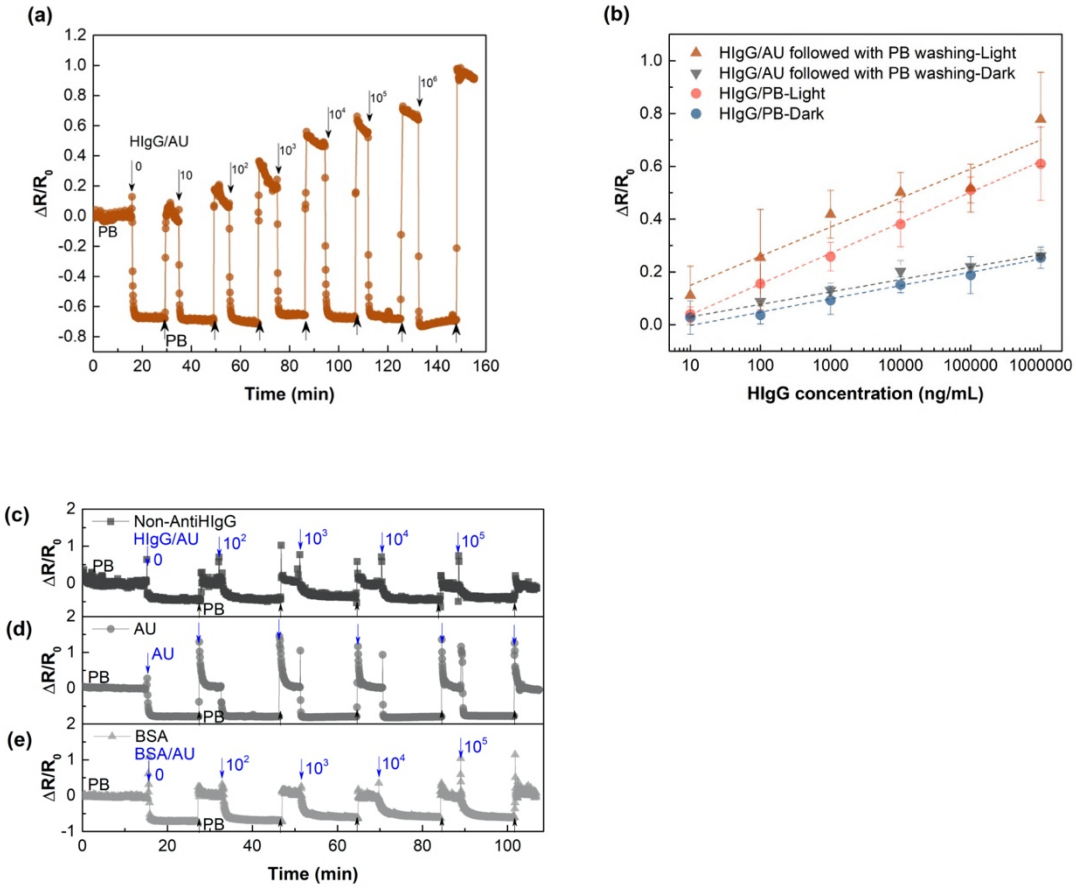

Figure 2.7. (a) Real-time monitoring of the changes in resistance for HIgG sensing in AU with 10 mM PB wash (V_D = 1 V). (b) Calibration curve of Al_2O_3 passivated MoS_2-based sensor. Data points are an average of 5 measurements and error bars represent ±1 SD. (c) Real-time monitoring of the changes in resistance for control experiments. All experiments were conducted in AU solution with red light illumination from bottom. R_0 is defined as the resistance of the device after priming with AU.

2.3.6 Reliability of flexible electronics in static bending test

As the demand for the reliability of flexible systems increases, it's necessary to assess the mechanical stability of biosensors. This underscores the importance of conducting evaluations to ensure that these flexible systems can withstand static

stresses and maintain their functionality over time. Herein, a simple static bending test was conducted to investigate the reliability of flexible electronics to provide an optional application in the wearable sensors field.[35] The flexible electronics were bent over a tube with a defined radius of 25 mm (Figure 2.8a, insert image). The test using 30 min interval time between positions and tests, the I-V curves and resistance were measured. As displayed in Figure 2.8a, during the 210 min static bending, the flexible electronic was still functional and produce typical linear I-V curves all the time. Figure 2.8b illustrated the resistance experienced a gradual increase in 150 min static bending and remained in a similar range after 150-210 min at relaxed positions. This suggested that the devices initially experienced physical deterioration within the first 150 min but subsequently achieved a stable operational state after this period. In addition, the same device was tested after being bended on the tube for 210 min in ambient condition, showing comparable response as the original device in both light and dark conditions for 10^3 ng/mL and 10^4 ng/mL HIgG analytes detections (Figure 2.8c). This confirms the device has a good reliability for flexible biosensing applications.

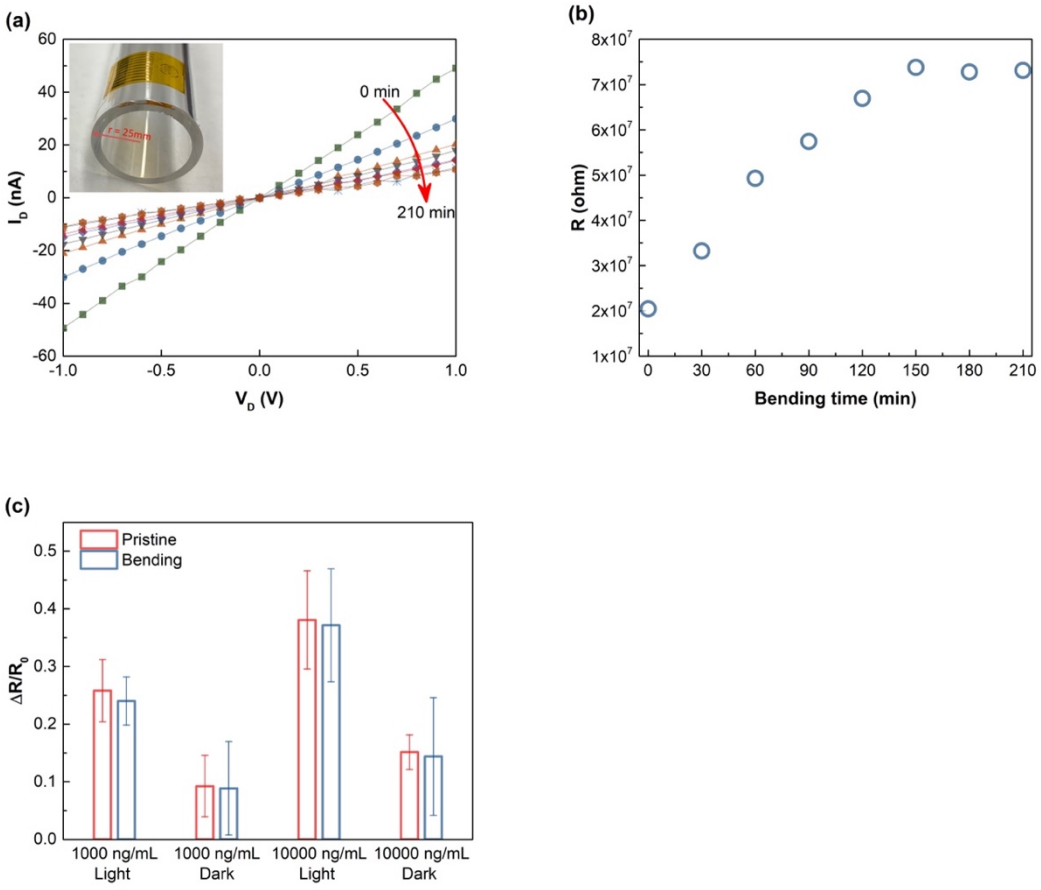

Figure 2.8. Flexible electronics performance with bending test (a) I-V curves (V_D = 1 V) and (b) changes of resistance upon static bending time. (c) Biosensing responses with pristine device and devices after 210 min bending test for the 10^3 ng/mL and 10^4 ng/mL HIgG analyte detections.

2.4 Conclusions

In conclusion, 2D MoS_2-based optoelectronic biosensors with low energy visible red-light excited on a flexible substrate has been achieved in this work. The detection of HIgG served as a model for evaluating the biosensing capabilities of MoS_2 optoelectronic biosensors. The biosensor showed a fast and selective detection of HIgG with varying concentration from 10 to 10^6 ng/mL with a LOD of 85.9 ng/mL. By

introducing a visible red light, the biosensing performance was enhanced with a lower LOD of 7.57 ng/mL. Under red light illumination, the high sensitivity of 0.115 per Log[ng/mL] was observed, which was 2.4-fold greater than the sensitivity without illumination of 0.047 per Log[ng/mL]. It demonstrated that the Kapton based MoS_2 optoelectronics significantly enhancing the efficiency of sensing applications by improving the charge carrier dynamics, leading to faster and more sensitive detection capabilities in and biosensors in liquid-phase without applied gate voltage. Moreover, the MoS_2-based optoelectronic biosensors platform had shown high sensitivity and selectivity in both simple matrix and complex artificial urine sensing matrix. In addition, the flexible electronics showed good reliability in long time static bending tests and had comparable response as the pristine device in both light and dark conditions for HIgG analytes detections. This fundamental work paves the way to further expected improvement of the sensitivity of such biosensors using MoS_2-based optoelectronic to any biomarker of interest in an easier way. Furthermore, it shows enormous potential for flexible and wearable sensors applications.

2.5 References

(1) Ibau, C.; Md Arshad, M. K.; Subash C.B., G. Current Advances and Future Visions on Bioelectronic Immunosensing for Prostate-Specific Antigen. *Biosensors and Bioelectronics* **2017**, *98* (June), 267–284.

(2) Seo, G.; Lee, G.; Kim, M. J.; Baek, S. H.; Choi, M.; Ku, K. B.; Lee, C. S.; Jun, S.; Park, D.; Kim, H. G.; Kim, S. J.; Lee, J. O.; Kim, B. T.; Park, E. C.; Kim, S. Il. Rapid Detection of COVID-19 Causative Virus (SARS-CoV-2) in Human Nasopharyngeal Swab Specimens Using Field-Effect Transistor-Based Biosensor. *ACS nano* **2020**, *14* (4), 5135–5142.

(3) Shen, Y.; Bin, T.; Mulchandani, A. Current Status, Advances, Challenges and Perspectives on Biosensors for COVID-19 Diagnosis in Resource-Limited Settings. *Sensors and Actuators Reports* **2021**, *3* (December 2020), 100025.

(4) Syedmoradi, L.; Ahmadi, A.; Norton, M. L.; Omidfar, K. A Review on Nanomaterial-Based Field Effect Transistor Technology for Biomarker Detection. *Microchimica Acta* **2019**, *186* (11), 739.

(5) Syu, Y.-C.; Hsu, W.-E.; Lin, C.-T. Review—Field-Effect Transistor Biosensing: Devices and Clinical Applications. *ECS Journal of Solid State Science and Technology* **2018**, *7* (7), 3196–3207.

(6) Vu, C. A.; Chen, W. Y. Field-Effect Transistor Biosensors for Biomedical Applications: Recent Advances and Future Prospects. *Sensors* **2019**, *19* (19), 1–22.

(7) Wen, W.; Song, Y.; Yan, X.; Zhu, C.; Du, D.; Wang, S.; Asiri, A. M.; Lin, Y. Recent Advances in Emerging 2D Nanomaterials for Biosensing and Bioimaging Applications. *Materials Today* **2018**, *21* (2), 164–177.

(8) Su, S.; Sun, Q.; Gu, X.; Xu, Y.; Shen, J.; Zhu, D.; Chao, J.; Fan, C.; Wang, L. Two-Dimensional Nanomaterials for Biosensing Applications. *TrAC - Trends in Analytical Chemistry* **2019**, *119*, 115610.

(9) Yadav, V.; Roy, S.; Singh, P.; Khan, Z.; Jaiswal, A. 2D MoS2-Based Nanomaterials for Therapeutic, Bioimaging, and Biosensing Applications. *Small* **2019**, *15* (1), 1–33.

(10) Lembke, D.; Bertolazzi, S.; Kis, A. Single-Layer MoS2 Electronics. *Accounts of Chemical Research* **2015**, *48* (1), 100–110.

(11) Shaswat Barua, Hemant Sankar Dutta, Satyabrat Gogoi, Rashmita Devi, R. K. Nanostructured MoS2-Based Advanced Biosensors: A Review. *ACS applied nano materials* **2018**, *1* (1), 2–25.

(12) Zhao, Y.; Song, J. G.; Ryu, G. H.; Ko, K. Y.; Woo, W. J.; Kim, Y.; Kim, D.; Lim, J. H.; Lee, S.; Lee, Z.; Park, J.; Kim, H. Low-Temperature Synthesis of 2D MoS2 on a Plastic Substrate for a Flexible Gas Sensor. *Nanoscale* **2018**, *10* (19), 9338–9345.

(13) Chen, J.; Li, H.; Liang, T.; Wang, H. Research Progress of Molybdenum Disulfide Field-Effect Transistor Biosensors. In *International Conference on Optoelectronic and Microelectronic Technology and Application*; 2020; p 12.

(14) Guo, J.; Wen, R.; Zhai, J.; Wang, Z. L. Enhanced NO2 Gas Sensing of a Single-Layer MoS2 by Photogating and Piezo-Phototronic Effects. *Science Bulletin* **2019**, *64* (2), 128–135.

(15) Wang, T.; Zhu, R.; Zhuo, J.; Zhu, Z.; Shao, Y.; Li, M. Direct Detection of DNA below Ppb Level Based on Thionin-Functionalized Layered MoS2 Electrochemical Sensors. *Analytical Chemistry* **2014**, *86* (24), 12064–12069.

(16) Zhang, Y.; Feng, D.; Xu, Y.; Yin, Z.; Dou, W.; Habiba, U. E.; Pan, C.; Zhang, Z.; Mou, H.; Deng, H.; Mi, X.; Dai, N. DNA-Based Functionalization of Two-Dimensional MoS2 FET Biosensor for Ultrasensitive Detection of PSA. *Applied Surface Science* **2021**, *548*, 149169.

(17) Wei, J.; Zhao, Z.; Lan, K.; Wang, Z.; Qin, G.; Chen, R. Highly Sensitive Detection of Multiple Proteins from Single Cells by MoS2-FET Biosensors. *Talanta* **2022**, *236* (August 2021), 122839.

(18) Yang, Y.; Zeng, B.; Li, Y.; Liang, H.; Yang, Y.; Yuan, Q. Construction of MoS2 Field Effect Transistor Sensor Array for the Detection of Bladder Cancer Biomarkers. *Science China Chemistry* **2020**, *63* (7), 997–1003.

(19) Hossain, M.; Sanaullah, M.; Yousuf, A. H. Bin; Es-Saki, A.; Chowdhury, M. H. Analytical Analysis of the Contact Resistance (Rc) of Metal-MoS2 Interface. *Midwest Symposium on Circuits and Systems* **2015**, *2015-Septe*, 1–4.

(20) Park, H.; Han, G.; Lee, S. W.; Lee, H.; Jeong, S. H.; Naqi, M.; Almutairi, A.; Kim, Y. J.; Lee, J.; Kim, W. J.; Kim, S.; Yoon, Y.; Yoo, G. Label-Free and Recalibrated

Multilayer MoS2 Biosensor for Point-of-Care Diagnostics. *ACS Applied Materials and Interfaces* **2017**, *9* (50), 43490–43497.

(21) Naylor, C. H.; Kybert, N. J.; Schneier, C.; Xi, J.; Romero, G.; Saven, J. G.; Liu, R.; Johnson, A. T. C. Scalable Production of Molybdenum Disulfide Based Biosensors. *ACS Nano* **2016**, *10* (6), 6173–6179.

(22) Kufer, D.; Konstantatos, G. Photo-FETs: Phototransistors Enabled by 2D and 0D Nanomaterials. *ACS photonics* **2016**, *3*, 2197–2210.

(23) Radisavljevic, B.; Radenovic, A.; Brivio, J.; Giacometti, V.; Kis, A. Single-Layer MoS2 Transistors. *Nature Nanotechnology* **2011**, *6* (3), 147–150.

(24) Kaushik, V.; Varandani, D.; Das, P.; Mehta, B. R. Layer Dependent Photoresponse Behavior of Chemical Vapor Deposition Synthesized MoS2 Films for Broadband Optical Sensing. *Journal of Physics D: Applied Physics* **2019**, *52* (47).

(25) Pham, T.; Li, G.; Bekyarova, E.; Itkis, M. E.; Mulchandani, A. MoS2-Based Optoelectronic Gas Sensor with Sub-Parts-per-Billion Limit of NO2 Gas Detection. *ACS Nano* **2019**, *13* (3), 3196–3205.

(26) Peng, M.; Zheng, X.; Shen, C.; He, Y.; Wei, H.; Qiu, P.; Song, Y.; Tian, F.; Li, Y.; Wei, S.; Wang, Z. Synergistic UV and Humidity Response of Flexible MoS2/Kapton Heterointerfaces via Photogenerated Charge Transfer. *Journal of Materials Chemistry C* **2021**, *9* (25), 7982–7990.

(27) Brooks, T.; Keevil, C. W. A Simple Artificial Urine for the Growth of Urinary Pathogens. *Letters in Applied Microbiology* **1997**, *24* (3), 203–206.

(28) Shi, Y.; Li, H.; Li, L. J. Recent Advances in Controlled Synthesis of Two-Dimensional Transition Metal Dichalcogenides via Vapour Deposition Techniques. *Chemical Society Reviews* **2015**, *44* (9), 2744–2756.

(29) Mouri, S.; Miyauchi, Y.; Matsuda, K. Tunable Photoluminescence of Monolayer MoS2 via Chemical Doping. *Nano Letters* **2013**, *13* (12), 5944–5948.

(30) Pham, T.; Chen, Y.; Lopez, J.; Yang, M.; Tran, T.; Mulchandani, A. Effect of Al2O3 Passive Layer on Stability and Doping of MoS2 Field-Effect Transistor (FET) Biosensors. *Biosensors* **2021**, *11* (514), 1–13.

(31) Song, P.; Ou, P.; Wang, Y.; Yuan, H.; Duan, S.; Chen, L.; Fu, H.; Song, J.; Liu, X. An Ultrasensitive FET Biosensor Based on Vertically Aligned MoS2 Nanolayers with Abundant Surface Active Sites. *Analytica Chimica Acta* **2023**, *1252*, 341036. https://doi.org/10.1016/j.aca.2023.341036.

(32) Gunda, N. S. K.; Singh, M.; Norman, L.; Kaur, K.; Mitra, S. K. Optimization and Characterization of Biomolecule Immobilization on Silicon Substrates Using (3-Aminopropyl)Triethoxysilane (APTES) and Glutaraldehyde Linker. *Applied Surface Science* **2014**, *305*, 522–530.

(33) Chu, C.-H.; Sarangadharan, I.; Regmi, A.; Chen, Y.-W.; Hsu, C.-P.; Chang, W.-H.; Lee, G.-Y.; Chyi, J.-I.; Chen, C.-C.; Shiesh, S.-C.; Lee, G.-B.; Wang, Y.-L. Beyond the Debye Length in High Ionic Strength Solution: Direct Protein Detection with Field-Effect Transistors (FETs) in Human Serum. *Scientific Reports* **2017**, *7* (1), 5256.

(34) Purwidyantri, A.; Domingues, T.; Borme, J.; Guerreiro, J. R.; Ipatov, A.; Abreu, C. M.; Martins, M.; Alpuim, P.; Prado, M. Influence of the Electrolyte Salt Concentration on DNA Detection with Graphene Transistors. *Biosensors* **2021**, *11* (1), 1–15.

(35) Saleh, R.; Barth, M.; Eberhardt, W.; Zimmermann, A. Bending Setups for Reliability Investigation of Flexible Electronics. *Micromachines* **2021**, *12* (1), 1–22.

Chapter 3

Two-Dimensional Layered Van Der Waals Nanomaterial-Bioreceptor Hybrid Optoelectronic Biosensor

3.1 Introduction

Two-dimensional (2D) nanomaterials have garnered growing interest for their unique electronic and optical properties in various applications.[1,2] In particular, single-layered and multilayered MoS_2 show a number of advantage, including but not limited to sensors,[3] transistors,[4] photonics and photodetectors,[5,6] energy storage,[7] and hydrogen evolution,[8,9] demonstrating their unusual versatility. 2D MoS_2 materials show considerable potential in biosensor technology due to their outstanding mechanical performance,[10] remarkable biocompatibility,[11] and they fulfill the requirements necessary for creating biosensors that are both highly sensitive and selective.[12,13] Some recent examples include their application as a biosensor for the detection of proteins such as streptavidin and SARS-CoV-2,[14,15] for the diagnosis of cancer biomarkers such as exosomes and prostate-specific antigens, for the identification of biomolecules including DNA and glucose,[16,17] and even for single-cell analysis.[18] While these reports show good sensitivity and low limits of target detection, these sensors experienced problems/limitations. The most significant limitation of MoS_2 sensors is their poor conductivity, leading to a very low current output due to the inherently high resistance of MoS_2 materials and substantial contact resistance in the devices. An ideal strategy to

solve this problem would involve the conjugation of MoS_2 nanostructures with low work function contacts to build up hybrid structures. Utilizing graphene as contacts in MoS_2 FETs offers a myriad of advantages over traditional metals such as Au and Ti. Foremost, the tunable work function of graphene enables a close match to MoS_2, facilitating an efficient charge injection and extraction at the MoS_2/graphene interface, minimizing energy barriers.[19] Graphene-MoS_2 contacts exhibit a lower Schottky barrier, which offers a pristine 2D to 2D interface at contacts with the MoS_2 channel and eliminating the van der Waals gap in the case of metal S-D electrodes. This enhances carrier injection and collection for improved device performance[20]. Furthermore, owing to its high electrical conductivity, mechanical flexibility, chemical stability, and biocompatibility, graphene demonstrates distinct advantages for the development of flexible and robust electronics, particularly in biosensor applications that involve interfaces with biological entities.

The optoelectronic properties of MoS_2 add another layer of significance to its ability. Illumination can induce changes in the material's conductivity or generate photocurrents, enhancing the sensitivity and selectivity of the biosensor. Because Van Hove singularities in MoS_2 happen to be situated near the conduction and valence band edges, this allows it to excite a photon with energy nearly equivalent to its bandgap (which happens to be in the visible spectrum or red color) into an electron–hole

pair.[20,21] The absorption of this photon leads to the generation of additional free carriers, which in turn decreases the resistance of MoS_2 channel/gate in an FET.[22] Therefore, exciting the MoS_2 channel/gate of an FET by a low energy red color light during sensing will increase the current output and thereby improve the biosensor performance. Moreover, graphene is optically transparent, enabling the transmission of light through the electrode and facilitating the utilization of light in conjunction with MoS_2. The integration of these properties, with graphene serving as the electrode material for MoS_2-based optoelectronic biosensors, ensures a harmonious blend of electrical and optical functionalities. This hybrid application of the unique electrical and optical characteristics of MoS_2 and graphene establishes a robust heterostructure for advanced optoelectronic biosensing applications.

In this study, we designed an all 2D layered van der Waals nanomaterial-bioreceptor hybrid optoelectronic biosensor for the highly sensitive and selective detection of chemical/biological molecules. The optoelectronic device will be a photogated FET transducer with 2D chemical vapor deposition (CVD) grown MoS_2 semiconductor as a channel, CVD grown graphene as S-D electrodes and utilizing a red light-emitting diode (LED) as a photon source, with its photon energy aligned with the band gap of single-layer MoS_2, effectively reducing the channel resistance of the MoS_2.The nanostructured MoS_2-based FET channel is further modified with a

biological recognition element to enable the sensitive and selective detection of the chemical/biological target analyte, with the sensing of HIgG and anti-HIgG used as a model system for this research. First, we explored the device capability and biosensing capability of the optoelectronic biosensors platform with MoS_2 as the channel and graphene as the electrodes (Gr-MoS_2-Gr) on transparent and flexible Kapton substrate electronic performance and light dependency performance. We introduced a reliable passivation strategy, where a MoS_2-based device was coated by a layer of aluminum oxide (Al_2O_3) deposited via atomic layer deposition (ALD). Then the resistor biofunctionalized with (3-Aminopropyl) triethoxysilane (APTES) and glutaraldehyde, followed by antibody immbolization was demonstrated for the real-time detection of HIgG in liquid-phase. Second, we tested the biosensing capability of Gr-MoS_2-Gr with light and without light, and both conditions consistently upheld their performance without significant degradation, even in a simulated real urine sample test. The theoretical limit of detection (LOD) of the Gr-MoS_2-Gr -based biosensor for detection of HIgG was determined to be 6.22 ng/mL for sensing with illumination and 23.4 ng/mL for sensing without illumination. Furthermore, we examined in detail the biosensing response of a device which has CVD MoS_2 linked to interdigitated metal electrodes for detecting HIgG. Compared to MoS_2-based biosensors with metal contacts, the Gr-MoS_2-Gr configuration showed improvements in both sensitivity and the LOD. The 2D

hybrid optoelectronic biosensor offers a simple approach to a crucial sensing element in wearable electronic devices.

3.2 Materials and Methods

3.2.1 Chemicals and materials

1-mil Kapton films with a thickness of 25 μm were purchased from Cole-Parmer. The silicon wafer used had a 300 nm thermally grown oxide layer and was obtained from Ultrasil. Necessary materials such as sulfur, molybdenum trioxide (MoO_3), APTES, and glutaraldehyde solution (Grade II, 25% in water) were sourced from Sigma-Aldrich. Monoclonal anti-HIgG antibody, HIgG protein, human serum albumin (HSA), and bovine serum albumin (BSA) were acquired from Sigma-Aldrich. The water employed in the sensing experiments underwent purification through a Milli-Q system. Unless otherwise stated, all reagents were obtained from Fisher Scientific.

3.2.2 Instruments

MoS_2 was synthesized in a Lindberg/Blue tube furnace from Thermo Scientific. Photolithographic patterning was conducted using a Karl Suss MicroTech mask aligner (Model MA6, SÜSS MicroTec SE), followed by the application of metal contact pads via an e-beam evaporator (Temescal BJD-1800). For depositing Al_2O_3 layers, the Cambridge Nanotech Savannah 100 from Veeco Instruments was utilized. A red LED (UMLIFE US) with wavelength of 650 nm and output power of 5 mW was integrated with the biosensing microfluidics system. Electrical characteristics were measured using a

Keithley source meter, specifically the Model 2636. Raman spectra were captured using a Horiba LabRam system with a 532 nm green laser. Optical microscope (OM) images were taken with a Nikon L150 Optical Microscope.

3.2.3 Device fabrication

MoS_2 growth. CVD-grown MoS_2 was synthesized using the methodology we detailed in a previous publication.[13] MoS_2 was grown with sulfur and MoO_3 powders as precursors with a ratio of 10:1. The process involved heating a Si/SiO_2 substrate, positioned above MoO_3 powder, from room temperature to 725 °C, while introducing sulfur via evaporation at 170 °C. This temperature was consistently maintained for a 20-minute growth period of MoS_2. After unloading the sample from the tube furnace, MoS_2 on Si/SiO_2 substrate was spin-coated with polystyrene (PS) and the PS/MoS_2 films were delaminated in 1M KOH solution. The MoS_2/PS films were then washed thoroughly with deionized water to remove residues for further use.

Graphene growth. The process of growing single-layer graphene on copper also used CVD. A clean copper foil underwent annealing at a temperature of 1030 °C for 2 hours under a protective atmosphere with argon and hydrogen (375 sccm and 15 sccm). The diluted methane as carbon-containing precursor was introduced into the chamber, where it decomposed on the copper surface. The carbon atoms arrange themselves into a graphene lattice structure during the 40 min growth period. Afterwards, the sample

was gradually cooled to minimize defects. Poly(methyl methacrylate) (PMMA) film was coated on top to protect graphene and delaminated in 0.2 M ammonium persulfate solution. Following this, the graphene/PMMA films were repeatedly rinsed with deionized water to eliminate any residual substances and transferred onto a desired substrate.

Gr-MoS_2-Gr device. The schematic representation detailing the fabrication steps of the Gr-MoS_2-Gr device was illustrated in Figure 3.1a. After graphene was transferred to the Si/SiO_2 substrate (step A), graphene electrodes were constructed directly on the Si/SiO_2 substrate through conventional photolithography methods. Unwanted graphene areas were eliminated using N_2O plasma etching (step B). A piece of floating MoS_2/PS was transferred onto the patterned graphene electrodes substrate. After PS removal in toluene solution (step C), Raman spectroscopy was obtained to confirm its high quality and maintaining the properties post-transfer and during the electrodes patterning process. The insert optical images (Figure 3.1c) showcased a pair of patterned graphene electrodes separated with a width of 10 μm and MoS_2 on top as a channel. Raman spectroscopy of the Gr-MoS_2-Gr in Figure 3.1b confirmed its high quality and maintaining the properties post-transfer of MoS_2 and graphene. For the graphene electrodes area, both Line C and Line A in Figure 3.1b displayed a pronounced G peak at 1590 cm^{-1} and 2D peak at 2680 cm^{-1}. The MoS_2 channel area (Line B in Figure

3.1b) clearly indicates the E^1_{2g} peak at 385 cm^{-1} and A_{1g} peak at 402.6 cm^{-1}. In the overlapping region of the MoS_2 channel (Line C in Figure 3.1b), two distinct peaks are clearly observed, indicating the E^1_{2g} peak at 384 cm^{-1} and A_{1g} peak at 402.6 cm^{-1}. Through the application of Raman spectroscopy, we verified the MoS_2 layer to be either a monolayer or a double layer. Additionally, the low intensity of the graphene D band confirms the presence of a low density of defects within the graphene.[23–25] Then a new layer of PS was spin-coated on top of Gr-MoS_2-Gr on Si/SiO_2 substrate for wet transfer (step D). The Gr-MoS_2-Gr/PS film was lifted off in 1M KOH solution and was extensively washed with DI water to ensure residue removal (step E). Small areas of metal Cr/Au (5 nm/50 nm) were established as extended contacts and markers when using electron-beam metal deposition on flexible Kapton substrate (step F). Then Gr-MoS_2-Gr/PS film was transferred onto prepatterned Kapton substrate (step G). The PS film was removed in toluene. Subsequently, a 30 nm thick Al_2O_3 layer was deposited at 250 °C using water and trimethylaluminum as precursors. This process was carried out for 300 cycles in an ALD system (step H). The Al_2O_3 passivated devices were used for further functionalization and detections (step I).

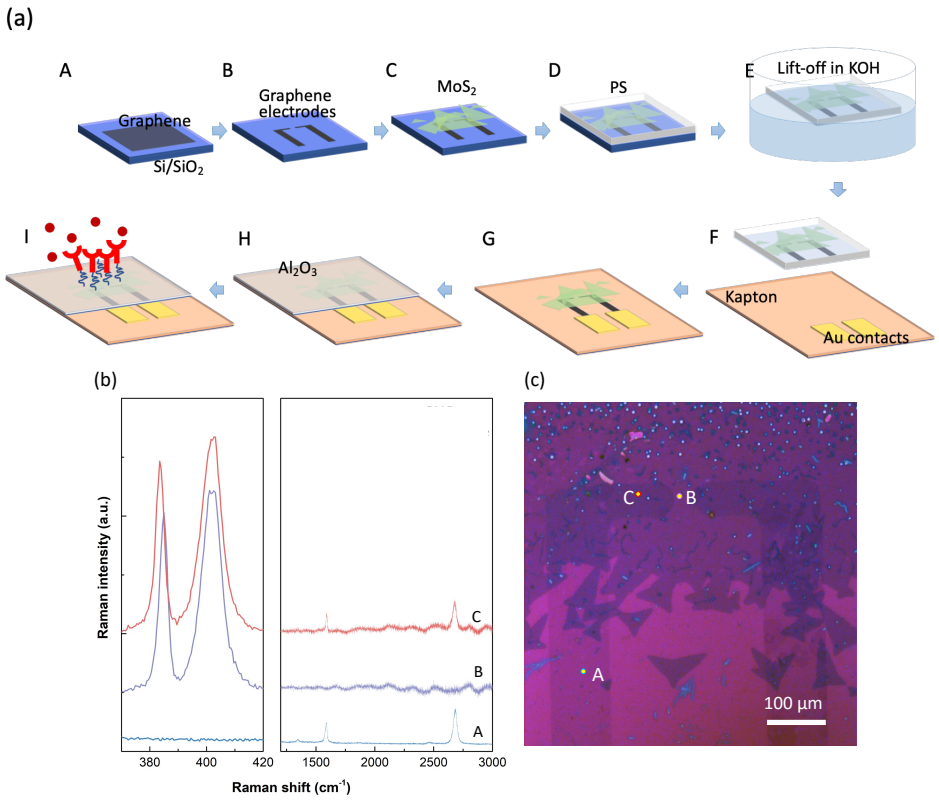

Figure 3.1. (a) The graphical depiction illustrates the fabrication process of Gr-MoS_2-Gr device. (b) Raman spectra of Gr-MoS_2-Gr at different areas. (c) Gr-MoS_2-Gr optical images on Si/SiO_2 substrate.

Au-MoS_2-Au device. A Cr/Au layer was deposited onto the Kapton substrate serving as the source and drain terminals, featuring a 10 µm × 10 µm gap and 5 nm/50 nm thick. Following this, the MoS_2/PS films were transferred onto the pre-prepared Kapton chips. The dissolution of PS was accomplished by immersing the samples in a toluene solution at room temperature. After that, a 30 nm thickness of the Al_2O_3 layer was grown at 250 °C. The Al_2O_3 passivated devices were used for further functionalization and detections.

3.2.4 Functionalization

The Al_2O_3 passivated devices were treated with ammonium hydroxide (NH_4OH) for 30 min. Following that, the device was immersed in APTES for an hour and then underwent a thorough ethanol wash. Subsequently, it was incubated in 25% glutaraldehyde for two hours and then rinsed with a 10 mM phosphate buffer (PB). Next, the device was incubated with 50 μg/mL anti-HIgG in PB overnight at 4 ^{o}C to immobilize the antibody and quenched with 10 wt.% ethanolamine. The above steps were done at room temperature except the anti-HIgG immobilization step.

3.2.5 Electrical characterization

Transfer characteristic curves using electrolyte-gating were measured at $V_D = 1$ with Ag/AgCl electrode and in 10 mM phosphate buffer electrolyte. The output characteristic curves were gathered at zero gate voltage ($V_G = 0$ V) by using a low-power mode.

3.2.6 Biosensing of HIgG

The biofunctionalized device was applied to detect HIgG antigens with different concentrations in PB solution. These experiments were conducted in a home-made microfluidic system. A customized PMMA cell with a volume of 30 μL was utilized for the detection process. The red LED light was introduced to the system from the bottom of the customized PMMA cell. With and without illumination, a range of different concentrations of HIgG were conducted to determine analytical figures of merits of

dynamic range, sensitivity, and LOD. During each run, the solutions were introduced into the biosensor, while the real-time change in electrical resistance was continuously monitored. This monitoring took place under an applied V_D of 1 V, with no gate voltage applied.

To test the suitability of the constructed MoS_2-based flexible optoelectronic biosensor for HIgG detection in a physiological environment, the biosensor was further tested in human body fluids with a red-light illumination from the bottom. An artificial urine (AU) matrix (pH = 7.4) was applied to simulate a real-life complex sensing environment.[26]

To assess the specificity of the developed sensing platform for HIgG detection, proteins such as BSA and HSA were chosen as control groups. These proteins were individually introduced into the protein detection system described above, replacing HIgG in the same detection process.

3.3 Results and Discussion

3.3.1 Electrical characterizations of Gr-MoS_2-Gr FET

The electrical characterizations of Gr-MoS_2-Gr FET biosensor were conducted at ambient conditions. The output characteristic was shown in Figure 3.2, where drain voltage (V_D) varies from -1 to 1 V, and no gate voltage was applied. The I-V curves show a very high current corresponding to the lower device resistance of ~460 kΩ. Compared with the Au-MoS_2-Au device, which shows a very high resistance of ~200

GΩ, the resistance was lower, which was due to the 2D to 2D interface at contact with MoS_2 channel that eliminated the van der Waals gap in the case of metal S-D electrodes.[20] To protect the surface, the devices passivated with Al_2O_3. The I-V curves shown demonstrate a linear relationship between current and applied bias. The increased current compared with pristine is attributed to the strong n-doping effect facilitated by the aluminum oxide layer, necessitating lower source-drain bias while still increasing current and charge mobility. Additionally, the presence of the oxide layer makes the device's surface suitable for biofunctionalization.[13]

Incorporating red LED light illumination in MoS_2 FET is pivotal for exploiting the optoelectronics behavior of MoS_2 semiconductors. The selected 650 nm red LED light's energy aligns with the bandgap of MoS_2, ensuring efficient excitation. This deliberate exposure excites electrons across the bandgap of MoS_2, generating electron-hole pairs and inducing a photocurrent in the MoS_2 channel. The I-V curve of Al_2O_3 passivated Gr-MoS_2-Gr showed the improved output characteristic of the optoelectronic transduction device in air when the light was introduced from the bottom. In the light state, there was a noticeable increase in current, accompanied by enhanced photocurrent to three times level. The red-light illumination induced a rapid increase in photocurrent as photogenerated electron-hole pairs contribute to an increased electron concentration in the conduction band. Consequently, the magnitude

of current in such a device was directly associated with electron concentration in MoS_2, which, in turn led to a surge in current in the device. This photocurrent response will enhance sensitivity and improves the signal-to-noise ratio, contributing to a more reliable sensing platform.[20]

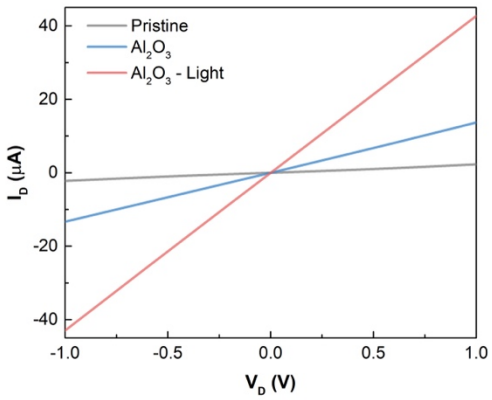

Figure 3.2. Output characteristics of pristine Gr-MoS_2-Gr and Al_2O_3 passivated Gr-MoS_2-Gr in dark, and Al_2O_3 passivated Gr-MoS_2-Gr with red light illumination. The Output characteristic of Al_2O_3 passivated Gr-MoS_2-Gr device was measured at V_D = 1V with red LED light from bottom.

3.3.2 Efficient capture and selective detection of HIgG

The importance of linkers is that they provide a chemical bridge between the sensor surface and the biomolecules (such as proteins or antibodies) to be immobilized. APTES and glutaraldehyde modifications play a vital role in creating a chemically suitable and stable environment for the covalent attachment of proteins, enhancing the reliability and functionality of the biosensor in many applications.[27–29] Herein, APTES and glutaraldehyde were used to modify the surface to immobilize covalent protein for

immunoassay with the biosensor. The surface was first treated with ammonium hydroxide to clean the surface and obtain a rougher surface. The anti-HIgG was covalently immobilized on the APTES-glutaraldehyde surface through the formation of imine bonds, where the aldehyde group on the surface chemically bonded with the primary amine group presented on the anti-HIgG.[30] To evaluate the bonding changes of the surface, output characteristics were used for the functionalization process without red light illumination. I-V curves were linear in V_D range of -1 to 1 V, which suggested that the electrode-channel contact is ohmic (Figure 3.3a). Compared with a Al_2O_3 passivated surface, the treatment of ammonium hydroxide (NH_4OH) resulted in a decrease in current. After antibody immobilized on the device surface via linkers, we observed a decrease in the slope of the I-V measurements from the bare Al_2O_3 passivated device. The addition of biomolecules to the linkers in subsequent steps consistently led to more pronounced changes in the slopes of the I-V curves. This effect was primarily attributed to the considerably larger size of protein molecules, which resulted in an increase in device resistance.

FET transfer curves were used in biosensing performance evaluations. Transfer characteristic curves using electrolyte-gating measured at V_D = 1 V by top-gating with Ag/AgCl electrode and in 10 mM phosphate buffer electrolyte without LED light illumination. When a biological molecule binds to the surface of an FET, it changes the

local charge environment. This change affects the current flowing through the transistor, which is readily measurable. When HIgG molecules were introduced onto the functionalized channel, they bonded to these antibodies, resulting in a noticeable decrease in the current as observed in the transfer curves (Figure 3.3b). As the concentration of bound HIgG molecules increased, they increasingly impacted the electrical properties of the MoS_2 FET, led to a reduction in current that corresponds with the rising concentration.

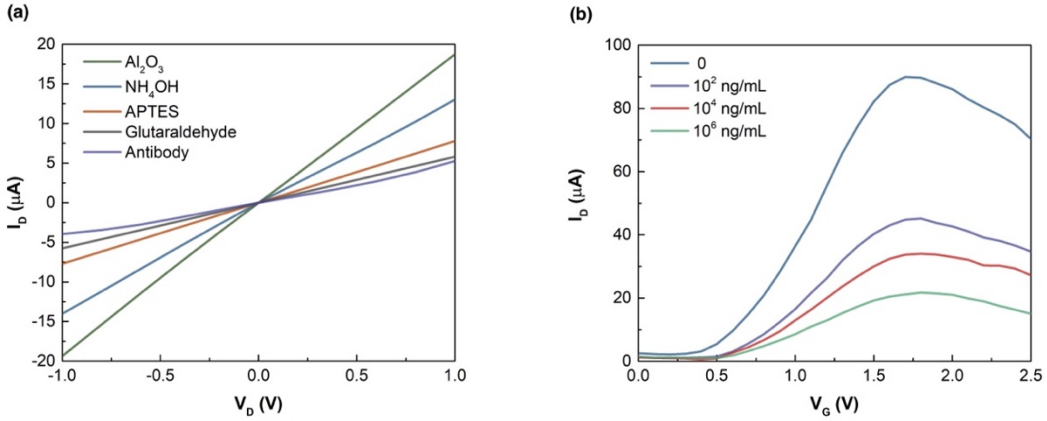

Figure 3.3. Electrical characterizations of Gr-MoS_2-Gr FET device. (a) Representative output measurements of the device during functionalization steps (no gate voltage applied). (b) Representative transfer curves (V_D = 1V) in response to liquid samples spiked with HIgG antigen at increased concentrations: 10^2, 10^4, 10^6 ng/mL.

3.3.3 Real-time resistance monitoring of Gr-MoS_2-Gr

Changes in the electrical properties of the Gr-MoS_2-Gr FET as biomolecules bind to its surface can be continuously monitored, providing dynamic information about the binding process. The biofunctionalized devices were conducted in a homemade microfluidic system with red LED light enhancement. Figure 3.4a showed

the time-dependent change in resistance. It was evident that the initial spike in the readings was attributable to the physical injection of each analyte. However, the subsequent increase in the readings, observed after stabilization, was indeed a result of the increasing amounts of HIgG. Noticeably compared without illumination, the response to HIgG analyte solution under illumination was enhanced dramatically. Calibration curves, plotted in Figure 3.4b, demonstrated a linear relationship between the concentration of HIgG and the change in resistance, covering a broad range of HIgG concentrations from 10 to 10^6 ng/mL. It presented the amplitude of relative response $\Delta R/R_0$ when red light was introduced to the system compared to the responses without light illumination. Under red light illumination, a high sensitivity of 0.1178 per Log[ng/mL] was observed, 1.88 times as high of sensitivity without illumination of 0.0628 per Log[ng/mL]. To calculate the theoretical LOD, we followed the same method described in our previous work.[31] The root-mean-square values of the sensing process with and without illumination were 0.0312 and 0.0287. The LOD was estimated to be 6.22 ng/mL and 23.4 ng/mL for the sensing process with and without red light illumination, respectively. The evident improvement in LOD was indicative of the high sensitivity of the photogate enhanced Gr-MoS_2-Gr FET optoelectronic biosensor. Furthermore, the minimal error bars evident in the results indicates a high level of reproducibility, thereby ensuring consistent and reliable detection of HIgG.

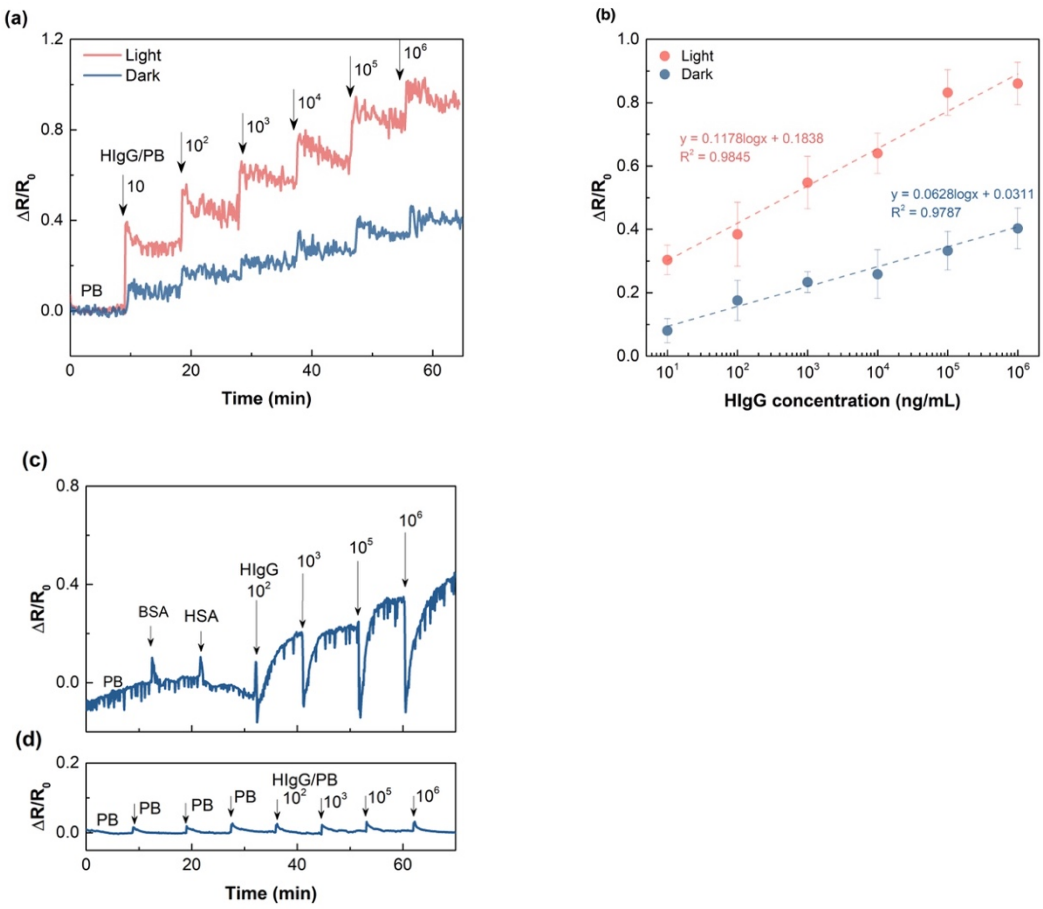

Figure 3.4. (a) Real-time observation of resistance changes during the HIgG sensing and priming process. This monitoring is performed under conditions of both illumination and non-illumination, with V_D = 1 V. (b) Calibration curve of Gr-MoS_2-Gr biosensor with and without illumination. (c) Real-time tracking of resistance variations with different biomolecules solutions additions, which are measured with red light illumination from bottom. (d) Real-time tracking of resistance variations for control experiments with red light illumination from bottom, showed a negative control sensing process not functionalized with anti-HIgG device.

To affirm that the observed results stem from the specific antibody-antigen interaction, control experiments were performed. First, after additions of high concentrations of BSA and HSA (10^3 ng/mL), which were not specific for anti-HIgG, the conductance of the biofunctionalized sensor did not show any response. In contrast,

subsequent, addition of HIgG solutions produced a conductance drop, as observed in Figure 3.4c. This was indicative of the specificity of our biosensors for HIgG biomarkers. Second, unmodified MoS_2-based devices, which was modified with linkers but not immobilized with anti-HIgG, did not exhibit conductance changes after adding PB solutions and different concentrations of HIgG solutions (Figure 3.4d). These results showed the good specificity of Gr-MoS_2-Gr biosensors for practical applications.

3.3.4 HIgG detection in physiological solutions

It's crucial to ascertain that the biosensor can accurately detect the target molecule amidst various other substances present in complex medium. To evaluate the sensitivity and specificity of the constructed MoS_2-based flexible optoelectronic biosensor, tests in a medium that closely resembles the reality use case were conducted for the real-time detections with light. We utilized AU matrix with a pH of 7.4 for simulating real-life sensing scenarios.[26] In Figure 3.5a, it was evident that the addition of AU led to a marked reduction in response. This decrease was due to the high ionic strength and elevated salinity inherent in the AU matrix. In the highly saline solutions, ions accumulated at the interface and formed a high capacitance region because of electrical double layer formed at the interface between solid and liquid.[32] It led to higher density of the ions accumulated on the passivated surface and increase in the electron concentration. Thus, the drain current increased and resistance decreased.[33] It

was decided to perform a washing procedure with PB solution. This step was essential to restore the responses of the MoS_2-based biosensor. After thoroughly washing by PB solution and removing the salts out of the test cell, a local environment was in low ionic strength. Therefore, the affinity binding of antigen-antibody interactions was not affected by the highly saline solutions any more. The responses were recovered and showed excellent agreement with the responses in PB as shown in Figure 3.5a. It indicated the washing process was necessary to remove the salts and the effects were minimal after thoroughly washed with PB solution. The calibration curve was shown in Figure 3.5b, which offers linear regression between HIgG concentration and the changes in resistance. The results also demonstrated a similarly high sensitivity of 0.1299 per Log[ng/mL], comparable to the sensitivity observed in a simple matrix of 10 mM PB, which showed a sensitivity of 0.1259 per Log[ng/mL] within the HIgG range of 10-10^5 ng/mL. The ability of the Gr-MoS_2-Gr biosensor to detect HIgG with remarkable sensitivity, even amidst salts and other biological components, makes it a promising candidate for real-world applications. The results emphasize real-time monitoring and testing of the biosensor in simulated urine conditions, showcasing its stability and resilience in complex environments, and making it suitable for health monitoring and medical diagnostics involving human urine and potantially other body fluid samples.

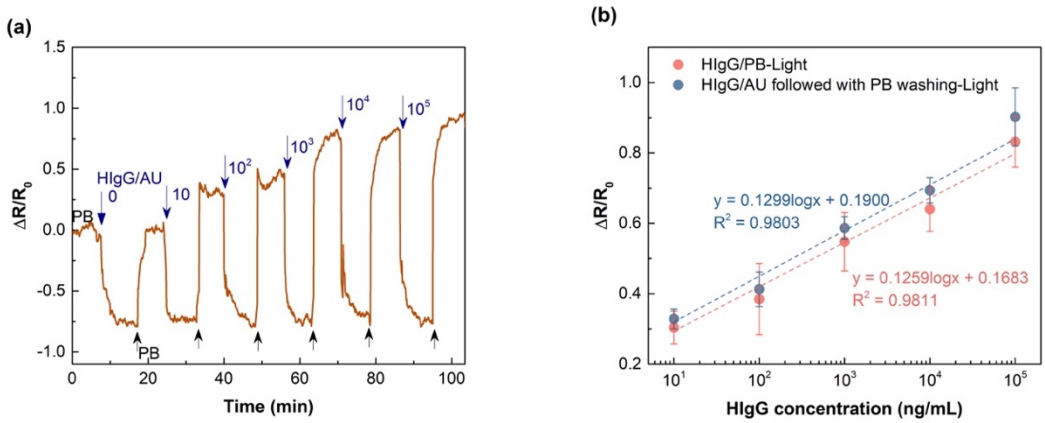

Figure 3.5. (a) Real-time observation of resistance changes during the HIgG sensing in AU with 10 mM PB wash (V_D = 1 V). (b) Calibration curves of Al_2O_3 passivated Gr-MoS_2-Gr biosensors detections with light in simple matrix of 10 mM PB and in complex matrix of AU with 10 mM PB wash.

3.3.5 Comparison of Au-MoS_2-Au and Gr-MoS_2-Gr biosensors

In addition to the Gr-MoS_2-Gr hybrid biosensor, the Au-MoS_2-Au biosensor was evaluated for HIgG detection. Figure 3.6 presented a comparison of the performance of both biosensors. They each showed a high response in terms of resistance change when detecting HIgG in a simple matrix. Notably, the Gr-MoS_2-Gr biosensor demonstrated greater resistance changes compared to the Au-MoS_2-Au biosensor when subjected to red light illumination at all three tested HIgG concentrations. These results highlight the Gr-MoS_2-Gr biosensor's enhanced detection capabilities and sensitivity, suggesting its potential for superior performance in biosensing applications.

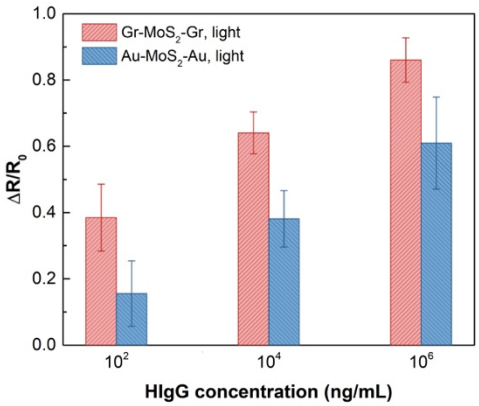

Figure 3.6. Calibration curves of Al_2O_3 passivated Gr-MoS_2-Gr and Au-MoS_2-Au biosensors in PB matrix with red LED light illumination.

3.4 Conclusions

The strategic choice of graphene as contacts in MoS_2 FETs, combining electrical, mechanical, and chemical properties with biocompatibility, forms a robust platform Gr-MoS_2-Gr hybrid optoelectronics for biosensing applications. The enhancement of photocurrent under red LED light increases current by three times and boosts sensitivity, enabling real-time detection with fast response and high selectivity. The flexibility of devices with both electrical- and photo-gated options presents promising applications for point-of-care medical settings. Utilizing graphene electrodes holds great potential to minimize contact resistance in biosensors, creating 2D to 2D contacts with the MoS_2 channel for flexible substrate-based photogated FET biosensors. The incorporation of red LED light, exploiting the unique optical properties of MoS_2, transforms it into a heterostructure-based optoelectronic biosensor. This design

significantly improves current output, resulting in a high sensitivity of 0.1178 per Log[ng/mL] under red light illumination, compared to 0.0628 per Log[ng/mL] without illumination. The estimated LOD of 6.22 and 23.4 ng/mL for sensing with and without illumination, respectively. The results also demonstrate a similarly high sensitivity of 0.1299 per Log[ng/mL] in complex AU matrix after PB wash. The MoS_2-based flexible optoelectronic biosensor demonstrates high sensitivity, instant detection feedback, and specificity for HIgG. This approach renders it a viable option for the economical detection of a wide range of biomolecules and biomarkers and highlights the potential for early disease diagnostics. This study presents a breakthrough in the development of advanced biosensing platforms. This biosensor design contributes to the ongoing evolution of sensing technologies but also opens avenues for innovations with far-reaching implications in healthcare, diagnostics, and beyond.

3.5 References

(1) Jing, Y.; Liu, B.; Zhu, X.; Ouyang, F.; Sun, J.; Zhou, Y. Tunable Electronic Structure of Two-Dimensional Transition Metal Chalcogenides for Optoelectronic Applications. *Nanophotonics* **2020**, *9* (7), 1675–1694. https://doi.org/10.1515/nanoph-2019-0574.

(2) Meng, Z.; Stolz, R. M.; Mendecki, L.; Mirica, K. A. Electrically-Transduced Chemical Sensors Based on Two-Dimensional Nanomaterials. *Chem. Rev.* **2019**, *119* (1), 478–598. https://doi.org/10.1021/acs.chemrev.8b00311.

(3) Samy, O.; Zeng, S.; Birowosuto, M. D.; El Moutaouakil, A. A Review on MoS2 Properties, Synthesis, Sensing Applications and Challenges. *Crystals* **2021**, *11* (4), 355. https://doi.org/10.3390/cryst11040355.

(4) Radisavljevic, B.; Radenovic, A.; Brivio, J.; Giacometti, V.; Kis, A. Single-Layer MoS2 Transistors. *Nature Nanotech* **2011**, *6* (3), 147–150. https://doi.org/10.1038/nnano.2010.279.

(5) Gant, P.; Huang, P.; Pérez De Lara, D.; Guo, D.; Frisenda, R.; Castellanos-Gomez, A. A Strain Tunable Single-Layer MoS2 Photodetector. *Materials Today* **2019**, *27*, 8–13. https://doi.org/10.1016/j.mattod.2019.04.019.

(6) Yang, X.; Li, B. Monolayer MoS $_2$ for Nanoscale Photonics. *Nanophotonics* **2020**, *9* (7), 1557–1577. https://doi.org/10.1515/nanoph-2019-0533.

(7) Li, X. L.; Li, T. C.; Huang, S.; Zhang, J.; Pam, M. E.; Yang, H. Y. Controllable Synthesis of Two-Dimensional Molybdenum Disulfide (MoS2 for Energy-Storage Applications. *ChemSusChem* **2020**, *13* (6), 1379–1391. https://doi.org/10.1002/cssc.201902706.

(8) Wang, H.; Xiao, X.; Liu, S.; Chiang, C.-L.; Kuai, X.; Peng, C.-K.; Lin, Y.-C.; Meng, X.; Zhao, J.; Choi, J.; Lin, Y.-G.; Lee, J.-M.; Gao, L. Structural and Electronic Optimization of MoS $_2$ Edges for Hydrogen Evolution. *J. Am. Chem. Soc.* **2019**, *141* (46), 18578–18584. https://doi.org/10.1021/jacs.9b09932.

(9) Cao, Y. Roadmap and Direction toward High-Performance MoS $_2$ Hydrogen Evolution Catalysts. *ACS Nano* **2021**, *15* (7), 11014–11039. https://doi.org/10.1021/acsnano.1c01879.

(10) Jiang, J.-W.; Park, H. S. Mechanical Properties of MoS2/Graphene Heterostructures. *Applied Physics Letters* **2014**, *105* (3), 033108. https://doi.org/10.1063/1.4891342.

(11) Zhang, Y.; Li, X.; Li, D.; Wei, Q. A Laccase Based Biosensor on AuNPs-MoS2 Modified Glassy Carbon Electrode for Catechol Detection. *Colloids and Surfaces B: Biointerfaces* **2020**, *186*, 110683. https://doi.org/10.1016/j.colsurfb.2019.110683.

(12) Zhang, Y.; Feng, D.; Xu, Y.; Yin, Z.; Dou, W.; Habiba, U. E.; Pan, C.; Zhang, Z.; Mou, H.; Deng, H.; Mi, X.; Dai, N. DNA-Based Functionalization of Two-Dimensional MoS2 FET Biosensor for Ultrasensitive Detection of PSA. *Applied Surface Science* **2021**, *548*, 149169. https://doi.org/10.1016/j.apsusc.2021.149169.

(13) Pham, T.; Chen, Y.; Lopez, J.; Yang, M.; Tran, T.-T.; Mulchandani, A. Effect of Al2O3 Passive Layer on Stability and Doping of MoS2 Field-Effect Transistor (FET) Biosensors. *Biosensors* **2021**, *11* (12), 514. https://doi.org/10.3390/bios11120514.

(14) Wei, J.; Zhao, Z.; Luo, F.; Lan, K.; Chen, R.; Qin, G. Sensitive and Quantitative Detection of SARS-CoV-2 Antibodies from Vaccinated Serum by MoS_2 -Field Effect Transistor. *2D Mater.* **2022**, *9* (1), 015030. https://doi.org/10.1088/2053-1583/ac40c4.

(15) Noguchi, H.; Nakamura, Y.; Tezuka, S.; Seki, T.; Yatsu, K.; Narimatsu, T.; Nakata, Y.; Hayamizu, Y. Self-Assembled GA-Repeated Peptides as a Biomolecular Scaffold for Biosensing with MoS_2 Electrochemical Transistors. *ACS Appl. Mater. Interfaces* **2023**, acsami.2c23227. https://doi.org/10.1021/acsami.2c23227.

(16) Yoon, J.; Lee, S. N.; Shin, M. K.; Kim, H.-W.; Choi, H. K.; Lee, T.; Choi, J.-W. Flexible Electrochemical Glucose Biosensor Based on GOx/Gold/MoS2/Gold Nanofilm on the Polymer Electrode. *Biosensors and Bioelectronics* **2019**, *140*, 111343. https://doi.org/10.1016/j.bios.2019.111343.

(17) Liu, J.; Chen, X.; Wang, Q.; Xiao, M.; Zhong, D.; Sun, W.; Zhang, G.; Zhang, Z. Ultrasensitive Monolayer MoS_2 Field-Effect Transistor Based DNA Sensors for Screening of Down Syndrome. *Nano Lett.* **2019**, *19* (3), 1437–1444. https://doi.org/10.1021/acs.nanolett.8b03818.

(18) Wei, J.; Zhao, Z.; Lan, K.; Wang, Z.; Qin, G.; Chen, R. Highly Sensitive Detection of Multiple Proteins from Single Cells by MoS2-FET Biosensors. *Talanta* **2022**, *236*, 122839. https://doi.org/10.1016/j.talanta.2021.122839.

(19) Yu, Y.-J.; Zhao, Y.; Ryu, S.; Brus, L. E.; Kim, K. S.; Kim, P. Tuning the Graphene Work Function by Electric Field Effect. *Nano Lett.* **2009**, *9* (10), 3430–3434. https://doi.org/10.1021/nl901572a.

(20) Pham, T.; Li, G.; Bekyarova, E.; Itkis, M. E.; Mulchandani, A. MoS_2 -Based Optoelectronic Gas Sensor with Sub-Parts-per-Billion Limit of NO_2 Gas Detection. *ACS Nano* **2019**, *13* (3), 3196–3205. https://doi.org/10.1021/acsnano.8b08778.

(21) Hu, J.-Q.; Shi, X.-H.; Wu, S.-Q.; Ho, K.-M.; Zhu, Z.-Z. Dependence of Electronic and Optical Properties of MoS2 Multilayers on the Interlayer Coupling and Van Hove Singularity. *Nanoscale Res Lett* **2019**, *14* (1), 288. https://doi.org/10.1186/s11671-019-3105-9.

(22) Buscema, M.; Island, J. O.; Groenendijk, D. J.; Blanter, S. I.; Steele, G. A.; Van Der Zant, H. S. J.; Castellanos-Gomez, A. Photocurrent Generation with Two-Dimensional van Der Waals Semiconductors. *Chem. Soc. Rev.* **2015**, *44* (11), 3691–3718. https://doi.org/10.1039/C5CS00106D.

(23) Plechinger, G.; Heydrich, S.; Eroms, J.; Weiss, D.; Schüller, C.; Korn, T. Raman Spectroscopy of the Interlayer Shear Mode in Few-Layer MoS2 Flakes. *Applied Physics Letters* **2012**, *101* (10), 101906. https://doi.org/10.1063/1.4751266.

(24) Lee, C.; Yan, H.; Brus, L. E.; Heinz, T. F.; Hone, J.; Ryu, S. Anomalous Lattice Vibrations of Single- and Few-Layer MoS_2. *ACS Nano* **2010**, *4* (5), 2695–2700. https://doi.org/10.1021/nn1003937.

(25) Ferrari, A. C.; Basko, D. M. Raman Spectroscopy as a Versatile Tool for Studying the Properties of Graphene. *Nature Nanotech* **2013**, *8* (4), 235–246. https://doi.org/10.1038/nnano.2013.46.

(26) Brooks, T.; Keevil, C. W. A Simple Artificial Urine for the Growth of Urinary Pathogens. *Letters in Applied Microbiology* **1997**, *24* (3), 203–206.

(27) Sen, A.; Shim, J.; Bala, A.; Park, H.; Kim, S. Boosting Sensitivity and Reliability in Field-Effect Transistor-Based Biosensors with Nanoporous MoS_2 Encapsulated by Non-Planar Al_2O_3. *Adv Funct Materials* **2023**, *33* (42), 2301919. https://doi.org/10.1002/adfm.202301919.

(28) Wei, J.; Zhao, Z.; Luo, F.; Lan, K.; Chen, R.; Qin, G. Sensitive and Quantitative Detection of SARS-CoV-2 Antibodies from Vaccinated Serum by MoS_2 -Field

Effect Transistor. *2D Mater.* **2022**, *9* (1), 015030. https://doi.org/10.1088/2053-1583/ac40c4.

(29) Gunda, N. S. K.; Singh, M.; Norman, L.; Kaur, K.; Mitra, S. K. Optimization and Characterization of Biomolecule Immobilization on Silicon Substrates Using (3-Aminopropyl)Triethoxysilane (APTES) and Glutaraldehyde Linker. *Applied Surface Science* **2014**, *305*, 522–530. https://doi.org/10.1016/j.apsusc.2014.03.130.

(30) Zeng, Q.; Zhang, Y.; Song, K.; Kong, X.; Aalders, M. C. G.; Zhang, H. Enhancement of Sensitivity and Specificity of the Fluoroimmunoassay of Hepatitis B Virus Surface Antigen through "Flexible" Coupling between Quantum Dots and Antibody. *Talanta* **2009**, *80* (1), 307–312. https://doi.org/10.1016/j.talanta.2009.06.061.

(31) Pham, T.; Chen, Y.; Lopez, J.; Yang, M.; Tran, T.; Mulchandani, A. Effect of Al2O3 Passive Layer on Stability and Doping of MoS2 Field-Effect Transistor (FET) Biosensors. *Biosensors* **2021**, *11* (514), 1–13.

(32) Chu, C.-H.; Sarangadharan, I.; Regmi, A.; Chen, Y.-W.; Hsu, C.-P.; Chang, W.-H.; Lee, G.-Y.; Chyi, J.-I.; Chen, C.-C.; Shiesh, S.-C.; Lee, G.-B.; Wang, Y.-L. Beyond the Debye Length in High Ionic Strength Solution: Direct Protein Detection with Field-Effect Transistors (FETs) in Human Serum. *Scientific Reports* **2017**, *7* (1), 5256.

(33) Purwidyantri, A.; Domingues, T.; Borme, J.; Guerreiro, J. R.; Ipatov, A.; Abreu, C. M.; Martins, M.; Alpuim, P.; Prado, M. Influence of the Electrolyte Salt Concentration on DNA Detection with Graphene Transistors. *Biosensors* **2021**, *11* (1), 1–15.

Chapter 4

Biological Sensing Using Vertical MoS_2-Graphene Heterostructures Based Field-Effect Transistor Biosensors

4.1 Introduction

Two-dimensional (2D) heterostructures are increasingly attracting attention for their unique ability to combine and enhance the individual properties of different 2D materials, such as graphene, molybdenum disulfide (MoS_2), through stacking resulting in a new material system enabling the combination of distinct 2D materials with varied electronic, optical, and mechanical properties, allowing researchers to engineer new materials with tailored properties for advanced applications in electronics, optoelectronics, and biosensing.[1–3] In the landscape of 2D materials, graphene and MoS_2 each contribute their unique advantages, setting the stage for groundbreaking applications. Graphene is renowned for its unparalleled electrical conductivity and robust mechanical properties, yet its zero bandgap is a limitation for semiconducting uses.[4] MoS_2, with its significant bandgap and high on/off ratio, is well-suited for semiconducting applications but showed low conductivity and mechanical strength. Merging MoS_2 and graphene into a heterostructure harnesses the best of both worlds—graphene's efficient charge transfer and MoS_2's biosensing capabilities—effectively addressing their individual shortcomings with improved carrier mobility, sensitivity, and specificity for biomolecule detection and creating a synergistic platform for

advanced biosensor development. The vertical stacking in 2D MoS_2 and graphene heterostructures employs strong covalent bonds within planes and utilizes weaker Van der Waals forces between layers. This significantly broadens the potential applications of 2D materials by leveraging both the inherent properties of the individual layers and the novel features arising from their integration. Kim et al.'s study showcases the graphene/MoS_2 heterojunction platform's ability to significantly boost carrier mobility—up to ten times (~100 cm^2/Vs) more than that of monolayer MoS_2—while also maintaining a high on/off current ratio of about 10^8 at room temperature.[5] This heterostructure's advantages extend to adjustable Fermi levels via extensive back-gate bias, enabling the modulation of the Schottky barrier height, which in turn, facilitates improved carrier mobility. Pham et al.'s research underscores the significant potential of graphene-MoS_2 heterostructures in enhancing electronic devices, particularly for gas sensing applications.[6] The study specifically demonstrates advancements in transistor performance for detecting toluene, showcasing the heterostructures' ability to improve the sensitivity and selectivity of sensors. This breakthrough paves the way for the development of more effective environmental monitoring and safety devices. Ignatova et al. explore the potential of MoS_2-graphene heterostructures for label-free biosensing, targeting a widely used cancer medication.[7] Their comprehensive study reveals that lattice mismatches and variations in work function at the nanoscale significantly boost

biosensor efficiency through three distinct optical detection methods. The research highlights the pivotal role of these heterostructures in enhancing sensitivity and specificity for biomolecule detection, signifying a major leap in biosensing technology.

Additionally, heterostructures offer more possibilities and choices for the biofunctionalization of biosensors, enhancing their adaptability and effectiveness in detecting a wide range of biological targets. Since there are two ways to build up the heterostructure biosensors, capping MoS_2 on top of graphene functionalizes on MoS_2, or capping graphene on top of MoS_2 functionalizes on graphene. A variety of biofunctionalization techniques for MoS_2-based biosensors have been explored, encompassing strategies like utilizing Van der Waals forces, leveraging hydrophobic interactions, taking advantage of electrostatic attractions, and covalent through diazonium salts doping and thiol coordination.[8–13] Similarly, Hydroxylated aryl groups grafted and organic functional groups covalent approaches are widely applied for graphene functionalization.[14] Specially, non-covalent through π-systems essential for ensuring stability of functional nanomaterials and organic compounds is appealing as a production strategy owing to graphene unique nation stacking way.[14–17]

In this paper, we explore the application of MoS_2 and graphene vertical heterostructures in FET biosensors, focusing on the synthesis, functionalization, and characterization of these materials for biomolecule sensing. We explore how the

arrangement of MoS_2, and graphene layers affects their properties by alternating the stacking order of the two materials, to obtain MoS_2 on top of graphene (MG) and graphene on top of MoS_2 (GM) configurations, examining their electronic interactions, charge transfer dynamics, and implications for carrier mobility and biosensor performance. Functionalization techniques are tailored to each material's unique properties with two-step process; MoS_2 involved silane-based triethoxsilylbutyraldehyde (TESBA) deposition on the surface, followed by mobilization of antibody with the aldehyde of TESBA, while graphene was modified with self-assembled 1-pyrenebutyric acid N-hydroxysuccinimide ester (PBASE), followed by a reaction between the aldehyde of PBASE with antibody. By systematically studying the influence of material characteristics and device architecture on biosensing performance, the optimal configuration depends on the specific application's requirements, such as desired electronic characteristics, carrier mobility, or sensitivity. This work sheds light on the mechanisms underpinning biomolecule detection and offers insights into optimizing heterostructure-based FET biosensors for clinical and environmental applications.

4.2 Materials and methods

4.2.1 Material synthesis

MoS_2 was synthesized on a 300 nm thick SiO_2 substrate utilizing MoO_3 and sulfur as precursors in a chemical vapor deposition (CVD) chamber. The process was

conducted under an argon gas atmosphere to ensure controlled growth conditions. Graphene synthesis was carried out separately in a distinct CVD chamber. This process involved the use of a polycrystalline copper foil as the growth substrate, with hydrogen (10 sccm) and argon (300 sccm) gases creating the necessary chemical environment. A low concentration of methane (90 ppm) was introduced as the carbon source for graphene growth.

The synthesized graphene protected by polymer layer was gently lifted-off in 0.2 M ammonium persulfate solution. After a thorough rinse with distilled water to eliminate contaminants, the graphene was carefully transferred onto a SiO_2 substrate for further experimentation and analysis.

4.2.2 Fabrication of FET devices

The fabrication of FET devices commenced with the precise patterning of source and drain electrodes on Si/SiO_2 substrates using e-beam lithography. It was followed by the vapor deposition of a 5/50 nm Cr/Au layer onto the substrates, establishing the required electrical contacts for the FETs.

MoS_2/Graphene (MG) heterostructure fabrication. The assembly of MoS_2 layers onto the metal electrodes was achieved using a polystyrene (PS) transfer film. After the MoS_2 layer assembly, the device underwent vacuum drying and was subsequently immersed in toluene to dissolve and remove the PS layer. To ensure

contact between MoS_2 and the electrodes, the device was annealed at 200°C for 2 h in a hydrogen (10 sccm) and argon (300 sccm) atmosphere. The graphene layer, carried by a polymethyl methacrylate (PMMA) film, was then accurately aligned, and placed atop the MoS_2. This graphene layer application followed a similar procedure of vacuum drying, and acetone immersion. A final annealing step at 200°C for 2 hours under hydrogen and argon gases was essential to ensure the successful integration of the MoS_2 and graphene layers.

Graphene/MoS_2 (GM) heterostructure fabrication. The fabrication of the GM heterostructure paralleled that of the MG heterostructure, with a key distinction being the sequence of material transfer as illustrated in Figure 4.1. Initially, the graphene layer was transferred to the substrate using a PMMA film, and this step was followed by the transfer of the MoS_2 layer using a PS film. Both transfers necessitated meticulous alignment, application of the polymer films, vacuum drying, acetone, and toluene immersion to remove the polymers, and annealing to achieve a cohesive and stable heterostructure.

4.2.3 Functionalization

MG FET Device Functionalization. The functionalization of the MG FET device's graphene surface involved several carefully executed steps. Initially, the surface was treated with 20 μL of a 10 mM solution of PBASE (Sigma-Aldrich) in

dimethylformamide (DMF) for 2 h. PBASE molecules were non-covalently bonded to the graphene surface through π–π stacking interactions, leveraging the complementary aromatic structures of graphene and pyrene in PBASE.[18] Following this, the device underwent sequential rinses with DMF, methanol, and deionized water to eliminate unbound PBASE. Subsequently, the device's channel was incubated with 20 μL of a 50 μg/mL anti-human immunoglobulin G (HIgG, Sigma-Aldrich) antibody solution in 0.1× phosphate-buffered saline (PBS) at 4 °C for 12 h. This step involved covalently attaching antibodies to the PBASE molecules through the formation of amide bonds with the primary amine groups on the antibodies. The device was then rinsed with a 10 mM phosphate buffer (PB) at pH 7.4. The successful attachment of PBASE to graphene and antibodies to PBASE was confirmed using Raman spectroscopy and Atomic Force Microscopy (AFM). Finally, 20 μL of 0.1 M ethanolamine in PB was applied to each sensing site and incubated at room temperature for 30 minutes, followed by a PB rinse.

GM FET Device Functionalization. The GM FET devices underwent a different functionalization process. Devices were submerged in a 2% (v/v) TESBA (Gelest Inc.) solution in toluene in sealed containers, reacting for 2 h to allow for silane deposition.[11] Post-reaction, the devices were rinsed with ethanol and deionized water and subsequently dried. A back-dried step at 120 °C for 20 min was then performed.[19]

Antibody immobilization was carried out similarly to the MG FET devices, involving the immobilization of anti-HIgG antibodies in PBS to the channel, followed by incubation and rinsing with PB. The successful coupling of TESBA to MoS_2 and antibodies to TESBA was confirmed by X-ray Photoelectron Spectroscopy (XPS) and AFM. Ethanolamine treatment was performed as with the MG FET devices, involving incubation and subsequent rinsing.

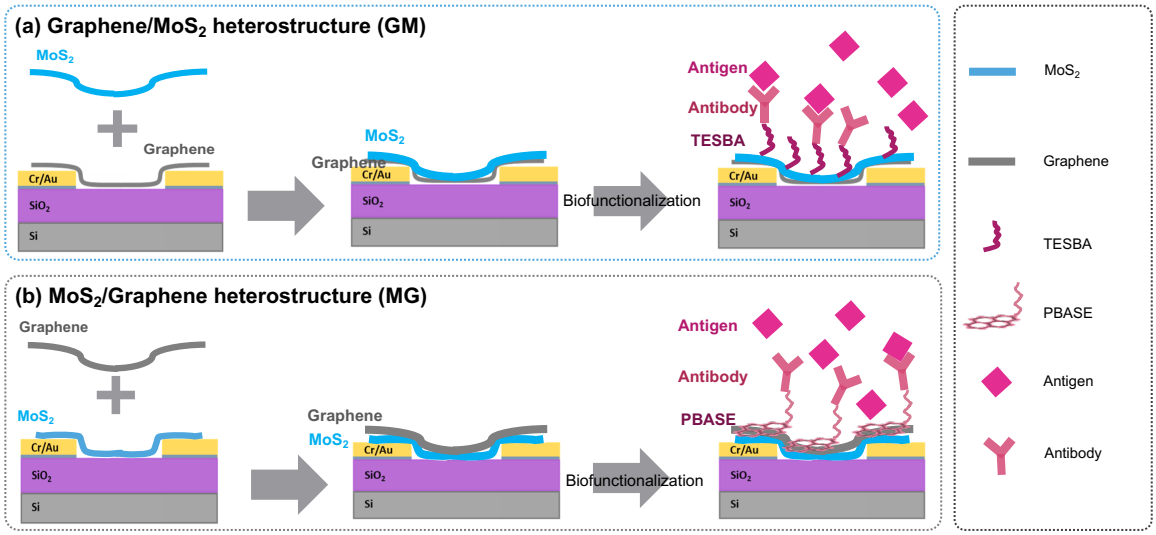

Figure 4.1. Schematic illustration of the FET devices fabrication, antibody immobilization and antigen detection of graphene and MoS_2 heterostructures based biosensors.

4.2.4 Optical and electrochemical characterization

Optical microscopy images were captured with a Nikon L150 Optical Microscope. Raman spectroscopy was carried out using a Horiba LabRam system with a 532 nm green laser with a minimal power of 5 mW as source, enabling the identification of molecular vibrations and chemical composition. AFM images were obtained using a Horiba LabRam/Aist-NT AFM system. XPS measurements were

conducted using a Kratos AXIS ULTRADLD XPS system with an Al Kα X-ray source and a 165 mm mean radius electron energy hemispherical analyzer. Vacuum pressure was meticulously maintained below 3×10^{-9} torr during the measurements. The Fourier transform infrared spectroscopy (FT-IR) spectra were obtained using a Nicolet 6700 FT-IR spectrometer.

FET transfer characteristic curves were acquired using a Keithley 2636 source meter from Tektronics. In this setup, a constant drain-source voltage (V_D) of 1 V was maintained while the back-gate voltage (V_G) was systematically swept from 0 V to 120 V. For resistance measurements, resistance was calculated from the linear region of the current-voltage curves, which were meticulously recorded across a range from -0.1 V to 0.1 V.

To accurately evaluate the real-time current responses and specificity of our FET biosensors, resistance-against-time (R-t) measurements were employed. These measurements were instrumental in assessing the biosensors' ability to distinguish between molecules similar to the targeted analyte. For specificity assessment of the sensing platform, bovine serum albumin (BSA, Sigma-Aldrich) and human serum albumin (HSA, Sigma-Aldrich) were selected as control proteins. Additionally, the R-t measurements played a key role in monitoring the biosensors' response to various concentrations of HIgG antigen. For real-time detection measurements, a constant bias

V_D = 1 V was applied without gate voltage. A custom-designed 30 μL polymethyl methacrylate (PMMA) cell was precisely positioned over each biosensor. Before the introduction of the samples, each FET biosensor underwent a stabilization period of 10–15 minutes to establish a baseline for current response. Following this stabilization, 200 μL of the sample, prepared in 10 mM PB, was sequentially added to the PMMA cell at 6 to 7-minute intervals. This methodical addition of samples was critical for eliciting stable and reliable current responses from the biosensors, thereby ensuring the accuracy and reproducibility of our measurements.

4.3 Results and Discussion

4.3.1 Materials characterizations

Both bare MoS_2 and graphene were synthesized using CVD method and characterized by optical images and AFM. The MoS_2 was grown directly on Si/SiO_2 substrate in continuous film and mainly comprises of single layer (Figure 4.2). The small MoS_2 flake was characterized by AFM with thickness of about 0.7 nm (Figure 4.2c). In Figure 4.3a, the Raman spectra of CVD-MoS_2 highlight two distinct peaks: E_{2g} at 393 cm^{-1} and A_{1g} at 415 cm^{-1}, representing the in-plane and out-of-plane vibrational modes. The notable separation of 19 cm^{-1} between these peaks indicates the monolayer structure of MoS_2.[20] The uniform color contrast in Figure 4.2d indicates that the graphene is continuous film. The height between the substrate and the graphene surface indicate sthe thickness of the graphene was 1.2 nm. Raman spectra in Figure

4.3b and 3c of our CVD graphene showed strong G peak at 1606 cm^{-1} and 2D peak at 2670 cm^{-1}. Raman spectra also denoted there were no defects introduced during both the growth phase and the subsequent transfer of the materials.

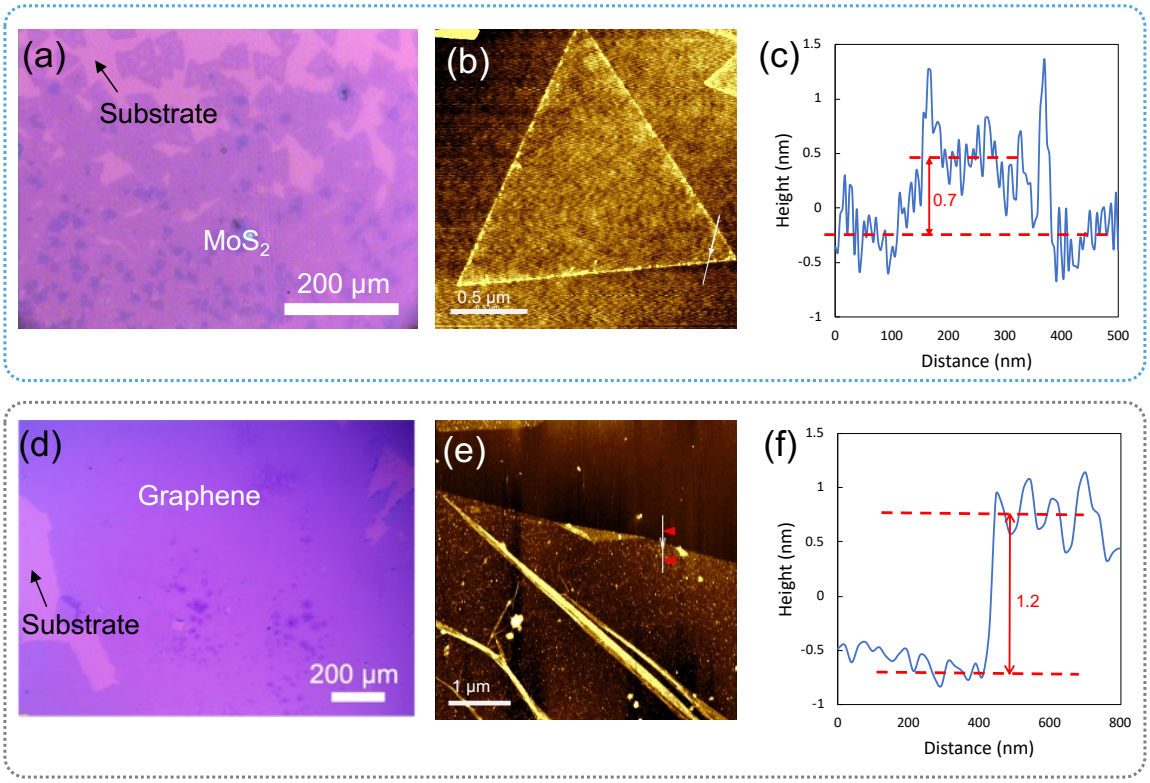

Figure 4.2. Optical images and AFM of MoS_2 and graphene: (a) a CVD-grown MoS_2 on an Si/SiO_2 substrate, (b) an AFM image of a MoS_2 flake with (c) its height profile, and (d) graphene synthesized via CVD on an Si/SiO_2 substrate, along with (e) its AFM image and (f) the corresponding height profile.

Following the synthesis of each material separately, the heterostructure was subsequently constructed through a physical stacking by capping graphene with MoS_2 (in which MoS_2 underneath of graphene, shortened for MoS_2/Graphene or MG as illustrated in Figure 4.1a), and capping MoS_2 with graphene (in which graphene underneath of MoS_2, shorten for Graphene/MoS_2 or GM as illustrated in Figure 4.1b).

Raman spectroscopy confirmed that the intrinsic properties of both materials remained intact post-transfer, ensuring their quality and compatibility within the heterostructure. The blueshift of A_{1g} mode (Figure 4.3a) in both MG and GM heterostructures indicates the existence of a Van der Waals interaction at the interface.[21,22] Figure 4.3b compares the G band of graphene in all cases. The G peak position shows a much larger shift of the MG compared with the case of GM. Since the measured Raman G peak position shifts $\Delta\Omega_G$ linearly with Fermi energy change ΔE_F, as $\Delta\Omega_G = |\Delta E_F| \times 42\ cm^{-1}\ eV^{-1}$.[22,23] The shift observed in the G band is attributed to the stacking and close interface between the layers. The stacking of MG leads to a much larger shift of the graphene G band, compared with the case of GM. For MG, G peaks downshift for 16 cm^{-1}, corresponding to a Fermi level shift of 0.38 eV in graphene due to contact with MoS_2, i.e., electron transfer from MoS_2 to graphene lifts up the graphene Fermi level by 0.38 eV; while for GM, G peaks downshift for 8 cm^{-1}, reflecting to a Fermi level shift of 0.19 eV in graphene due to contact with MoS_2 and electron transfer from MoS_2 to graphene lifting up the graphene Fermi level by 0.19 eV. The possible reason for the shift difference is that graphene becomes more sensitive when it is in contact with different bottom and/or top dielectric environments.[21,22] The positions of 2D peaks was also a function of doping, as shown in Figure 4.3c, both of the heterostructures' 2D peak showed blueshift, which means interaction within both

heterostructures results in the doping of the graphene layer.[6,24] The 2D peak upshift by 55 cm^{-1} for MG and the 2D peak upshift by 45 cm^{-1} for GM and the doping in MG is stronger than the doping in GM structure.

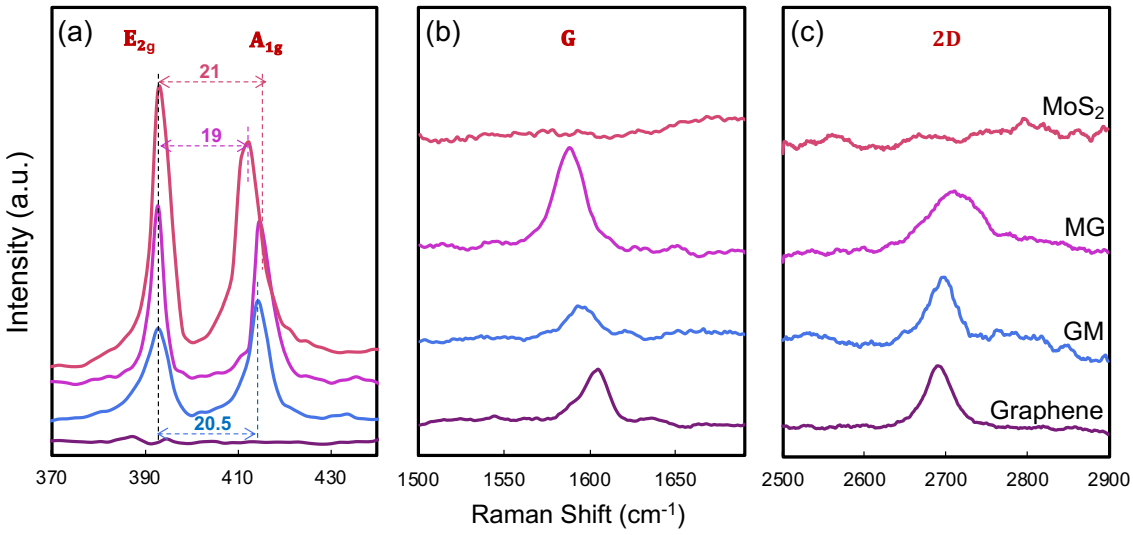

Figure 4.3. Raman spectra of MoS_2, graphene and heterostructures.

To enhance our comprehension of the electrical properties of heterostructures, we conducted comparative analyses of their resistances. Given in Figure 4.4a that graphene is known for its high conductivity and low resistance ~700 Ω, in contrast to MoS_2, which exhibits a high resistance of ~170 MΩ, the assembly of these materials into heterostructures provides insightful observations. The MG heterostructure demonstrated a resistance of ~1700 Ω, whereas the GM heterostructure showed a resistance ~800 Ω. This suggests the electrical performance of the heterostructures remains predominantly governed by the properties of graphene, indicating that the

simple physical stacking method does not significantly alter the conductive dominance of graphene within these composite structures.

To further investigate the effects of doping on electronic performance, the study assessed the electronic characteristics of back-gated FET performance for both MG and GM heterostructures. The FET transfer curves were plotted in Figure 4.4b. The high p-doping graphene transfer curve shows a charge neutrality points of gate voltage (V_{CNP}) at 96 V. The significant p-doping of graphene is frequently seen as a result of the photolithography process used for device patterning which typically incorporates steps of exposure to plasma and immersion in metal etching agents.[6] The presence of ambient adsorbents like water vapor and oxygen can further enhance the p-doping phenomenon. The noticeable difference of slopes in the right and left arms of the transfer curve indicate as-fabricated CVD graphene dominated by hole carriers. The MoS_2 FET curve shows the typical n-type performance of CVD grown MoS_2 at room temperature.

Both heterostructure FET shows ambipolar transfer characteristics and exhibits a shift in V_{CNP} compared with graphene. The V_{CNP} shifts to 84 V for GM indicating that graphene becomes less p-doped but more n-doped by MoS_2. This phenomenon, where graphene capped with MoS_2 exhibits a shift from p-type to more n-type characteristics, is attributed to the electrons migrate from MoS_2 to graphene. Under these conditions,

the normally p-doped multilayer graphene serves as a recipient for electrons originating from the n-doped MoS_2. Similar reported in the electronic properties of MoS_2 and graphene heterostructure was illustrated in our previous work.[6] On the other hand, the V_{CNP} is found at 72 V for MG which shows more n-doped effect by the MoS_2 compared with graphene and GM heterostructure. This discrepancy highlights the impact of physical stacking techniques on the interactions and charge transfer within the heterostructure. Such influences are critical in altering carrier mobility, thereby directly affecting the behavior of charge carriers within the heterostructure.

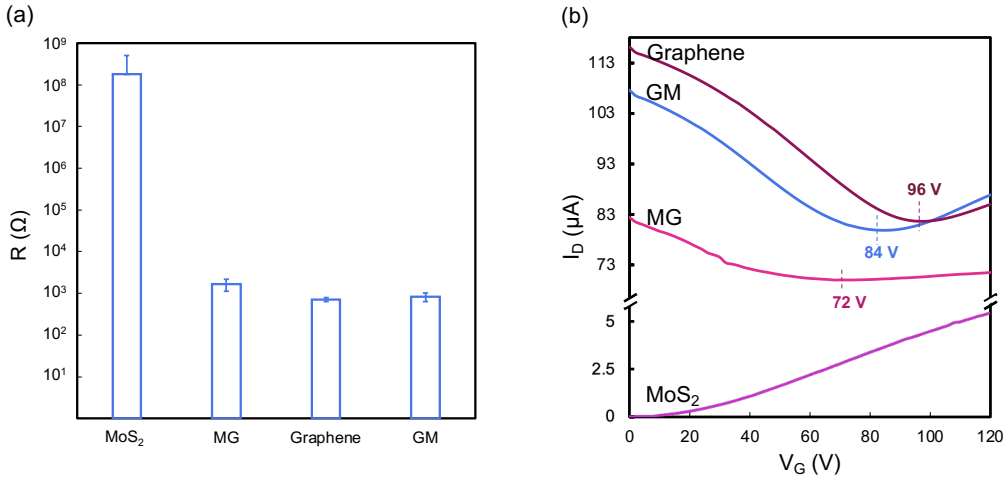

Figure 4.4. (a) resistance results and (b) representative transfer curve of MoS_2, graphene, MG and GM heterostructures.

4.3.2 Biofunctionalization

One advantage of using heterostructures in biosensors lies in the capacity to leverage the unique properties of both constituent materials, enabling specialized functionalization techniques to be tailored for each layer. By capitalizing on the distinct

attributes of MoS_2 and graphene, we implement specific functionalization strategies that are designed to complement the unique characteristics of each material in various configurations. For graphene with MoS_2 on top, we utilize a silane-based method that involves TESBA, while for MoS_2 with graphene on top, we utilize a PBASE-based approach. This deliberate choice ensures that the functionalization process is perfectly attuned to the inherent properties of the material on the upper layer of each heterostructure. Consequently, we compare the two approaches for the biofunctionalization of graphene and MoS_2 through a two-step biofunctionalization process, characterized by XPS, Raman spectroscopy, and AFM characterizations.

To determine the chemical composition of MoS_2 modified with TESBA, XPS spectral analysis was conducted on gold substrate. The wide-scan spectra of both MoS_2/Au, MoS_2-TESBA/Au, and MoS_2-TESBA-antibody/Au as shown in Figure 4.5a, reveal the presence of Mo, S, C, and O elements. These elements are observed in the MoS_2/Au, MoS_2-TESBA/Au, and MoS_2-TESBA-antibody/Au samples. Notably, the Si element is detected in the MoS_2-TESBA sample (as detailed in Figure 4.5c), confirming the successful incorporation of TESBA onto the MoS_2 surface. Furthermore, an increased O1s intensity in the MoS_2-TESBA spectrum, primarily attributed to TESBA, suggests successful integration of TESBA with MoS_2. Upon antibody immobilization on TESBA, the detection of the N element from the antibody (Figure 4.5b) indicates

successful immobilization. The peak observed at 401 eV could be an overlap between N1s and Mo 3p.

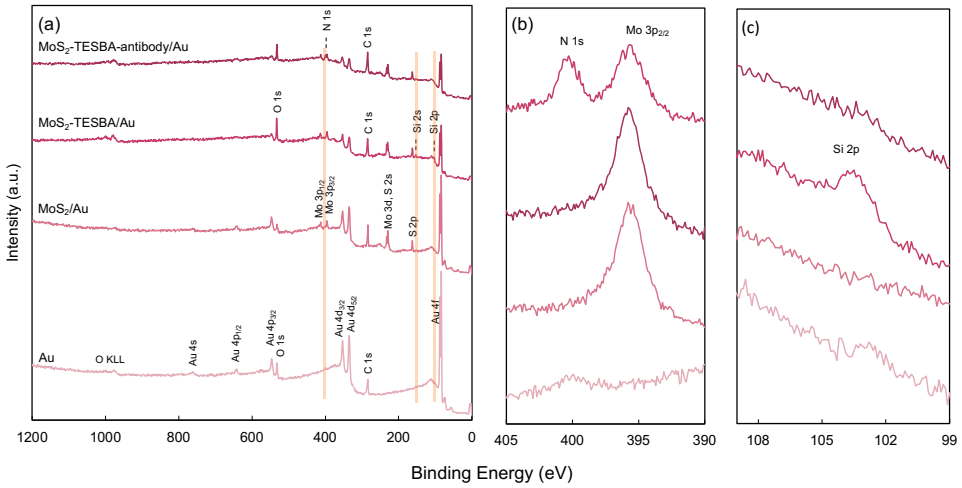

Figure 4.5. (a) XPS survey spectra of MoS_2 at different stages of functionalization spotted on a gold substrate. (b) High-resolution XPS spectra of N 1s and Mo 3p peaks. (c) High-resolution XPS spectra of Si 2p peaks.

Raman spectroscopy was applied to confirm the presence of PBASE on the surface of the FET biosensor. Figure 4.6 displays the averaged Raman spectra for bare graphene, PBASE-functionalized graphene, and antibody-immobilized graphene, derived from multiple measurements across each sample to thoroughly assess the impact of PBASE functionalization on graphene quality. Before functionalization, the D peak at 1350 cm^{-1} was observed, typically associated with graphene's structural defects. After PBASE functionalization, this D peak intensified and broadened, indicating increased structural irregularities. Furthermore, PBASE-specific intrinsic signals emerged, notably a peak at 1626 cm^{-1} corresponding to pyrene group resonance

and a peak at 1401 cm^{-1}, reflecting disorder from orbital hybridization with the graphene plane.[25] A notable shift (~7 cm^{-1}) in the 2D peak frequency of the graphene films to a higher value (as illustrated in Figure 4.6) suggests hole doping by PBASE.[16,18] While the antibody immobilization's doping effect on both the G band and the 2D peak was less pronounced than that of PBASE, it nonetheless led to enhanced signals at 1357 cm^{-1}, and 1401 cm^{-1}. Additionally, a subtle shift (~3 cm^{-1}) towards a lower frequency in the 2D peak was observed following antibody immobilization, further indicating the interaction between the antibody and the PBASE functionalized graphene surface.

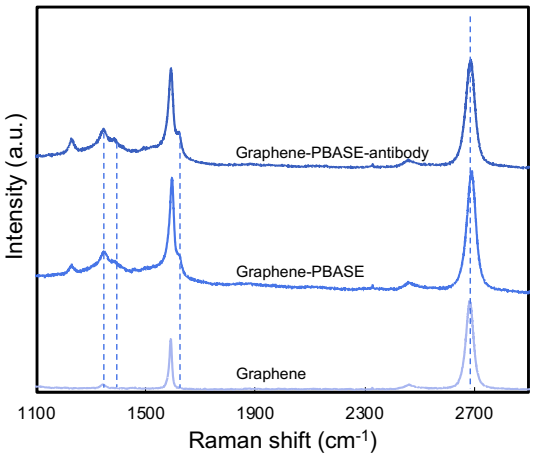

Figure 4.6. Raman spectra of bare graphene, PBASE functionalized graphene, and antibody immobilized graphene.

AFM is employed to examine the alterations in surface topography resulting from the biofunctionalization process. Figure 4.7a-d present the AFM images of the bare MoS_2, TESBA conjunctions and after antibody immobilization and after antigen attachment, respectively. We observe small clusters of thicker materials attributed to

non-uniform MoS_2 growth on the edge, which contributes to more active sites for functionalization. Bare MoS_2 exhibits a rms roughness less than 1.7 nm. After the TESBA conjunctions, the surface roughness increases to 2.5 nm. Subsequently, the surface roughness was noted to elevate to 3 nm following antibody immobilization, and a further increase of 4.1 nm was observed upon the attachment of antigens. Figure 4.7f-j shows the changes of graphene biofunctionalization which resulted in the morphology of the surface after the linker modification, the immobilization of the antibody, and the capture with antigen. Ripples and wrinkles observed in large-area graphene (as shown in Figure 4.7f-i) are a result of the transfer process. Additionally, the presence of small clusters of thicker materials is identified as residues which were not eliminated during the cleaning and transferring procedures of the graphene. The surface roughness changes during biofunctionalization of graphene are nearly analogous to MoS_2, which shows progressively increase after antibody immobilization and antigen detection (Figure 4.7j).[26,27]

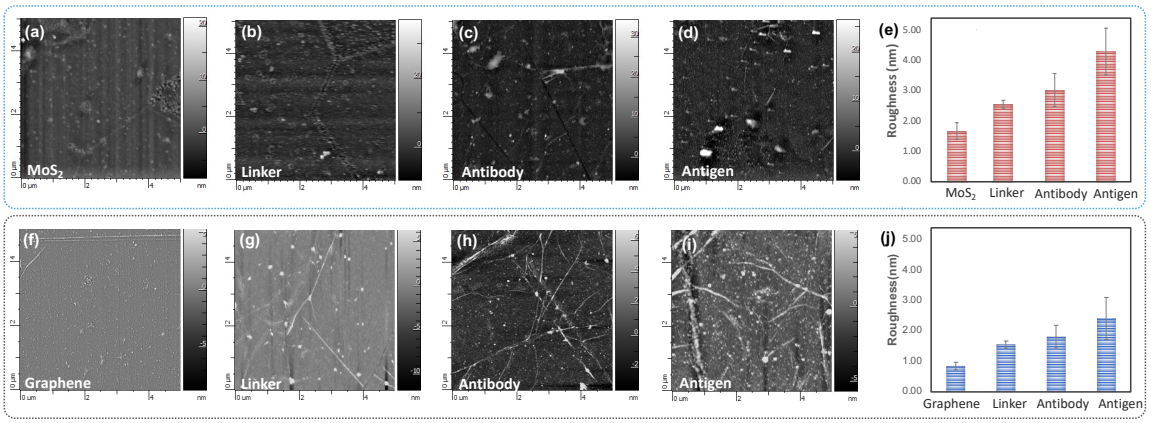

Figure 4.7. The AFM image of (a) bare MoS_2, (b) TESBA conjunctions (c) after antibody immobilization, and (d) after antigen attachment of MoS_2 surface. (e) The rms roughness changes of MoS_2 surface functionalization process. The image of (f) bare graphene, (g) PBASE conjunctions, (h) after antibody immobilization, and (i) after antigen attachment of graphene surface. (j) The rms roughness changes of graphene surface functionalization process. AFM images were obtained within a 5 μm × 5 μm area.

4.3.3 Biosensing performance

Transfer curves of two heterostructures biosensors are obtained to detect varying concentrations of HIgG analyte. The sensing properties were assessed through the shift in the V_{CNP}, which is defined as $\Delta V_{CNP} = V_{CNP} - V_{CNP0}$, where V_{CNP0} and V_{CNP} are the charge neutrality point before and after the addition of target. Upon introduction of a low HIgG concentration (10^{-4} ng/mL), a discernible rightward shift was observed for both MG (Figure 4.8a) and GM (Figure 4.8b) heterostructure biosensors coupled with a increase in the overall current level. At higher HIgG concentrations, the transfer curves exhibited further rightward shifts, and the V_{CNP} values increased accordingly. These shifts and the current changes suggest that HIgG binding to the functionalized heterostructure surface results in changes to the local charge environment. The

interaction of HIgG with the biosensor's surface receptors leads to an alteration in the electrostatics environment of the heterostructures surface, impacting charge carrier distribution. These changes are sensitively detected by the FET, which reflects them as variations in carrier mobility. Specifically, the binding event can lead to a change in the carrier mobility, which can be calculated from the linear region of the transfer curves for each analyte concentration and summarized in Figure 4.8c. The mobility (μ) of charge carriers in a FET was calculated using the following equation:[28]

$$\mu = \frac{g_m L}{W C_{ox} V_D}$$

where g_m is the transconductance, which is the slope of the transfer curves in the linear region. L and W are the length and width of the channel, which are both specified as 10 μm. C_{ox} is the capacitance per unit area of the gate oxide. For a gate oxide composed of 300 nm thick SiO_2, C_{ox} has been calculated to be 1.15×10^{-8} F/cm^2.[29] In comparing the sensing performances of the MG and GM heterostructure biosensors when detecting HIgG, distinct behaviors were observed in response to increasing analyte concentrations. For the MG heterostructure, the mobility of holes remained largely unchanged, while there was a slight decrease in electron mobility. In contrast, the GM heterostructure exhibited an increase in hole mobility and a decrease in electron mobility as the concentration of HIgG analyte increased. This variance suggests that the electrostatic environment created by the analyte-receptor complex

has a more pronounced impact on the GM heterostructure, significantly affecting the distribution of charge carriers. This difference in response highlights the unique electronic interactions occurring within each heterostructure upon HIgG binding. The calibration curves in Figure 4.8d, which were derived from the shifts in the V_{CNP}, provide further insights into the biosensors' performance and offer a comprehensive overview of the biosensors' responses across a range of HIgG concentrations. A linear relationship is observed between the shift in ΔV_{CNP} and the concentration HIgG, which fits to the linear equation for both heterostructures, $y = 0.0325\ln x + 0.4266$ for GM heterostructure and $y = 0.0098\ln x + 0.3451$ for MG heterostructure FET biosensors. The limit of detection (LOD) was determined followed the same method described in our previous work.[30] The results showed that the GM biosensor has higher sensitivity (0.0325 vs 0.0098 per ln[HIgG, ng/mL]) and lower LOD (1.24×10^{-5} ng/mL vs 2.64×10^{-5} ng/mL) compared to MG biosensor. Both heterostructures FET biosensors exhibit comparable LODs to existing MoS_2 FET biosensors, as summarized in Table 4.1. Furthermore, they have demonstrated higher LODs than simple graphene FET biosensors for antibody detection.

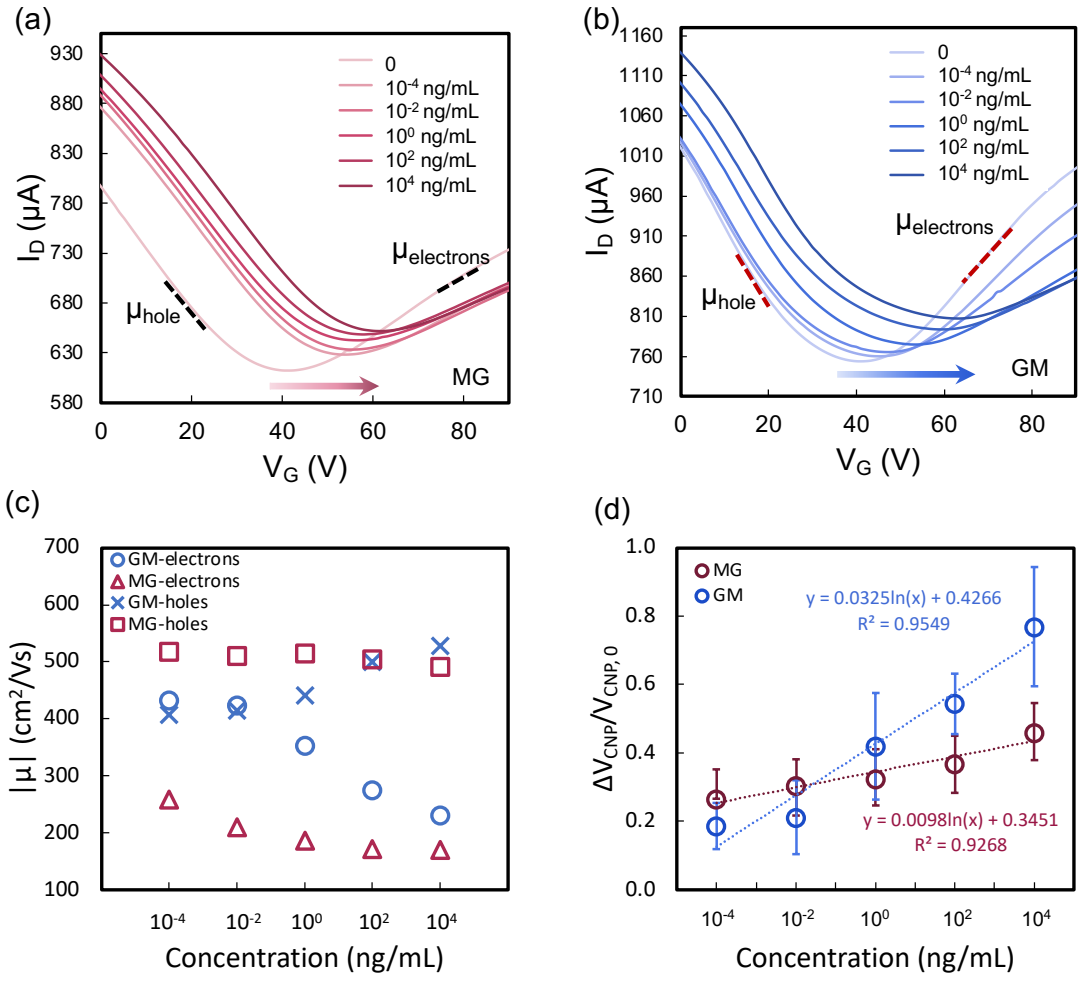

Figure 4.8. (a) Representative transfer curves for various concentrations of the HIgG antigen using (a) an MG FET biosensor and (b) a GM FET biosensor. (c) Calculated carrier mobility from the linear regions of the transfer curves in (a) and (b). (d) Concentration-dependent calibration curves for the HIgG antigen, demonstrating the shifts in the charge neutrality point of gate voltage (ΔV_{CNP}) for both MG FET (red line) and GM FET (blue line) biosensors.

Table 4.1. Summary and comparison of MoS_2, graphene, graphene and MoS_2 heterostructures FET biosensors for antibody detections.

Materials	Antibody type	Detection range	LOD or detection limit	Reference
MoS_2	prostate-specific antigen (PSA)	10^{-3} to 10 ng/mL		31
Multi-layer MoS_2	PSA	3.75 nM to 375 fM		32
Multilayer MoS_2	PSA	10^{-5} to 1 ng/mL	100 fg/mL	33
Few-layer MoS_2	PSA	10^{-6} to 100 ng/mL	1 fg/mL	34
Multilayer MoS_2	SARS-CoV-2 spike protein	10^{-6} to 1 ng/mL		13
Vertically aligned MoS_2	PSA	10^{-2} to 10 ng/mL	800 fg/mL	35
Multilayer MoS_2	IgG	10^{-3} to 10^{-1} ng/mL		36
Graphene	Bone gla protein	10^{-5} to 10^{2} ng/mL	100 fg/mL (in 0.5% serum)	37
Graphene	SARS-CoV-2 Spike S1 antigen	1 fM to 1 μM	10 fM	38
Porous graphene	SARS-CoV-2 virus	1 to 10^{6} pg/mL	1 pg/mL (1 ng/mL in human serum)	39
Monolayer graphene	SARS-CoV-2 antibody	5 aM to 5 pM	0.39 fg/mL	40
Vertically oriented graphene	HIgG	2 to 20 ng/mL	2 ng/mL	41
GM	HIgG	10^{-4} to 10^{6} ng/mL	12.4 fg/mL	This work
MG	HIgG	10^{-4} to 10^{6} ng/mL	26.4 fg/mL	This work

Figure 4.9 offers an insightful comparative analysis of the real-time resistance responses exhibited by MG and GM biosensors when exposed to various biomolecular solutions. Both biosensors were tested against solutions of HSA, BSA, and HIgG. For both MG and GM heterostructures biosensors, no obvious change in resistance was observed upon the addition of bare PB and non-target biomolecules of HSA and BSA in high concentrations. Conversely, a noticeable change in resistance was observed upon the addition of HIgG solutions, indicating a strong interaction between the biosensor surface and the HIgG molecules. The response to HSA and BSA, on the other hand, was relatively muted, suggesting a high degree of specificity of the MG biosensor towards HIgG. This specificity is crucial for applications where accurate detection of HIgG is essential. Furthermore, the analysis of resistance changes at different concentrations of HIgG (10^2 ng/mL and 10^4 ng/mL) provides valuable insights into the biosensors' sensitivity. Both MG and GM biosensors exhibited a concentration-dependent response, with higher concentrations of HIgG leading to more significant changes in resistance. This concentration-dependent behavior is indicative of the potential of these biosensors for quantitative analysis that require high specificity and sensitivity in clinical and diagnostic applications.

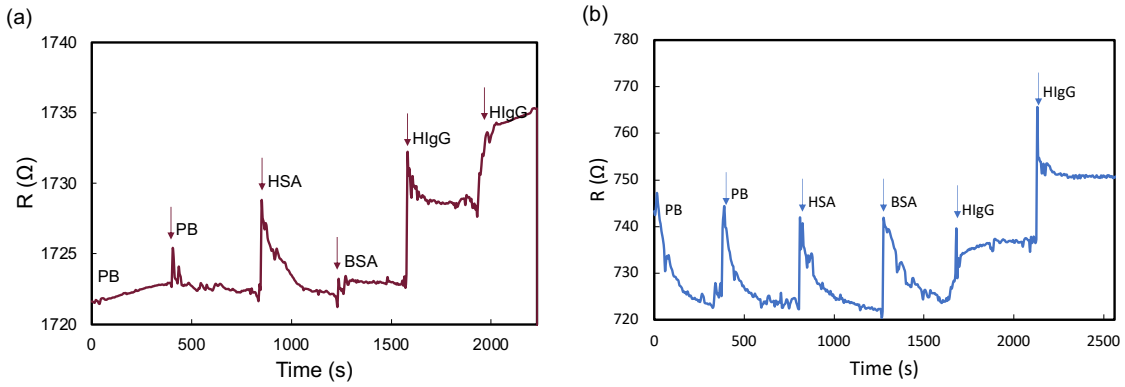

Figure 4.9. R-t measurement of (a) MG biosensor and (b) GM biosensor upon the addition of different biomolecular solutions. All analyte solutions prepared in 10 mM PB consisted of 10^2 ng/mL of HSA, 10^2 ng/mL of BSA, 10^2 ng/mL and 10^4 ng/mL of HIgG.

4.4 Conclusions

In conclusion, we have presented an experimental study on biomolecule sensing using vertical MoS_2-Graphene heterostructures based FET biosensors, highlighting the synthesis and fabrication processes of MoS_2 and graphene via CVD, and the subsequent assembly into MG and GM heterostructures. We employ specialized functionalization techniques for each configuration tailored to each topping material's unique properties: graphene with MoS_2 on top uses a silane-based method with TESBA, and MoS_2 with graphene on top utilizes PBASE. Biofunctionalization techniques for both heterostructures are detailed, leading to specific biomolecular detection. Optical, electrochemical characterization, and FET device performance are thoroughly investigated. Our study demonstrates that GM heterostructures exhibit higher sensitivity and lower LOD for HIgG antigen compared to MG configurations, with GM showing a sensitivity of 0.0325 vs 0.0098 per ln[HIgG, ng/mL] and a LOD of 1.24×10^{-5}

ng/mL vs 2.64×10^{-5} ng/mL for MG. This suggests the GM configuration's superior performance in biosensing due to its enhanced charge carrier distribution when interaction with biomolecules. The study showcases the potential of these heterostructures in biosensing applications, with distinct advantages in carrier mobility and limit of detection highlighted through comprehensive data analysis. This research offers valuable insights for future endeavors aimed at optimizing the functionality of biosensors based on graphene and MoS_2 heterostructures.

4.5 References

(1) Yoon, J.; Lim, J.; Shin, M.; Lee, S.-N.; Choi, J.-W. Graphene/MoS2 Nanohybrid for Biosensors. Materials 2021, 14 (3), 518. https://doi.org/10.3390/ma14030518.

(2) Pham, P. V.; Bodepudi, S. C.; Shehzad, K.; Liu, Y.; Xu, Y.; Yu, B.; Duan, X. 2D Heterostructures for Ubiquitous Electronics and Optoelectronics: Principles, Opportunities, and Challenges. Chem. Rev. 2022, 122 (6), 6514–6613. https://doi.org/10.1021/acs.chemrev.1c00735.

(3) Azadmanjiri, J.; Srivastava, V. K.; Kumar, P.; Sofer, Z.; Min, J.; Gong, J. Graphene-Supported 2D Transition Metal Dichalcogenide van Der Waals Heterostructures. Applied Materials Today 2020, 19, 100600. https://doi.org/10.1016/j.apmt.2020.100600.

(4) Yu, Y.-J.; Zhao, Y.; Ryu, S.; Brus, L. E.; Kim, K. S.; Kim, P. Tuning the Graphene Work Function by Electric Field Effect. Nano Lett. 2009, 9 (10), 3430–3434. https://doi.org/10.1021/nl901572a.

(5) Kim, T.; Fan, S.; Lee, S.; Joo, M.-K.; Lee, Y. H. High-Mobility Junction Field-Effect Transistor via Graphene/MoS2 Heterointerface. Sci Rep 2020, 10 (1), 13101. https://doi.org/10.1038/s41598-020-70038-6.

(6) Pham, T.; Ramnani, P.; Villarreal, C. C.; Lopez, J.; Das, P.; Lee, I.; Neupane, M. R.; Rheem, Y.; Mulchandani, A. MoS2-Graphene Heterostructures as Efficient Organic Compounds Sensing 2D Materials. Carbon 2019, 142, 504–512. https://doi.org/10.1016/j.carbon.2018.10.079.

(7) Ignatova, T.; Pourianejad, S.; Li, X.; Schmidt, K.; Aryeetey, F.; Aravamudhan, S.; Rotkin, S. V. Multidimensional Imaging Reveals Mechanisms Controlling Multimodal Label-Free Biosensing in Vertical 2DM-Heterostructures. ACS Nano 2022, 16 (2), 2598–2607. https://doi.org/10.1021/acsnano.1c09335.

(8) Stergiou, A.; Tagmatarchis, N. Molecular Functionalization of Two-Dimensional MoS 2 Nanosheets. Chemistry A European J 2018, 24 (69), 18246–18257. https://doi.org/10.1002/chem.201803066.

(9) Presolski, S.; Pumera, M. Covalent Functionalization of MoS2. Materials Today 2016, 19 (3), 140–145. https://doi.org/10.1016/j.mattod.2015.08.019.

(10) Li, X.; Li, Y.; Qiu, Q.; Wen, Q.; Zhang, Q.; Yang, W.; Yuwen, L.; Weng, L.; Wang, L. Efficient Biofunctionalization of MoS2 Nanosheets with Peptides as Intracellular Fluorescent Biosensor for Sensitive Detection of Caspase-3 Activity. Journal of Colloid and Interface Science 2019, 543, 96–105. https://doi.org/10.1016/j.jcis.2019.02.011.

(11) Martin, H. J.; Schulz, K. H.; Bumgardner, J. D.; Walters, K. B. An XPS Study on the Attachment of Triethoxsilylbutyraldehyde to Two Titanium Surfaces as a Way to Bond Chitosan. Applied Surface Science 2008.

(12) Sen, A.; Shim, J.; Bala, A.; Park, H.; Kim, S. Boosting Sensitivity and Reliability in Field-Effect Transistor-Based Biosensors with Nanoporous MoS2 Encapsulated by Non-Planar Al 2 O 3. Adv Funct Materials 2023, 33(42),2301919.https://doi.org/10.1002/adfm.202301919.

(13) Wei, J.; Zhao, Z.; Luo, F.; Lan, K.; Chen, R.; Qin, G. Sensitive and Quantitative Detection of SARS-CoV-2 Antibodies from Vaccinated Serum by MoS 2 -Field Effect Transistor. 2D Mater. 2022, 9 (1), 015030. https://doi.org/10.1088/2053-1583/ac40c4.

(14) Georgakilas, V.; Otyepka, M.; Bourlinos, A. B.; Chandra, V.; Kim, N.; Kemp, K. C.; Hobza, P.; Zboril, R.; Kim, K. S. Functionalization of Graphene: Covalent and Non-Covalent Approaches, Derivatives and Applications. Chem. Rev. 2012, 112 (11), 6156–6214. https://doi.org/10.1021/cr3000412.

(15) Islam, K.; Suhail, A.; Pan, G. A Label-Free and Ultrasensitive Immunosensor for Detection of Human Chorionic Gonadotrophin Based on Graphene FETs. Biosensors 2017, 7 (3), 27. https://doi.org/10.3390/bios7030027.

(16) Kwong Hong Tsang, D.; Lieberthal, T. J.; Watts, C.; Dunlop, I. E.; Ramadan, S.; Del Rio Hernandez, A. E.; Klein, N. Chemically Functionalised Graphene FET Biosensor for the Label-Free Sensing of Exosomes. Sci Rep 2019, 9 (1), 13946. https://doi.org/10.1038/s41598-019-50412-9.

(17) Maidin, N. N. M.; Rahim, R. A.; Halim, N. H. A.; Abidin, A. S. Z.; Ahmad, N. A.; Lockman, Z. Interaction of Graphene Electrolyte Gate Field-Effect Transistor for Detection of Cortisol Biomarker; Bandung, Indonesia, 2018; p020022. https://doi.org/10.1063/1.5080835.

(18) Khan, N. I.; Mousazadehkasin, M.; Ghosh, S.; Tsavalas, J. G.; Song, E. An Integrated Microfluidic Platform for Selective and Real-Time Detection of Thrombin Biomarkers Using a Graphene FET. Analyst 2020, 145 (13), 4494–4503. https://doi.org/10.1039/D0AN00251H.

(19) Lan, Y.-W.; Hong, C.-J.; Chen, P.-C.; Lin, Y.-Y.; Yang, C.-H.; Chu, C.-J.; Li, M.-Y.; Li, L.-J.; Su, C.-J.; Wu, B.-W.; Hou, T.-H.; Li, K.-S.; Zhong, Y.-L. Nonvolatile Molecular Memory with the Multilevel States Based on MoS 2 Nanochannel Field Effect Transistor through Tuning Gate Voltage to Control Molecular Configurations. Nanotechnology 2020, 31 (27), 275204. https://doi.org/10.1088/1361-6528/ab82d7.

(20) Zhan, Y.; Liu, Z.; Najmaei, S.; Ajayan, P. M.; Lou, J. Large-Area Vapor-Phase Growth and Characterization of MoS 2 Atomic Layers on a SiO 2 Substrate. Small 2012, 8 (7), 966–971. https://doi.org/10.1002/smll.201102654.

(21) Zhou, K.-G.; Withers, F.; Cao, Y.; Hu, S.; Yu, G.; Casiraghi, C. Raman Modes of MoS 2 Used as Fingerprint of van Der Waals Interactions in 2-D Crystal-Based Heterostructures. ACS Nano 2014, 8 (10), 9914–9924. https://doi.org/10.1021/nn5042703.

(22) Zhao, M.; Song, P.; Teng, J. Electrically and Optically Tunable Responses in Graphene/Transition-Metal-Dichalcogenide Heterostructures. ACS Appl. Mater. Interfaces 2018, 10 (50), 44102–44108. https://doi.org/10.1021/acsami.8b12588.

(23) Chen, C.-F.; Park, C.-H.; Boudouris, B. W.; Horng, J.; Geng, B.; Girit, C.; Zettl, A.; Crommie, M. F.; Segalman, R. A.; Louie, S. G.; Wang, F. Controlling Inelastic Light Scattering Quantum Pathways in Graphene. Nature 2011, 471 (7340), 617–620. https://doi.org/10.1038/nature09866.

(24) Das, A.; Pisana, S.; Chakraborty, B.; Piscanec, S.; Saha, S. K.; Waghmare, U. V.; Novoselov, K. S.; Krishnamurthy, H. R.; Geim, A. K.; Ferrari, A. C.; Sood, A. K. Monitoring Dopants by Raman Scattering in an Electrochemically Top-Gated Graphene Transistor. Nature Nanotech 2008, 3 (4), 210–215. https://doi.org/10.1038/nnano.2008.67.

(25) Liu, Y.; Yuan, L.; Yang, M.; Zheng, Y.; Li, L.; Gao, L.; Nerngchamnong, N.; Nai, C. T.; Sangeeth, C. S. S.; Feng, Y. P.; Nijhuis, C. A.; Loh, K. P. Giant Enhancement in Vertical Conductivity of Stacked CVD Graphene Sheets by Self-Assembled

Molecular Layers. Nat Commun 2014, 5 (1), 5461. https://doi.org/10.1038/ncomms6461.

(26) To, T. D.; Nguyen, A. T.; Phan, K. N. T.; Truong, A. T. T.; Doan, T. C. D.; Dang, C. M. Modification of Silicon Nitride Surfaces with GOPES and APTES for Antibody Immobilization: Computational and Experimental Studies. Adv. Nat. Sci: Nanosci. Nanotechnol. 2015, 6 (4), 045006. https://doi.org/10.1088/2043-6262/6/4/045006.

(27) Zeng, Q.; Zhang, Y.; Song, K.; Kong, X.; Aalders, M. C. G.; Zhang, H. Enhancement of Sensitivity and Specificity of the Fluoroimmunoassay of Hepatitis B Virus Surface Antigen through "Flexible" Coupling between Quantum Dots and Antibody. Talanta 2009, 80 (1), 307–312. https://doi.org/10.1016/j.talanta.2009.06.061.

(28) Forsyth, R.; Devadoss, A.; Guy, O. Graphene Field Effect Transistors for Biomedical Applications: Current Status and Future Prospects. Diagnostics 2017, 7 (3), 45. https://doi.org/10.3390/diagnostics7030045.

(29) Li, J.; Song, E.; Chiang, C.-H.; Yu, K. J.; Koo, J.; Du, H.; Zhong, Y.; Hill, M.; Wang, C.; Zhang, J.; Chen, Y.; Tian, L.; Zhong, Y.; Fang, G.; Viventi, J.; Rogers, J. A. Conductively Coupled Flexible Silicon Electronic Systems for Chronic Neural Electrophysiology. Proc. Natl. Acad. Sci. U.S.A. 2018, 115 (41). https://doi.org/10.1073/pnas.1813187115.

(30) Pham, T.; Li, G.; Bekyarova, E.; Itkis, M. E.; Mulchandani, A. MoS 2 -Based Optoelectronic Gas Sensor with Sub-Parts-per-Billion Limit of NO 2 Gas Detection. ACS Nano 2019, 13 (3), 3196–3205. https://doi.org/10.1021/acsnano.8b08778.

(31) Lee, J.; Dak, P.; Lee, Y.; Park, H.; Choi, W.; Alam, M. A.; Kim, S. Two-Dimensional Layered MoS2 Biosensors Enable Highly Sensitive Detection of Biomolecules. Sci Rep 2014, 4 (1), 7352. https://doi.org/10.1038/srep07352.

(32) Wang, L.; Wang, Y.; Wong, J. I.; Palacios, T.; Kong, J.; Yang, H. Y. Functionalized MoS 2 Nanosheet-Based Field-Effect Biosensor for Label-Free Sensitive Detection of Cancer Marker Proteins in Solution. Small 2014, 10 (6), 1101–1105. https://doi.org/10.1002/smll.201302081.

(33) Park, H.; Han, G.; Lee, S. W.; Lee, H.; Jeong, S. H.; Naqi, M.; AlMutairi, A.; Kim, Y. J.; Lee, J.; Kim, W.; Kim, S.; Yoon, Y.; Yoo, G. Label-Free and Recalibrated

Multilayer MoS 2 Biosensor for Point-of-Care Diagnostics. ACS Appl. Mater. Interfaces 2017, 9 (50), 43490–43497. https://doi.org/10.1021/acsami.7b14479.

(34) Zhang, Y.; Feng, D.; Xu, Y.; Yin, Z.; Dou, W.; Habiba, U. E.; Pan, C.; Zhang, Z.; Mou, H.; Deng, H.; Mi, X.; Dai, N. DNA-Based Functionalization of Two-Dimensional MoS2 FET Biosensor for Ultrasensitive Detection of PSA. Applied Surface Science 2021, 548, 149169. https://doi.org/10.1016/j.apsusc.2021.149169.

(35) Song, P.; Ou, P.; Wang, Y.; Yuan, H.; Duan, S.; Chen, L.; Fu, H.; Song, J.; Liu, X. An Ultrasensitive FET Biosensor Based on Vertically Aligned MoS2 Nanolayers with Abundant Surface Active Sites. Analytica Chimica Acta 2023, 1252, 341036. https://doi.org/10.1016/j.aca.2023.341036.

(36) Ji, Z.; Wei, J.; Luo, F.; Liu, Z.; Lu, H.; Chen, R.; Wang, Y.; Qin, G. Investigating on Sensing Mechanism of MoS 2 -FET Biosensors in Response to Proteins. Nanotechnology 2023, 34 (43), 435503. https://doi.org/10.1088/1361-6528/aceb6a.

(37) Kanai, Y.; Ohmuro-Matsuyama, Y.; Tanioku, M.; Ushiba, S.; Ono, T.; Inoue, K.; Kitaguchi, T.; Kimura, M.; Ueda, H.; Matsumoto, K. Graphene Field Effect Transistor-Based Immunosensor for Ultrasensitive Noncompetitive Detection of Small Antigens. ACS Sens. 2020, 5 (1), 24–28. https://doi.org/10.1021/acssensors.9b02137.

(38) Shahdeo, D.; Chauhan, N.; Majumdar, A.; Ghosh, A.; Gandhi, S. Graphene-Based Field-Effect Transistor for Ultrasensitive Immunosensing of SARS-CoV-2 Spike S1 Antigen. ACS Appl. Bio Mater. 2022, 5 (7), 3563–3572. https://doi.org/10.1021/acsabm.2c00503.

(39) Cui, T.-R.; Qiao, Y.-C.; Gao, J.-W.; Wang, C.-H.; Zhang, Y.; Han, L.; Yang, Y.; Ren, T.-L. Ultrasensitive Detection of COVID-19 Causative Virus (SARS-CoV-2) Spike Protein Using Laser Induced Graphene Field-Effect Transistor. Molecules 2021, 26 (22), 6947. https://doi.org/10.3390/molecules26226947.

(40) Kang, H.; Wang, X.; Guo, M.; Dai, C.; Chen, R.; Yang, L.; Wu, Y.; Ying, T.; Zhu, Z.; Wei, D.; Liu, Y.; Wei, D. Ultrasensitive Detection of SARS-CoV-2 Antibody by Graphene Field-Effect Transistors. Nano Lett. 2021, 21 (19), 7897–7904. https://doi.org/10.1021/acs.nanolett.1c00837.

(41) Mao, S.; Yu, K.; Chang, J.; Steeber, D. A.; Ocola, L. E.; Chen, J. Direct Growth of Vertically-Oriented Graphene for Field-Effect Transistor Biosensor. Sci Rep 2013, 3 (1), 1696. https://doi.org/10.1038/srep01696.

Chapter 5

Conclusions

5.1 Summary

Our work has systematically explored the development, optimization, and application of 2D MoS_2-based optoelectronic biosensors, underpinning a significant leap in biosensing technology with potential applications in flexible and wearable sensors for early disease diagnostics. In this essay, we have explored a foundational advancement by employing low-energy visible red-light excitation on a flexible substrate to achieve rapid and selective biomolecule detection with significantly improved limits of detection.

Through the integration of MoS_2 with graphene electrodes and the innovative use of optoelectronics, we demonstrate substantial enhancements in sensitivity, specificity, and operational stability of FET biosensors for the detection of human immunoglobulin G and potentially other biomolecules. Further, the investigation on biomolecule sensing using hybrid MoS_2-Graphene heterostructures FET optoelectronics has elucidated the superior performance of the biosensor, highlighting the importance of strategic material assembly and functionalization in optimizing biosensor performance. This configuration has demonstrated the device's enhanced conductivity when interacting with biomolecules, leading to higher sensitivity and

lower LOD. The integration of graphene as contact electrodes in MoS_2 FETs has been shown to form a robust hybrid optoelectronic platform that not only addresses the poor conductivity issue but also enhances the biosensor's photocurrent, sensitivity, and flexibility, making it well-suited for point-of-care medical applications.

Furthermore, we have presented a study on biomolecule sensing using two vertical MoS_2-Graphene heterostructures based FET biosensors, highlighting the synthesis and fabrication processes of MoS_2 and graphene via CVD, and the subsequent assembly into MG and GM heterostructures. We employed specialized biofunctionalization techniques leading to specific biomolecular detection for each configuration tailored to each topping material's unique properties: graphene with MoS_2 on top uses a silane-based method with TESBA, and MoS_2 with graphene on top uses PBASE. Optical and electrochemical characterization are thoroughly investigated to characterize the two heterostructures FET configurations performance. The study showcases the potential of these heterostructures in biosensing applications, with distinct advantages in carrier mobility and limit of detection highlighted through comprehensive data analysis. This research offers valuable insights for future endeavors aimed at optimizing the functionality of biosensors based on graphene and MoS_2 heterostructures.

The collective findings from this thesis reveal the potential of biofunctionalized MoS_2-based flexible optoelectronics in revolutionizing biosensing applications. By leveraging the unique properties of 2D materials, such as MoS_2 and graphene, and their heterostructures, this work has laid a solid foundation for the future development of highly sensitive, specific, and flexible biosensors. These sensors not only hold promise for the economical detection of a wide range of biomolecules and biomarkers but also open new avenues for innovations in healthcare, diagnostics, and beyond, with far-reaching implications.

5.2 Future work

Two-dimensional layered van der Waals nanomaterials, particularly semiconducting MoS_2, have garnered attention for chemical and biological sensing due to their unique quantum and surface effects. One future direction is to develop biosensors combining these materials with bioreceptors for sensitive detection of molecules. Moving forward, the development of MoS_2 optoelectronic biosensors will focus on incorporating a broader range of 2D materials and constructing hybrid structures to enhance the devices' sensitivity and selectivity. For integrating additional 2D materials and hybrid structures, including channel materials that enhance carrier mobility and conductivity, along with contact electrodes to decrease contact resistance, and replacing traditional components with high-k materials and 2D layered dielectrics

in microelectronic devices. Also, it is necessary to extend the scope of detectable biomarkers and create innovative wearable technologies for continuous health monitoring. Ultimately, addressing such challenges will bring these advanced biosensing solutions to the market. Further, reproducibility and long-term stability are also significant hurdles, which involves ensuring that these biosensors maintain their sensitivity and selectivity over time, even under varying environmental conditions. Such advancements will set a promising path for enhancing medical diagnostics and broadening the applicability of 2D material-based biosensors.